Experimental Studies of Bimolecular Reaction Dynamics Using Pulsed Tabletop Vacuum Ultraviolet Photoionization Detection

A Dissertation

Presented to the Faculty of the Graduate School

of Cornell University

In Partial Fulfillment of the Requirements for the Degree of

Doctor of Philosophy

by

Daniel Russell Albert

August 2013

Experimental Studies of Bimolecular Reaction Dynamics Using Pulsed Tabletop Vacuum Ultraviolet Photoionization Detection

Daniel Russell Albert, Ph. D.

Cornell University 2013

The development and application of pulsed photoionization detection employing high intensity vacuum-ultraviolet (VUV) radiation produced by tabletop light sources has been utilized to study bimolecular reaction dynamics of phenyl radical reactions. This method employs four-wave mixing of unfocussed commercial nanosecond dye lasers in mercury vapor to generate light at 9.9 eV. Using two or three commercial pulsed nanosecond dye lasers pumped by a single 30 Hz Nd:YAG laser, generation of 0.10 mJ pulses at 125 nm (6×10^{13} photons/pulse) has been demonstrated. The VUV light source has been used as an alternative to the use of synchrotron light sources, for sensitive universal photoionization detection of products from crossed molecular beam reactions employing pulsed beam sources. In the reaction of phenyl radicals with molecular oxygen at collision energies of 64 and 97 kJ/mol, the reaction $C_6H_5 + O_2 \rightarrow C_6H_5O + O$ was found to occur via the formation of long-lived phenylperoxy collision complexes at all collision energies. The reaction of phenyl radicals with propene has also been studied at collision energies of 84 and 108 kJ/mol. The branching ratios between methyl radical elimination, forming C_8H_8, and H-atom elimination, forming C_9H_{10}, were found to be 10:1 at 84 kJ/mol and 3:1 at 108 kJ/mol. By using "soft" vacuum ultraviolet photoionization at 9.9 eV for product detection, we were able to observe both product channels with negligible fragmentation. As a comparison the reaction of phenyl radicals with trans-2-butene has been studied at a collision energy of 97 kJ/mol. We only observe methyl elimination in the reaction with 2-butene and do not observe H-atom elimination.

BIOGRAPHICAL SKETCH

Daniel Albert was born May 29, 1985 to Ron and Carol Albert. He grew up in Sandusky, Ohio with his brother David. Countless hours of his youth were spent enjoying Lake Erie and commiserating as a Cleveland sports fan. He attended Ohio Wesleyan University in Delaware, OH. While at Ohio Wesleyan, Dan enjoyed learning from the Firedogs Ultimate Frisbee team, the wonderful chemistry department and his future wife Rachel. In 2007 he started graduate school at the University of Wisconsin-Madison; joining the laboratory of Gil Nathanson to study gas-liquid interactions using molecular beam scattering. He earned a Master's Degree from Wisconsin and transferred to Cornell University in Ithaca, New York, joining the laboratory of Floyd Davis to study chemical reaction dynamics using crossed molecular beam scattering. Dan and Rachel married on August 1st 2009 in Sandusky, Ohio. They have a son, Noah, born July 16th, 2012.

To Rachel and Noah

ACKNOWLEDGEMENTS

I would like to start by thanking Floyd Davis for being an excellent research mentor through my years here at Cornell. Floyd has provided much advice, guidance and support. I have learned so much in my time here and Floyd has been helpful every step along the way.

I am also greatly indebted to Dave Proctor for my success in the Davis laboratory. When I first arrived at Cornell he gave me an extensive crash course in the experimental techniques being used in the lab. I would also like to thank the other graduate students who have helped me along the way in the Davis group, Martha Beckwidth and Michael Todt.

Nate Ellis has been an excellent mentor and sounding board in the student machine shop. His guidance and willingness to help with machining new parts for the lab has been instrumental to my success.

When I first started my graduate career at Wisconsin, I learned so much from all of the Nathanson Group, Alexis Johnson, Dan Burden, Thomas Krebs and Susan Burden. The Nathanson Group truly fostered my development as a scientist in addition to being a great group of friends. I will forever be indebted to Gil Nathanson for his advice, support and kindness. At a difficult time when I was considering stopping graduate school, Gil encouraged me to continue and went out of his way to help me make a smooth transition out of his lab to be with Rachel at Cornell.

I first learned to love science and research through a series of great teachers and mentors. Dan Brattain at Sandusky High School first got me to love science. Kim Lance at Ohio Wesleyan taught me the joys of scientific research. David Lever at Ohio Wesleyan was a fantastic advisor and kept encouraging me even when I was an immature student during me first years in college.

My parents have nurtured and supported me for my entire life. I strive to live up to the example they have set for me and hope I can be as good of a parent to my children.

This entire journey would not have been fulfilling without Rachel. You have done so much to help me and support me. We started this journey together and

encountered a great many hurdles, but our love has and will continue to carry us through. I cannot imagine someone better to spend a life with. I look forward to all the future has to bring with our family.

TABLE OF CONTENTS

LIST OF FIGURES

LIST OF TABLES

CHAPTER 1: Introduction

Crossed molecular beams experiments can provide extremely detailed insight into the dynamics of bimolecular elementary gas phase chemical reactions.[1,2,3,4,5,6] For three- or four-atom systems forming products that can be detected in a quantum state-resolved manner, experimentally-determined product angular, velocity and quantum state distributions can be compared to predictions derived from "exact" quantum scattering calculations.[7,8,9] For more complex polyatomic systems, the reaction dynamics may involve multiple potential energy surfaces, often leading to more than one reaction product channel. In such cases,[10] the identification of the primary product channels, measuring their branching ratios, and unraveling the microscopic reaction mechanisms, are usually the key goals of both experiment and theory.[11,12]

In studies of bimolecular reaction dynamics, the single-collision conditions offered by the crossed molecular beams method makes it possible to observe nascent products, frequently highly reactive radicals, without interference by secondary collisions. Unfortunately, the low reactant densities required to ensure single collision conditions makes product detection challenging.[2,4] The development of a crossed molecular beams apparatus[13] employing electron impact ionization followed by a quadrupole mass analyzer has facilitated studies of chemical systems ranging from simple 3-atom exchange reactions[14] to complex polyatomic reactions.[15] Electron impact mass spectrometry is a "universal" detection method, applicable to detection of any gaseous atom or molecule. Unfortunately, the sensitivity of electron impact detection is typically much lower than for methods based on electronic spectroscopy, such as laser induced fluorescence (LIF),[16,17] resonance-enhanced multi photon ionization (REMPI),[18,19,20,21] or Rydberg tagging time-of-flight (TOF) spectroscopy[22,23,24,25] However, LIF, REMPI and Rydberg

tagging require detailed knowledge of the spectroscopic fingerprints of the species being detected. While the electronic spectroscopies of atoms and many diatomic molecules are well-characterized, the same can be said for only a relatively small number of triatomic (or larger) molecules. In addition, electronic excitation of polyatomic molecules may lead to photodissociation, thereby rendering LIF, REMPI and Rydberg tagging ineffective for detecting many molecular species.

In the field of bimolecular reaction dynamics involving free radicals, *atomic* free radicals have been studied most extensively, with the greatest focus on H, D, O, F, Cl, Br *etc*. Such species are readily produced in high yield and high purity by photolysis or pyrolysis of a stable precursor. Bimolecular reactions involving atomic free radicals usually proceed with large cross sections, often (but not always) forming a limited number of different products. On the other hand, *molecular* free radicals are more difficult to produce than atomic radicals, and often undergo self-reaction producing impurities. Furthermore, steric factors often play important roles in limiting reaction cross sections[3], particularly for radicals containing 3 or more atoms, and polyatomic free radical reactions often involve more than one channel. From these considerations, studies of polyatomic free radical reactions using crossed molecular beams are extremely challenging.

For several decades, "hard" electron impact ionization (using 60 – 100 eV electrons) was used in an effort to maximize ionization efficiencies (typically 0.01%).[2,4] However, interfering signals at the m/e ratio of interest often arise. Since the residual gases in a UHV chamber are primarily CO and H_2, detection at m/e = 28 and 2 is extremely difficult. To meet this challenge, Yang and coworkers employed extensive cryopumping and took special efforts to reduce pressures in the ionization region to ~10^{-12} Torr, facilitating direct detection of even H_2 from

photodissociation reactions.[26] However, there remains a less predictable source of background due to fragmentation of parent species producing unwanted daughter ions.[2] For example, methyl radicals (CH_3) can be produced by pyrolysis, photolysis, or electric discharge of molecular beams containing azomethane (CH_3NNCH_3). Although a significant fraction may be converted to CH_3, some undissociated azomethane will invariably be present and can undergo nonreactive collisions. Using hard electron impact ionization, fragmentation produces CH_3^+ (m/e = 15), N_2^+ (m/e = 28), N^+ (m/e = 14), $CH_3N_2^+$ (m/e = 43), CH_2^+ (m/e = 14), *etc*. Since background signals at these m/e ratios will be much larger than from bimolecular collisions of CH_3, detection of nonreactive scattering of CH_3 (m/e = 15), or reactions leading to production of C_2H_4 (m/e = 28), CH_2 (m/e = 14), or CH_3CO (m/e = 43) is likely to be impossible.[2]

As a direct consequence of the challenges associated with product detection in crossed beams experiments, the most readily-studied reactions are those producing molecules amenable to resonant detection methods such as REMPI or LIF. For reactions producing molecules not favorable to such detection methods, reactions with large cross sections and/or kinematics favorable for product detection have been studied most frequently. For example, the bimolecular reactions of phenyl radicals (C_6H_5) with propene (C_3H_6), of interest in connection with soot formation, involves addition of the radical to the C=C bond producing C_9H_{11}.[10,27,28,29,30] This reaction intermediate can decompose by loss of an H atom producing C_9H_{10}, or by CH_3 elimination producing C_8H_8.[28,30] The Newton diagrams in velocity space for these competing channels are shown in Figure 1.1, with the circles denoting the maximum CM velocities of the C_9H_{10} and C_8H_8 products. Due to linear momentum conservation, the C_9H_{10} products are constrained to appear at a relatively narrow range of laboratory angles near the center of mass (CM) of the system, resulting in large product densities favorable to successful detection. The

C_8H_8 products, on the other hand, recoil from the heavier CH_3 product and are scattered over a much larger range of angles. Assuming a 1:1 branching ratio and the same CM energy and angular distributions, the product signal intensities scale as the volume of the Newton sphere. In this case, the C_9H_{10} signal intensities at a given laboratory angle would be more than 50 times larger than signal intensities for the C_8H_8 channel, rendering it much easier to detect. The drawback, however, is that it is often difficult to extract much dynamical insight (CM angular and velocity distributions) by measuring the heavy products from H atom elimination, since their laboratory velocity distributions differ very little from that of the CM of the system.[31] More significant from a chemical perspective, many interesting reactions do not proceed exclusively by H atom elimination.

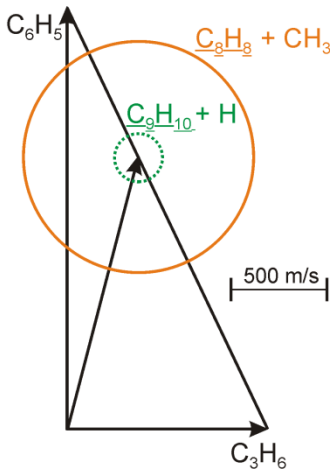

Figure 1.1: Newton diagram for the C_6H_5 + C_3H_6 reaction. The dotted green circle corresponds to the maximum translational energy release of the C_9H_{10} + H product channel. The solid orange circle corresponds to the maximum translational energy release of the C_8H_8 + CH_3 product channel.

To overcome the limitations of dissociative ionization, Casavecchia and coworkers have elegantly demonstrated the use of low energy electrons for "soft" electron impact ionization detection of products from bimolecular reactions in crossed molecular beams.[11,15,32,33] By tuning the electron energies below that for dissociative ionization, interference from fragmentation of parent species may be reduced or eliminated. For example, since the ionization energy for CO (m/e = 28) is 14.0 eV, it is possible to detect species such as C_2H_4 (m/e = 28) with an ionization energy of 10.5 eV by tuning the electron energy around 11-13 eV. Unfortunately, this method comes with a substantial penalty; electron impact ionization cross sections decrease significantly at lower electron energies, leading to very small signal levels. Nevertheless, by decreasing the distances between nozzles and interaction regions, Casavecchia and coworkers were able to compensate for the reduced ionization efficiencies and have mapped out the detailed dynamics for a wide variety of important chemical systems possessing multiple reaction pathways.[11,15,32,33]

Since the ionization energies of most molecules and free radicals exceed 8 eV (Figure 1.2), there has been considerable interest in the use of "soft universal" photoionization detection using vacuum ultraviolet (VUV; $\lambda < 180$ nm) or extreme ultraviolet (XUV; $\lambda < 110$ nm) radiation.[34,35] The quasi-continuous VUV/XUV beam produced at third-generation synchrotrons such as Berkeley's Advanced Light Source[34] or Taiwan's Synchrotron Research Center[35] is broadly tunable in the 9-20 eV range, with ~1% energy bandwidth, providing photon fluxes (~10^{16} photons per second[34,35]) that are sufficient for performing crossed molecular beam scattering experiments.[36,37,38,39,40] The primary limitation of this method is that third-generation synchrotron light sources are available at only a few locations worldwide. Also, due to the size and complexity of crossed molecular beams machines, successful implementation at a synchrotron requires a dedicated beamline for extended periods.

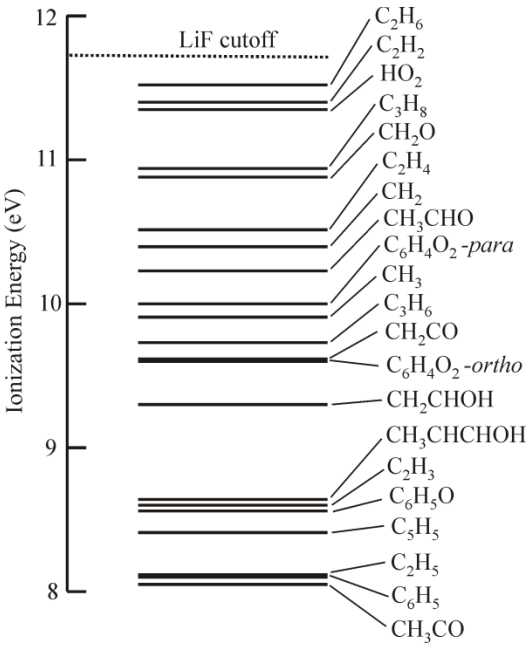

Figure 1.2: Ionization energies of some simple molecules and radicals.

For studies of reactions of transition metal atoms with hydrocarbon molecules, the low ionization energies of metal-containing species has allowed the use of 7.9 eV photons from commercial F_2 excimer lasers (λ = 157 nm) for photoionization detection.[41,42,43,44] The performance of commercial 157 nm excimer lasers has improved greatly over the past couple of decades, and relatively inexpensive lasers producing > 1 mJ/pulse at repetition rates of up to 100 Hz are readily available. The single photon ionization technique for transition metal atoms allowed for an increase of up to 100 in the signal to noise ratio, relative to electron impact ionization.[41] The increase come from both the increased detection efficiency using single photon ionization and also from the near zero background nature of the technique.[41]

Suits and coworkers have carried out ion imaging studies of hydrocarbon reactions leading to hydrocarbon radical products with relatively low ionization energies that can be photoionized at

7.9 eV.[45,46,47,48] However the ionization energies of most nonmetallic free radicals exceeds 7.9 eV, rendering this method ineffective as a universal detection method except for a small number of select systems.

A number of alternatives to synchrotrons exist for production of VUV and XUV radiation. Perhaps the best known approach, still used in photoelectron spectroscopy of stable molecules, employs conventional discharge lamps.[49] However, the intensities of such lamps are typically too low for detection of products from photodissociation or bimolecular reactions. During the past decade, electron beam or RF powered excimer lamps have been employed for soft VUV photoionization in mass spectrometry studies.[50] The 128 nm emission from an Ar_2 lamp is often used, and commercial versions of such lamps, both pulsed and continuous, are now available. However, intensities are still substantially lower than for synchrotron light sources and only a few discrete VUV wavelengths are available.[50] Laser-induced plasma radiation has also been employed as an alternative to synchrotron radiation for studies of the photoionization spectroscopy of small molecules.[51] Focusing a commercial nanosecond excimer laser on a solid target produces a VUV/XUV quasicontinuum which, when dispersed by a grating, provides continuously tunable nanosecond pulsed radiation with ~1% bandwidth in the 10^9 photons per pulse range.[51] Such intensities are sufficient for photoionization spectroscopy but not for detection of products from crossed beam reactive scattering studies.

The generation of pulsed VUV radiation using nonlinear frequency conversion of UV and visible lasers has been exploited quite extensively over the past two decades. Photoionization cross sections for most atoms and molecules increase sharply above threshold. For example, the ionization energy of phenyl radicals (C_6H_5) is 8.6 eV and the photoionization cross section is 1.3 x 10^{-17}cm^2 at 9.9 eV (125 nm).[52] Using a pulsed VUV light source under conditions where the

number of photons greatly exceeds the number of molecules, ionization of 2.5% of the molecules requires a photon flux of ~2 x 10^{15}/cm^2. To achieve 2.5% ionization within a laser diameter of 2 mm, a pulse energy of 0.10 mJ (6 x 10^{13} photons/pulse) is required.

Third harmonic generation ($\omega_{VUV} = 3\omega_1$) or resonance enhanced four wave mixing ($\omega_{VUV} = 2\omega_1 + \omega_2$) using focused nanosecond pulsed lasers in inert gas (e.g. Kr or Xe) cells or pulsed jets is the most well-established method for production of coherent narrow-bandwidth VUV/XUV generation.[53,54,55,56,57] Generation of 10^{10} photons/pulse is readily achievable. Under favorable cases where phasematching is possible using inert gas mixtures, VUV pulses approaching 10^{12} photons per pulse can be generated in certain wavelength ranges including Lyman-α at 121.6 nm.[23,55] While such intensities are suitable for Rydberg tagging TOF spectroscopy [22,23,24,25] or imaging of atomic species[58], these sources are still too weak for universal product detection in crossed beam experiments.

Experimental and theoretical work by several groups has demonstrated that much higher VUV conversion efficiencies may be obtained using metallic gases such as mercury (Hg) as the nonlinear medium.[59,60,61,62] For example, up to 10^{13} photons per pulse near 125 nm (9.9 eV) have been produced by tuning a commercial frequency doubled dye laser to the Hg 6s($^1S_0$) $\rightarrow$7s($^1S_0$) two-photon resonance at 312.85 nm and mixing with the residual 625.70 nm radiation in a focused geometry.[59] By instead mixing the 312.85 nm light with tunable light from a second dye laser, the VUV is broadly tunable with maximum conversion efficiencies in the vicinity of Hg Rydberg resonances.[59] To date, most experimental work using Hg has employed tight-focusing conditions where peak intensities are far above those where simple theory can be used to predict optimum phase matching conditions.[59,60] Under these conditions, saturation and other competing

nonlinear processes often limit the degree to which VUV systems can be scaled to higher energies.

Production of VUV pulses with energies in the millijoule range (> 5 x 10^{14} photons per pulse) at 130 nm was first proposed by Smith and Alford[61] and then demonstrated experimentally by Muller and coworkers[62] using four-wave mixing of transform-limited unfocused nanosecond pulsed lasers in Hg vapor. This method is most general and efficient if three independent input laser beams are each tuned near Hg resonances at the precise wavelengths where index matching may be achieved. Continuous wave (CW) Lyman-α has also been produced using a variant of this approach.[63] As described in the following sections, we have employed commercially-available nanosecond dye lasers to produce high intensity pulsed VUV at 9.9 eV. This allows "soft universal" photoionization detection of a range of interesting free radical species (Figure 1.2). "Universal soft" photoionization detection using VUV generated by resonant-enhanced four wave mixing in mercury vapor has been used to study the reaction dynamics of phenyl radical reactions using crossed molecular beam scattering experiments.

Phenyl radicals (C_6H_5) are an important in combustion because they are reaction intermediates in the oxidation of aromatic species.[10,27] Phenyl radical reactions with unsaturated hydrocarbons lead to production of polycyclic aromatic hydrocarbons (PAH), which in turn lead to soot formation. The primary mechanism for PAH formation is thought to occur via the "hydrogen-abstraction-acetylene-addition" (HACA) mechanism,[10,27,64] in which phenyl radicals are produced and then add to unsaturated hydrocarbons. The reaction products following addition can undergo hydrogen atom abstraction forming a new radical species that can then add to another unsaturated hydrocarbon. By repeating this process, larger PAH can be generated via stepwise addition of smaller hydrocarbons.[64] Understanding branching ratios and reaction

mechanisms of phenyl radical reactions is important in modeling the formation of PAH and soot particles. Branching ratios and reaction dynamics of phenyl radical reactions with molecular oxygen, propene and trans-2-butene will be discussed.

REFERENCES

1. X. Yang, *Annu. Rev. Phys. Chem.*, **58**, 433 (2007).

2. Y.T. Lee in *Atomic and Molecular Beam Methods*, edited by G. Scoles (Oxford University Press, New York, 1988), Vol. 1, pp. 551-568.

3. R.D. Levine, *Molecular Reaction Dynamics*, Cambridge University Press, Cambridge, 2005.

4. Y.T. Lee, *Science*, **236**, 793 (1987).

5. D.R. Herschbach, *Agnew. Chem. Int. Ed. Engl.*, **26**, 1221 (1987).

6. J.C. Poanyi, *Angew. Chem. Int. Ed. Engl.*, **26**, 952 (1987).

7. K. Liu, *J. Chem Phys.*, **125**, 132307 (2006).

8. P. Casavecchia, N. Balucani and G.C. Volpi, *Ann. Rev. Phys. Chem.*, **50**, 347 (1999).

9. S. Liu, C. Xiao, T. Wang, J. Chen, T. Yang, X. Xu, D.H. Zhang and X. Yang, *Faraday Discuss.*, **157**, 101 (2012).

10. J.A. Miller, M.J. Pilling and J. Troe, *Proceeding of the Combustion Institute.*, **30**, 43 (2005).

11. N. Balucani, G. Capozza, F. Leonori, E. Segoloni andP. Casavecchia, *Int. Rev. Phys. Chem.*, **25**, 109 (2006).

12. P. Casavecchia, F. Leonori, N. Balucani, R. Petrucci, G. Capozza and E. Segoloni, *Phys. Chem. Chem. Phys.*, **11**, 46 (2009).

13. Y.T. Lee, J.D. McDonald, P.R. LeBreton and D.R. Herschbach, *Rev. Sci. Instrum.*, **40**, 1402 (1969).

14. D.M. Neumark, A.M. Wodtke, G.N. Robinson, C.C Hayden and Y.T. Lee, *J. Chem. Phys.*, **82**, 3045 (1985).

15. B. Fu, Y-C. Han, J.M. Bowman, F. Leonori, N. Balucani, L. Angelucci, A. Occhiogrosso, R. Petrucci and P. Casavecchia, *J. Chem. Phys.*, **137**, 22A532 (2012).

16. J.L. Kinsey, *Ann. Rev. Phys. Chem.*, **28**, 349 (1977).

17. K-W. Kang, M-J. Park and J-H. Choi, *Phys. Chem. Chem. Phys.*, **13**, 8122 (2011).

18. K. Liu, *Phys. Chem. Chem. Phys.*, **9**, 17 (2007).

19. D. Townsend, W. Li, S.K. Lee, R.L. Gross and A.G. Suits, *J. Phys. Chem. A*, **109**, 8661 (2005).

20. H. Kawamata and K. Liu, *J. Chem. Phys.*, **133**, 124304 (2010).

21. J. Zhang, S.A. Lahankar, D.J. Garton, T.K. Minton, W. Zhang and X. Yang, *J. Phys. Chem. A*, **115**, 10894 (2011).

22. L. Schnieder, K. Seekamp-Rahn, E. Wrede and K.H. Welge, *J. Chem. Phys.*, **107**, 6175 (1997).

23. B.R. Strazisar, C. Lin and H.F. Davis, *Science,* **290**, 958 (2000).

24. C. Lin, M.F. Witinski and H.F. Davis, *J. Chem. Phys.*, **119**, 251 (2003).

25. X. Yang, *Phys. Chem. Chem. Phys.*, **13**, 8112 (2011).

26. J.J. Lin, D.W. Hwang, S. Harich, Y.T. Lee and X. Yang, *Rev. Sci. Instrum.*, **69**, 1642 (1998).

27. H. Richter and J.B. Howard, *Progress in Energy and Combustion Science,* **26**, 565 (2000).

28. J.Park, G.J. Nam, I.V. Tokmakov and M.C. Lin, *J. Phys. Chem. A,* **110**, 8729 (2006).

29. F. Zhang, X. Gu, Y. Guo and R.I. Kaiser, *J. Phys. Chem. A,* **112**, 3284 (2008).

30. R.I. Kaiser, D.S.N. Parker, M. Goswami, F. Zhang, V.V. Kislov, A.M. Mebel, J. Aguilera-Iparraguirre and W.H. Green, *Phys. Chem. Chem. Phys.*, **14**, 720 (2012).

31. S.A. Lahankar, J. Zhang, S. Garashchuk, G.C. Schatz and T.K. Minton, *J. Phys. Chem. Lett.*, **4**, 1315 (2013).

32. G. Capozza, E. Segoloni, F. Leonori, G.G. Volpi and P. Casavecchia, *J. Chem. Phys.*, **120**, 4557 (2004).

33. B. Fu, Y-C Han, J.M. Bowman, L. Angelucci, N. Balucani, F. Leonori and P. Casavecchia, *Proc. Nat. Acad. Sci.*, **109**, 9733 (2012).

34. X. Yang, J. Lin, Y.T. Lee, D.A. Blank, A.G. Suits and A. Wodtke, *Rev. Sci. Instrum.*, **68**, 3317 (1997).

35. C.C. Wang, Y.T. Lee, J.J. Lin, J. Shu, Y-Y. Lee and X. Yang, *J. Chem. Phys.*, **117**, 153 (2002).

36. N. Hemmi and A.G. Suits, *J. Chem. Phys.*, **109**, 5338 (1998).

37. S-H. Lee, C-H. Chin, W-K. Chen, W-J. Huang and C-C. Hsieh, *Phys. Chem. Chem. Phys.*, **13**, 8515 (2011).

38. C-H. Chin, W-K. Chen, W-J. Huang, Y-C. Lin and S-H. Lee, *J. Phys. Chem A*, **116**, 7615 (2012).

39. H.F. Davis, J. Shu, D.S. Peterka and M. Ahmed, *J. Chem. Phys.*, **121**, 6254 (2004).

40. D.A. Blank, N. Hemmi, A.G. Suits and Y.T. Lee, *Chem. Phys.*, **231**, 261 (1998).

41. P.A. Willis, H.U. Stauffer, R.Z. Hinrichs and H.F. Davis, *Rev. Sci. Instrum.*, **70**, 2606 (1999).

42. M. Oana, Y. Nakatsuka, D.R. Albert and H.F. Davis, *J. Phys. Chem. A*, **116**, 5039 (2012).

43. R.Z. Hinrichs, J.J. Schroden and H.F. Davis, *J. Phys. Chem. A*, **112**, 3010 (2008).

44. J.J. Schroden and H.F. Davis, *J. Phys. Chem. A*, **116**, 3508 (2012).

45. C. Huang, W. Li, A.D. Estillore and A.G. Suits, *J. Chem. Phys.*, **129,** 074301 (2008).

46. A.D. Estillore, L.M. Visger-Kiefer, T.A. Ghani and A.G. Suits, *Phys. Chem. Chem. Phys.*,**13**, 8433 (2011).

47. A.D. Estillore, L.M. Visger-Kiefer and A.G. Suits, *Faraday Discuss.*, **157**, 181 (2012).

48. A.D. Estillore, L.M. Visger and A.G. Suits, *J. Chem. Phys.*, **132**, 164313 (2010).

49. S. Souma, T. Sato, T. Takahashi and P. Baltzer, *Rev. Sci. Instrum.*, **78**, 123104 (2007).

50. F. Mühlberger, J. Wieser, A. Morozov, A. Ulrich and R. Zimmermann, *Anal. Chem.*, **77,** 2218 (2005).

51. R. Flesch, M.C. Schürmann, M. Hunnekuhl, H. Meiss, J. Plenge and E. Rühl, *Rev. Sci. Instrum.*, **71,** 1319 (2000).

52. N.E. Sveum, S.J. Goncher and D.M. Neumark, *Phys. Chem. Chem. Phys.*, **8**, 592 (2006).

53. G.C. Bjorklund, *IEEE J. Quantum Electron.*, **QE-11**, 287 (1975).

54. R. Hilbig and R. Wallenstein, *Appl. Opt.*, **21**, 913 (1982).

55. J.P. Marangos, N. Shen, H. Ma, M.H.R. Hutchinson and J.P. Connerade, *J. Opt. Soc. Am. B*, **7**, 1254 (1990).

56. E. Cromwell, T. Trickl, Y.T. Lee and A.H. Kung, *Rev. Sci. Instrum.*, **60,** 2888 (1989).

57. S.J. Hanna, P. Campuzano-Jost, E.A. Simpson, D.B. Robb, I. Burak, M.W. Blades, J.W. Hepburn and A.K. Bertram, *Int. J. Mass. Spec.*, **279**, 134 (2009).

58. M. Ahmed, D.S. Peterka and A.G. Suits, *Chem Phys. Lett.*, **301**, 372 (1999).

59. R. Hilbig and R. Wallenstein, *IEEE J. Quant. Electron.*, **QE-19**, 1759 (1983).

60. R. Mahon and F.S. Tomkins, *IEEE J. Quant. Electron.*, **QE-18**, 913 (1982).

61. A.V. Smith and W.J. Alford, *J. Opt. Soc. Am. B*, **4**, 1765 (1987).

62. C.H. Muller, D.D. Lowenthal, M.A. DeFaccio and A.V. Smith, *Opt. Lett.*, **13**, 651 (1988).

63. M. Scheid, D. Kolbe, F. Markert, T.W. Hänsch and J. Walz, *Opt. Express*, **17**, 11274 (2009).

64. J. Appel, H. Bockhorn and M. Frenklach, *Combustion and Flame*, **121**, 122 (2000).

CHAPTER 2: High-Intensity Coherent Vacuum Ultraviolet Source Using Unfocussed Commercial Dye Lasers

Introduction

Coherent radiation in the visible, infrared, and near ultraviolet can be readily produced using commercial lasers employing nonlinear frequency conversion in solid crystals.[1] However, since birefringent crystals are not capable of transmitting wavelengths shorter than ~ 190 nm, coherent light sources in the vacuum ultraviolet (VUV) and extreme ultraviolet (XUV) employ gases rather than solids for nonlinear frequency conversion. Unfortunately, due to the low densities and small nonlinear susceptibilities of gases, conversion efficiencies producing $\lambda < 190$ nm are typically much less than 1%.[2,3,4,5]

In recent years, a number of alternative VUV and XUV light sources have been developed, including discharge lamps[6,7] and laser induced plasma sources.[8] However, these approaches are not generally applicable if high peak powers, high spectral purity, and high spatial coherence is required. The undulator beamline at Berkeley's Advanced Light Source, a third generation synchrotron,[9] provides ~10^{16} photons per second with an energy resolution, $\Delta E/E$, of ~ 1%.[9] However, the need for a dedicated facility limits applicability of this method to only a few sites worldwide.[9,10] Furthermore, the quasi-continuous nature of synchrotron radiation generally prohibits applications requiring high peak VUV or XUV powers such as materials processing or multiphoton spectroscopy. Also, many experiments can benefit greatly from the use of pulsed rather than continuous VUV light sources. Therefore, considerable effort has been devoted to increasing the efficiencies for nonlinear frequency conversion of tabletop pulsed lasers into the VUV and XUV region.

The earliest reports of nonlinear frequency conversion in gases involved third harmonic generation.[11,12] For example, the spectroscopically important Lyman-α at λ = 121.6 nm is readily produced by focusing the 364.8 nm output from a single commercial dye laser (typically operating at 10-30 Hz) into a gas cell containing Kr.[13] For input pulse energies of ~ 10 mJ (τ ~ 6-20 ns), ~10^{10} photons/pulse can be obtained in the VUV, ($\nu_{VUV} = 3\nu_{1)}$ corresponding to a conversion efficiency of ~10^{-6}. Other mixing schemes employing Kr or Xe using a single dye laser have been described, providing continuously tunable radiation between 110 and 210 nm.[2,14]

By using two input laser beams, one tuned to a two-photon atomic resonance, the resonance enhancement of χ^3 leads to substantially improved conversion efficiencies. For example, broadly tunable radiation near 10 eV can be generated by four-wave difference frequency mixing mixing ($\nu_{VUV} = 2\nu_1 - \nu_2$) of focused lasers in Kr, producing ~10^{11} photons/pulse.[15] For specific VUV wavelengths, phase matching (*e.g.,* by addition of Ar) makes it possible to employ higher gas pressures, facilitating production of ~10^{12} photons/pulse reported at Lyman-α using λ_1 = 212.55 nm and λ_2 = 850 nm.[3,16] However, for generation of high VUV intensities using difference frequency mixing using focused lasers, two major practical limitations are difficult to overcome: 1) it is difficult to generate input pulse energies at λ_1 (typically < 220 nm) exceeding 1-2 mJ, and 2) the onset of dielectric breakdown using focused lasers generally limits maximum input pulse energies.

In general, for generation of high VUV pulse energies above 9.5 eV, a significant advantage to resonance enhanced sum frequency ($\nu_{VUV} = 2\nu_1 + \nu_2$) mixing over difference frequency ($\nu_{VUV} = 2\nu_1 - \nu_2$) mixing is that longer input wavelengths can be employed, allowing substantially higher input pulse energies. Unfortunately, sum frequency mixing schemes usually exhibit considerable variation in VUV conversion efficiencies with ν_2.[15] However, for many VUV

applications, broad tunability is not necessary, and the primary goal is instead to achieve the highest possible VUV pulse energies at specific wavelengths, e.g., 130.2 nm for O atom detection, or ~ 125 nm for single photon ionization of organic radicals from bimolecular reactions. The application of VUV for ultrasensitive photoionization detection in analytical mass spectrometry has been discussed in some detail.[17]

While phase matching by the addition of gases such as Kr or Xe may be employed to enhance conversion efficiencies at certain wavelengths,[3,13,14] this is not always possible. For example, the efficiency for difference frequency mixing in Kr to generate 130.2 nm light needed for excitation of the $^3P_J \rightarrow {}^3S_1$ transition in oxygen atoms cannot be enhanced by adding Ar or Xe.[3] However, as discussed in detail below, by tuning *three* input laser beams in the vicinity of atomic resonances, phase matching can be achieved in the absence of additional gases, leading to great enhancement of VUV intensities.

Because of their very large χ^3, metallic vapors such as magnesium (Mg) and mercury (Hg) are frequently used to obtain substantially higher conversion efficiencies into the VUV and XUV.[18,19,20,21,22] For example, by focusing two lasers into Hg vapor, Hilbig and Wallenstein demonstrated that by tuning one laser to the $6\ {}^1S_0 \rightarrow 7\ {}^1S_0$ two-photon resonance at $\lambda_1 = 312.85$ nm,[19] up to ~0.5% conversion efficiency employing a second laser tunable in the visible region can be achieved, with the greatest efficiencies reported in the 125 nm (9.9 eV) range. In this way up to 10^{13} photons/pulse at a specific wavelength near 125 nm was reported.[19] Although theory predicts that for focused geometries in Hg using the $7\ {}^1S_0$ two-photon resonance, VUV generation should be limited to the high energy side of $^1P_1$ resonances below the Hg^+ limit (10.4 eV), in practice tunable light is also observed on the low energy side.[19] Thus the VUV conversion efficiency exhibits pronounced maxima near $^1P_1$ resonances. Although slightly less

efficient, the 625.70 nm and 312.85 nm outputs from a *single* frequency-doubled dye laser can be used to produce very high VUV intensities at a single wavelength near 125 nm.[19]

All of the methods described above employ *focused* configurations for VUV generation. Usually, saturation and dielectric breakdown effects become significant as laser powers are increased, making it impossible to scale systems to higher pulse energies.[20] To avoid this limitation, Smith and Alford proposed a four-wave mixing scheme employing three unfocused tunable lasers for VUV generation in Hg vapor, as shown in Figure 2.1.[20] By tuning λ_1 near the 253 nm $6\ ^1S_0 \rightarrow 3\ ^3P_1$ resonance, λ_2 near 404 nm (corresponding to the $6\ ^1S_0 \rightarrow 7\ ^1S_0$ two-photon resonance), and λ_3 near 777 nm (near a $9\ ^1P_1$ resonance), phase matching can be achieved while at the same time χ^3 is maximized due to the triply-resonant nature of the four-wave mixing process.[20] An attractive feature of this approach is that the system should be scalable to higher VUV pulse energies by using higher input pulse energies, because of the use of collimated (unfocussed) lasers. Using this method, Muller et al. produced ~1.2 mJ per pulse (8×10^{14} photons/pulse) at 130.2 nm, corresponding to the $^3P_2 \rightarrow\ ^3S_1$ transition in oxygen atoms.[21] In their work, the 8 mm diameter input beams, each around 10 mJ/pulse, (τ = 2.2 ns) were of single longitudinal mode (SLM) with near- transform-limited bandwidths. Their system was extremely complex, employing three separate ring dye laser oscillators followed by dye and titanium sapphire amplifiers pumped by Nd:YAG lasers.[21] Since that time, no further work has been reported for pulsed VUV using this method. However, several groups have employed this triply-resonant scheme using three tunable continuous-wave lasers in focused configurations in Hg for producing continuous-wave VUV radiation at unprecedented intensities.[23,24]

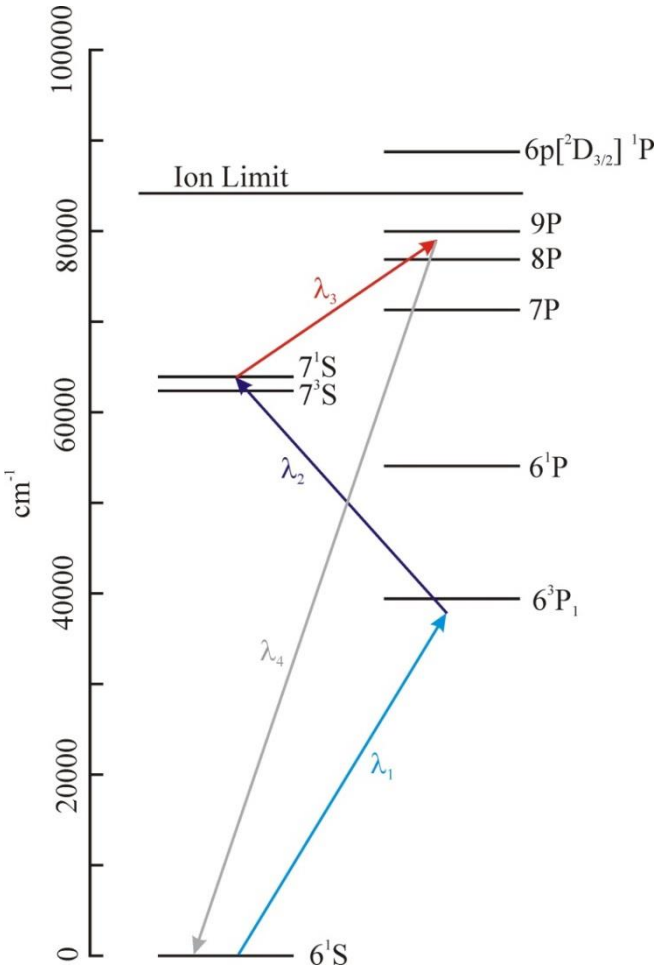

Figure 2.1: Energy level diagram of selected states of mercury. λ_1 is tuned near a single photon resonance ($6\ ^1S_0 \rightarrow 6\ ^3P_1$), λ_2 is tuned so that $\lambda_1 + \lambda_2$ is two-photon resonant ($6\ ^1S_0 \rightarrow 7\ ^1S_0$) and λ_3 is tuned near a Rydberg resonance ($9\ ^1P_1$). The resulting sum frequency is generated at $\lambda_4 \approx$ 125 nm.

On the basis of the previous theoretical and experimental work, it was not at all obvious that the remarkably high VUV intensities reported by Muller et al.[21] might be achieved by four wave mixing of *unfocussed* commercial multimode dye lasers. However, using output beams from commercial lasers with a Hg oven in an arrangement similar to that of Hilbig and Wallenstein[19] in our laboratory, we found that substantial VUV intensities near 9.9 eV could be produced in a 2 cm long Hg cell *with the focusing lens removed*. Subsequently, by employing substantially longer Hg heat pipes, we have optimized conditions for producing very high VUV intensities by

mixing through the 7 $^1S_0$ state in mercury using unfocussed configurations. We have used these VUV beams for "soft" single photon VUV ionization in crossed molecular beam scattering experiments[25] as well as at 130.2 nm for oxygen atom Rydberg time-of-flight (ORTOF) spectroscopy studies.[26]

In our laboratory over the past few years, a number of different schemes have been employed for VUV generation using two or three commercial dye lasers and, in some cases, the 266.1 nm radiation (fourth harmonic) of the injection-seeded Nd:YAG laser. Here we present intensity measurements and tuning curves for generating radiation near 125 nm, and demonstrate the light source for 130.2 nm radiation in ORTOF studies. We provide a detailed description of a design that easily eliminates laser damage of windows due to contamination issues, a common problem using mercury as the nonlinear material. An off-axis MgF_2 lens is used to separate the VUV from the residual visible and UV beams. Comparisons are made to the detailed calculations by Smith and Alford.[20]

Experimental

The VUV radiation was generated by resonance-enhanced four-wave mixing in mercury vapor.[20] The tunable input beams were generated using two or three commercial pulsed dye lasers (Scanmate 2) pumped by a single injection-seeded Nd:YAG laser (Continuum Powerlite 9030 or Precision 9030). The dye lasers were pumped at either 532 nm or 355 nm, corresponding to the second and third harmonics of the Nd:YAG laser, respectively. The dye laser beams were typically ~2 mm diameter. In some cases the fourth harmonic (266.1 nm) of the Nd:YAG pump laser was telescoped to ~2 mm diameter and used as λ_1 in the four wave mixing scheme. In all cases, the optical pathlengths for λ_1, λ_2 and λ_3 were matched (to within about 1″) to ensure that

all three pulses were temporally overlapped in the heat pipe. The polarizations of all three lasers were linear, with λ_1 and λ_2 parallel. The output VUV polarization is parallel to λ_3.

The three laser beams were propagated separately via dielectric mirrors and then combined on a fused silica Pellin-Broka prism located near the entrance to the heatpipe. The use of a Pellin-Broka prism in a "reverse geometry" (i.e., to combine beams of different wavelengths) provides two significant advantages: 1) three separate wavelengths can be easily combined without the need for expensive dichroic mirrors, and 2) by using the prism with P-polarization for all three laser beams, reflective losses are negligible. The input window to the heatpipe was mounted at Brewster's angle to further minimize reflective losses.

The heat pipe consisted of 2.5 cm outer diameter stainless steel tubing with 20 cm of water cooling (~ 293 K) on each end of the tube (Figure 2.2). To assemble the heat pipe, thermocouples were first attached to the stainless steel tube in five locations in order to monitor the temperature. The center 60 cm of the tube was then wrapped with several layers of 0.050″ thick copper sheet followed by three heating tapes surrounded by several layers of aluminum foil. The central portion of the tube (60 cm) was heated to ~410 K generating ~1 Torr of Hg vapor. A pool of mercury was held in the center of the tube by a slight bend on both sides of the tube so that the mercury pool was held in the center 60 cm of the tube. Liquid mercury condensed in the water-cooled region of the tube returns to the lowest central region due to gravity. The tube was evacuated using a dual stage rotary pump and a slow flow of helium (~10 Torr) was directed away from each end of the tube to keep the optics clean. The helium entered at each end of the cell, approximately 3 cm from the window surface, and exited at each end of the cell ~10 cm from the windows. The helium flow rate was controlled by needle valves on

both the inlet and outlet. The flow is sufficiently slow that a cylinder of helium lasts for several months of continuous flow.

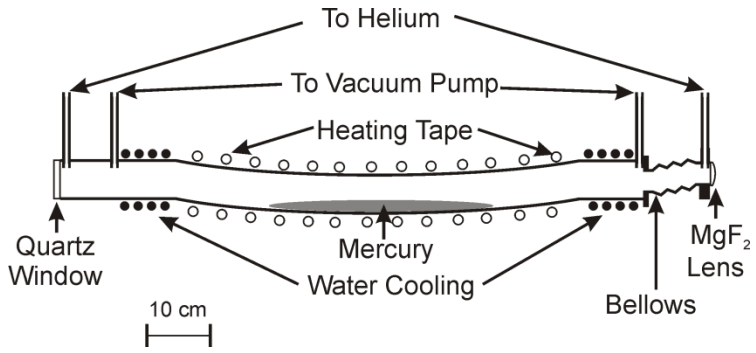

Figure 2.2: Schematic of the mercury heat pipe.

The energy level diagram for atomic mercury is shown in Fig. 2.1. The first photon (λ_1) near 255 nm was typically generated by frequency doubling the 765 nm light from the output of a 532 nm pumped dye laser (LDS 765 laser dye) and then mixing the doubled light with the residual 765 nm radiation. Since a 382.5 nm waveplate was not available, a 266 nm waveplate was used between the doubling crystal and the mixing crystal in order to rotate the polarization of the 382.5 nm light to achieve optimal mixing. The waveplate was angle tuned to maximize the 255 nm light intensity. In some experiments, the 255 nm light was produced by frequency doubling the 510 nm output from a 355 nm pumped dye laser. Typical pulse energies used in these experiments were 2 - 3 mJ per pulse at 255 nm. The second photon (λ_2) near 404 nm was generated either by pumping a mixture of Exalite 404 (Exciton) in dioxane at 355 nm or by mixing the ~651 nm light from a 532 nm pumped dye laser (DCM or Pyridine 1 laser dye) with the 1064 nm light from the injection seeded Nd:YAG laser. Typical pulse energies at 404 nm were 6 - 10 mJ per pulse. The third photon (λ_3) near 630 nm or 777 nm was generated directly

from a 532 nm pumped dye laser (DCM or LDS 765 laser dye, respectively). Typical pulse energies at 630 nm or 777 nm were 7 - 8 mJ per pulse.

We have also generated VUV pulses using only two dye lasers. For example, using $\lambda_1 = \lambda_2 =$ 312.76 nm (10 mJ/pulse) and $\lambda_3 = 630$ nm, light near 9.9 eV is generated. Alternatively, $\lambda_1 =$ 266.1 nm, obtained as the fourth harmonic of an injection seeded Nd:YAG laser with the two-photon resonance achieved using $\lambda_2 = 379.5$ nm, generated by mixing 589 nm light (Kiton Red laser dye) with 1064 nm fundamental from the Nd:YAG laser. Typical pulse energies were 10 mJ at both 266.1 nm and 379.5 nm. While much higher 266.1 nm pulse energies were achievable, after telescoping to ~2 mm diameter, mirror damage occurred at pulse energies above 10 mJ.

In order to isolate the VUV beam from the three strong residual UV and visible beams, they are dispersed by a 50 cm focal length MgF_2 lens (2.54 cm diameter) by propagating the beams off of the optic axis of the lens. The MgF_2 lens also served as the output window of the mercury cell. The lens was mounted in an o-ring sealed home-made lens mount machined from a 2.75″ OD double-sided conflat flange. The lens mount was connected to the mercury cell using a commercial 4″ long bellows with 2.75″ conflat flanges at both ends, as illustrated in Figure 2.2. The lens mount was rigidly supported on a one dimensional translation stage and a second 4″ long bellows assembly connected the lens to the apparatus. This arrangement made it possible to translate the lens horizontally while the mercury cell and vacuum system remained stationary.

For initial alignment of the lasers and MgF_2 lens, a red helium neon laser was counter propagated through the photoionization region, edge of the MgF_2 lens, VUV cell and Pellin-Broka prism towards the three dye lasers. The λ_3 laser was then overlapped with the red helium

neon laser and then the alignment of lasers at λ_1 and λ_2 adjusted to achieve good spatial overlap. Due to the much larger index of refraction for VUV beam, the final position of the MgF_2 lens must be adjusted using the translation stage to precisely locate the VUV beam at the ionization region of the detector. After all beams are aligned and the VUV intensity optimized and spatially aligned, the macor beam dump, held on a vacuum compatible linear manipulator was then translated horizontally to block the 255, 404 and 630 nm beams while allowing the 125 nm light to pass.

The high intensity VUV light source at 125 nm was coupled to the Cornell rotatable source, fixed-detector crossed molecular beams apparatus for "soft" single photon ionization.[25,27] The high intensity light source at 130.2 nm was used on a different apparatus, employing a fixed source and rotatable detector, for studies involving ORTOF.[26] In ORTOF, another tunable laser near 305 nm is used to excite oxygen atoms from the 3 $^3S_1$ state to a high lying long-lived Rydberg state.[26] The Rydberg atoms drifted ~33.3 cm before being passing through a grounded mesh and being field ionized and detected using a microchannel plate detector.

In the rotatable source machine, no additional optical elements were present between the MgF_2 dispersing lens and the ionization region of a quadrupole mass spectrometer where the base pressure was $< 1 \times 10^{-10}$ Torr. An isolation valve and two stages of differential pumping (employing two turbomolecular pumps) were used. In the Rydberg machine, after the residual beams were dumped, the VUV was reflected into the apparatus using a protected aluminum mirror (E-source optics) mounted in a 5-way 8" conflat cross pumped by a turbomolecular pump.

All of the intensity measurements were recorded using the rotatable source, fixed detector apparatus by monitoring the wide angle inelastic scattering of chlorobenzene (C_6H_5Cl) off of

molecular oxygen (O_2). The C_6H_5Cl beam was produced by bubbling H_2 carrier gas (20 PSIG) through a room-temperature liquid C_6H_5Cl sample and expanding the mixture through the 1 mm orifice of a piezoelectrically actuated pulsed valve.[28,29] The molecular beam was skimmed by a 2 mm diameter skimmer before entering the main chamber and crossing the O_2 beam. The O_2 beam was produced by expanding a 40% O_2 in He mixture (40 PSIG) through the 1 mm orifice of a second piezoelectrically actuated pulsed valve. The beam was skimmed by 1.5 mm diameter skimmer before entering the main chamber and crossing the C_6H_5Cl beam. After the beams cross, the non-reactively scattered components are monitored at various lab angles (15 to 30 degrees). The scattered components travel ~25 cm before they are ionized by the 125 nm VUV beam. The ions are then mass filtered using a quadrupole mass analyzer (Extrel) and counted using an electron multiplier/conversion dynode set-up. For comparison measurements between a 7.9 eV excimer laser (GAM EX100HF) and our 125 nm light source the non-reactive scattering of n-methylaniline was monitored since it can be ionized at both 7.9 and 9.9 eV.

Review of Theoretical Calculations

The calculations based on the measured refractive indices and nonlinear susceptibilities of Hg vapor, published by Smith and Alford in 1987,[20] are of great value for predicting tuning curves and nonlinear conversion efficiencies employing collimated (unfocussed) pulsed laser beams. Before discussing our experimental results, we briefly review some of their results.

Figure 2.3 shows the partial Δk, calculated by Smith and Alford, for mixing of collimated low-intensity lasers as a function of frequency near the $^3P_1$ Hg resonance at ν = 39412 cm^{-1} (λ = 253.7 nm), and the 9p $^3P_1$ and $^1P_1$ resonances near 80,000 cm^{-1}.[20] For a given choice of ν_1, the value of Δk_1 in the vicinity of the $^3P_1$ resonance is first read directly from Fig. 2.3. For

collimated laser beams, the VUV frequency where phase matching occurs, corresponding to the same partial Δk, is then read from figure 2.3. For example, for $\lambda_1 = \lambda_2 = 312.85$ nm, corresponding to the two-photon resonance in Hg at 31,964 cm^{-1}, $\Delta k_1 = 0.18$ is indicated by the dotted horizontal line. As indicated in Fig. 2.3, the optimum VUV frequency (ν_{vuv}) corresponding to the same value of Δk lies approximately halfway between the $^3P_1$ and $^1P_1$ resonances, *i.e.*, near $\nu_{vuv} = 79688$ cm^{-1}. Using the two-photon resonance frequency of 63,928 cm^{-1}, the optimum phase matching input wavelength, λ_3 is calculated to be 634.5 nm.

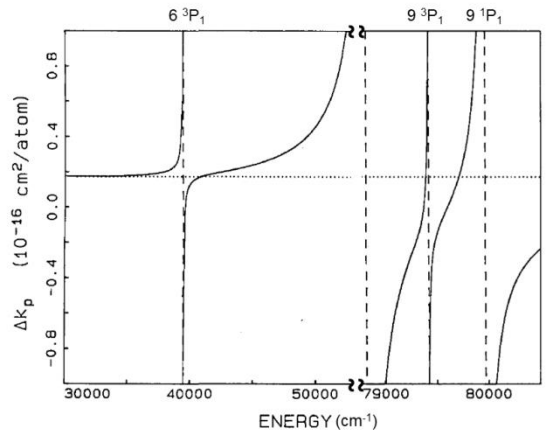

Figure 2.3: Partial Δk as a function of frequency near the 6^3P_1 and $9\ ^3P_1$ and 9^1P_1 resonances, from Smith and Alford, ref. 20. Note change in horizontal axis and scale.

The partial susceptibilities χ_p, plotted in Fig. 2.4, can be used to estimate relative VUV intensities for various specific combinations of ν_1 and ν_{VUV}. As described by Smith and Alford, the third order nonlinear susceptibility $\chi 3$ is proportional to the magnitude of the product $\chi_1 \times \chi_{VUV}$.[20] With ν_1 detuned to frequencies significantly lower than the $^3P_1$ resonance at 39412 cm^{-1}, χ_1 is approximately constant at -2.5 and, under phase matching conditions with $\nu_{vuv} = 79688$ cm^{-1},

the corresponding $\chi_{VUV} \approx 2.5$. As described below, this scheme is attractive in terms of experimental simplicity because only two relatively efficient DCM dye lasers are required, operating at 312.85 nm and ~ 634.5 nm.

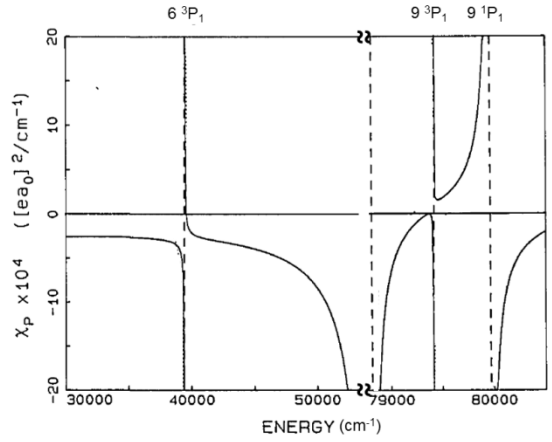

Figure 2.4: Partial susceptibilities χ_P as a function of frequency near the 6^3P_1 and $9\ ^3P_1$ and 9^1P_1 resonances, from Smith and Alford, ref. 20. Solid lines are for the $7\ ^1S_0$ resonance studied in this work. Note change in horizontal axis and scale.

Using three independently tunable lasers, one can tune ν_1 to higher frequencies on the low energy side of the $^3P_1$ resonance while simultaneously tuning ν_2 to remain on the 7^1S_0 two-photon resonance (Fig. 2.1). Under these conditions, Fig. 2.3 indicates that ν_{VUV} shifts slightly to the blue and, according to Fig. 2.4, VUV intensities will increase slightly. However, as ν_1 is tuned very close to the $^3P_1$ resonance from the low energy side, Δk_1 increases sharply. To maintain phase matching conditions, ν_{vuv} shifts to higher frequency, requiring progressively greater ν_3 as the $9\ ^1P_1$ resonance at $\nu = 79964\ cm^{-1}$ is approached. As indicated in Fig. 2.4, χ_1 and χ_{VUV} both increase sharply in the vicinity of atomic resonances, so the largest VUV

conversion efficiencies are predicted for $\lambda_1 \approx 255$ nm, $\lambda_2 \approx 404$ nm, and $\lambda_3 \approx 628$ nm, producing VUV light at wavelengths near 125 nm ($\nu_{VUV} \approx 79850$ cm^{-1}).

With ν_1 tuned to frequencies greater than 39412 cm^{-1}, *i.e.,* on the high energy side of the $^3P_1$ resonance, qualitatively similar behavior is predicted. However, since Δk_1 is negative close to the 6^3P_1 resonance, phase matching requires tuning of ν_3 so ν_{VUV} is on the blue side of the $^3P_1$ or $^1P_1$ resonances. It should be noted, however, that because χ_1 changes sign (goes through zero) at frequencies ν_1 just above 39412 cm^{-1}, the VUV conversion efficiencies will exhibit a considerably more complex frequency dependence.

VUV Generation Near 125 nm

Relative intensity measurements for a number of resonant two-photon mixing schemes, all employing the 7^1S_0 state at 63,928 cm^{-1}, are shown in Figure 2.5. Table 2.1 lists the wavelengths employed for the different VUV generation schemes studied in our laboratory. Each tuning curve shown in Figure 2.5 represents a different two-photon combination (λ_1 and λ_2) and shows the resulting λ_3 tuning curve. Tuning curve a) was obtained with $\lambda_1 = 266.1$ nm (fourth harmonic of the Nd:YAG laser) and $\lambda_2 = 379.5$ nm. The tuning curve of λ_3 was recorded by scanning λ_3 while monitoring the non-reactive scattering of C_6H_5Cl from O_2. For this scheme, only two tunable lasers are required. As shown in Figs. 3 and 4, for significant detuning of ν_1 below the 6^3P_1 resonance, Δk_1, χ_1, and χ_{VUV} are all approximately constant so conversion efficiencies do not vary significantly with ν_1 and ν_2. Because relatively high UV pulse energies (10 mJ for each laser) can be generated as the Nd:YAG fourth harmonic and at 379.5 nm (the latter by mixing the Nd:YAG fundamental with 590 nm light), and because only two dye lasers are required, this scheme has been used quite extensively in our laboratory.

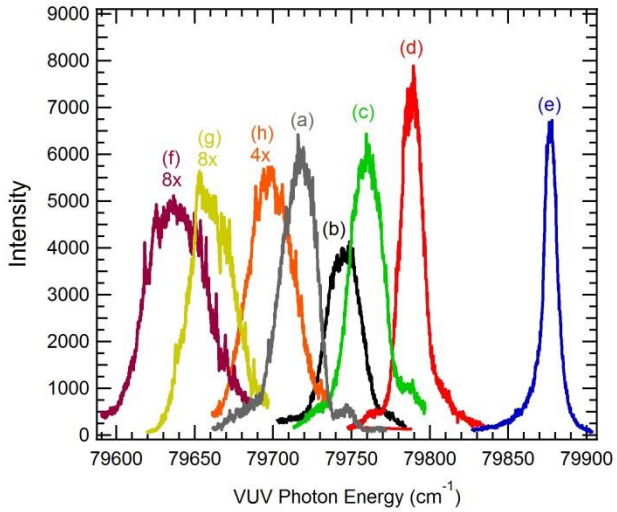

Figure 2.5: Tuning curves for VUV generation (tuning λ_3) when $\lambda_1 + \lambda_2 = 63928$ cm^{-1} for the following λ_1 values with mJ per pulse of λ_1 in parenthesis. See Table 2.1 for corresponding values for λ_2. The $6\ ^1S_0 \rightarrow 6\ ^3P_1$ resonance in mercury is at 253.7 nm (39412 cm^{-1}). All curves are not scaled except for those marked in the figure (a) 266.1 nm (10 mJ) (b) 256.6 nm (1.3 mJ) (c) 255.7 nm (2.5 mJ) (d) 254.8 nm (2.7 mJ) (e) 254.0 nm (2.7 mJ) (f) 252.1nm (1.5 mJ) (g) 251.6 nm (1.3 mJ) (h) 247.9 nm (1.5 mJ).

Table 2.1: Wavelengths (nm) used for resonance enhanced four-wave mixing in Hg vapor.

λ_1	λ_2	λ_3	λ_4
266.1	379.5	633.6	125.45
256.6	400.7	632.0	125.39
255.7	402.9	631.4	125.37
254.8	405.2	630.2	125.32
254.0	407.2	627.0	125.20
252.1	412.2	636.5	125.57
251.6	413.5	635.9	125.54
247.9	423.9	634.0	125.47

Because the Nd:YAG laser is injection seeded by a narrowband CW diode laser, the bandwidth of the 266.1 nm laser is nearly Fourier transform limited with bandwidth of < $0.005 cm^{-1}$. Somewhat surprisingly, we found that the VUV intensity did not decrease significantly when the injection seeder was turned off with the Nd:YAG fundamental bandwidth increasing to ~1 cm^{-1}. Consequently, the bandwidths of ν_1 and ν_2 increase from <0.010 cm^{-1} and $0.15 cm^{-1}$ to 2 cm^{-1} and 1 cm^{-1}, respectively. While we have not studied this behavior extensively, this observation suggests that VUV conversion efficiencies under our specific experimental conditions are not strongly dependent on input laser bandwidths.

On the basis of Fig. 2.3, it is not surprising that the VUV tuning curve employing the 2-photon 7 $^1S_0$ resonance at $\lambda_1 = \lambda_2 = 312.85$ nm (not shown) was found to be very similar to that shown in Fig. 2.5a. However, the absolute VUV intensities using the 312.85 nm two-photon resonance were about a factor of two smaller under our experimental conditions. Because of its relative simplicity, employing the two-photon resonance is the most convenient possible approach for generation of high-intensity VUV using collimated lasers. In our laboratory, typically 10 mJ pulses at 312.85nm (30 Hz) could be produced routinely. At the expense of somewhat greater complexity (using two dye lasers + fourth harmonic of Nd:YAG), the scheme with λ_1 =266.1 nm (10 mJ) and λ_2 = 379.1 nm (10 mJ), we typically obtained a factor of 2 higher VUV intensities. The higher intensity using 266.1 nm scheme is entirely attributable to the factor of 2 greater total laser pulse energies at λ_1 and λ_2. As shown in curves b, c, d, upon tuning λ_1 closer to the 6 $^3P_1$ resonance, a gradual increase in VUV intensity is observed. Note that curve d was obtained with 254.8 nm pulse energies around 2.7 mJ, whereas curve a employed 266.1 nm pulse energies around 10 mJ. Clearly, conversion efficiencies increase significantly (by a factor of 4) as the ν_1 approaches the 6^3P_1 resonance. It is interesting to note, however, that

according to curve e, obtained with λ_1 = 254.0 nm (only 38 cm^{-1} below the 6^3P_1 resonance), maximum VUV intensities do not further increase as the 6^3P_1 resonance is approached. Clearly, factors other than those indicated in Fig. 2.4, (e.g., absorption in the VUV by Hg_2) are operative, effectively limiting conversion efficiencies close to the 6^3P_1 resonance. Our limited studies of the effect of Hg vapor pressure (by changing the temperature) suggest that peak VUV conversion efficiencies remain approximately constant when ν_1 is tuned over a range of about 200 cm^{-1} on the low energy (red) side of the $6\ ^3P_1$ resonance.

Curves f, g, and h in Figure 2.5 were recorded with λ_1 tuned to the high energy (blue) side of the 6^3P_1 resonance. Note that these curves have been multiplied by factors of 8, 8 and 4, respectively, indicating significantly lower conversion efficiencies in this region. The relatively low intensities for curves f and g are attributable to the fact that χ_1 approaches zero just to the blue of the resonance, as shown in Fig. 2.4. The increased conversion efficiency observed for curve h, with λ_1 tuned further from the atomic resonance, is due to the larger χ_1 and χ_{VUV} in this region.

As illustrated in figure 2.5 (curves a-e), the VUV tuning curves become narrower as the VUV energy approaches the 9P resonance from the low-energy side. This behavior can be understood from the calculations of Smith and Alford.[20] As illustrated in figure 2.3, the slope of the plot of the index mismatch Δk vs. photon energy increases as atomic resonances are approached. The choice of input wavelength λ_1 in the vicinity of the $^3P_1$ resonance at 253 nm dictates VUV wavelength where maximum conversion efficiency can be achieved. The VUV tunability (i.e., tunablity of λ_3) is limited by the requirement that the partial index mismatch Δk falls within a range specified by λ_1. At VUV wavelengths far away from the 9P resonance where

Δk varies weakly with λ, a relatively wide range of VUV wavelengths fall within the specified Δk. However, near resonances, the much stronger dependence of Δk on λ_3 (steeper slope in Fig. 2.3), leads to a narrower range of VUV tunability.

Absolute VUV Pulse Energy Measurements

In order to determine the absolute VUV pulse energies, we have compared signals from the non-reactive scattering of n-methylaniline from O_2 using the 7.9 eV output of an F_2 excimer laser and our 9.9 eV light source. We found that the total signal level using the 9.9 eV light source using the 266.1 nm + 379.5 nm mixing scheme (curve 5a) is 6 times smaller than that of the 7.9 eV light source. We have measured the 7.9 eV pulse energy using a pyroelectric energy meter to be 1.0 mJ per pulse (~8 x 10^{14} photons per pulse). Using the 8 x 10^{14} photons per pulse value at 7.9 eV and correcting for the factor of 3 difference in photoionization cross section of n-methylaniline between 7.9 eV and 9.9 eV[30]; we conclude that 0.07 mJ per pulse at 125 nm is delivered to the ionization region of the detector at the peak of curve 5a. Assuming 70% transmission through the MgF_2 lens, this corresponds to 0.10 mJ/pulse at 125 nm, i.e., 6 x 10^{13} photons/pulse. At 30 Hz, this corresponds to 1.8 x 10^{15} photons/s.

Our measured VUV pulse energy at 125 nm is a factor of ~10 smaller than that reported previously near 130 nm using three transform-limited pulsed lasers, each providing ~10 mJ/pulse.[21] The principal differences between our conditions and those reported earlier are that our lasers are multimode with bandwidths of ~0.15 cm^{-1} each (~0.21 cm^{-1} after frequency doubling) rather than Fourier transform limited. Also, the spatial quality of the beams produced by commercial dye lasers deviate significantly from the Gaussian distributions employed in the previous work. In our experiment, the 255 nm pulse energy was limited to 2.7 mJ because only a

single Nd:YAG laser was available for pumping all three dye lasers. Also, our pulse duration was substantially longer $\tau \sim 7.0$ ns than that in the previous experiments (~2.2 ns). Using these parameters, the calculated peak 255 nm laser power in our work (0.43 MW) is about an order of magnitude smaller than in the work of Muller (4.5 MW).[21]

VUV Generation near the 130.2nm $^3P_J \rightarrow {}^3S_1$ Transition in Atomic Oxygen

We have demonstrated the tunability of the high-intensity light source by tuning to the atomic oxygen $^3P_2 \rightarrow {}^3S_1$ transition at 130.2 nm.[26] In these studies, a photon at 130.2 nm photodissociates O_2 molecules and then a second 130.2 nm photon (within the same laser pulse) excites the oxygen atoms to the $^3S_1$ state. A 305 nm photon from another dye laser then promotes the oxygen atoms to high-n Rydberg levels. The atoms drift to a microchannel plate where they are field ionized and counted as a function of arrival time and laboratory angle.[26]

Several different studies of molecular photoionization in our laboratory indicate that the VUV pulse energies produced near 130 nm are very similar to those obtained at 125 nm. On the basis of calculated χ values,[20] this is anticipated. Typical time-of-flight spectra for $O(^3P_2)$ products are shown in Figure 2.6. The peak at shorter arrival time corresponds to $O(^3P_2)$ recoiling from $O(^3P_{0,1,2})$ and the peak at later time corresponds to $O(^3P_2)$ recoiling from $O(^1D_2)$. The absolute signal levels using VUV pulses generated in Hg vapor are greater by more than two orders of magnitude compared to that obtained previously under otherwise similar conditions using the 2-1 mixing scheme in Kr employing tunable lasers at 212.55 and 580 nm.[26,31,32] Since the observed signals result from absorption of two 130 nm photons, and either or both of the transitions may be saturated using the high intensity VUV source, it is difficult to make quantitative statements about the relative intensities based on these measurements. However, in

recent studies of the metastable O($^1S_0$) product signal from N_2O photodissociation at 130 nm, involving a single photon process, we observe signals that are a factor of ~300 times greater than using the previous method.[31] This is consistent with the expectation that our previous pulses were ~1 x 10^{11} photons/pulse for resonant (but not phase matched) 2-1 mixing in Kr[3,15] and our conclusions that the 130 nm intensities are comparable to those produced near 125 nm, measured to be 3 x 10^{13} photons/pulse. The large increase in 130.2 nm laser intensities, combined with the much smaller background levels resulting from removing the UV and visible laser beams opens up the possibility to study a range of chemical reactions producing ground state oxygen atoms in crossed molecular beams, such as $H + O_2 \rightarrow OH + O$.

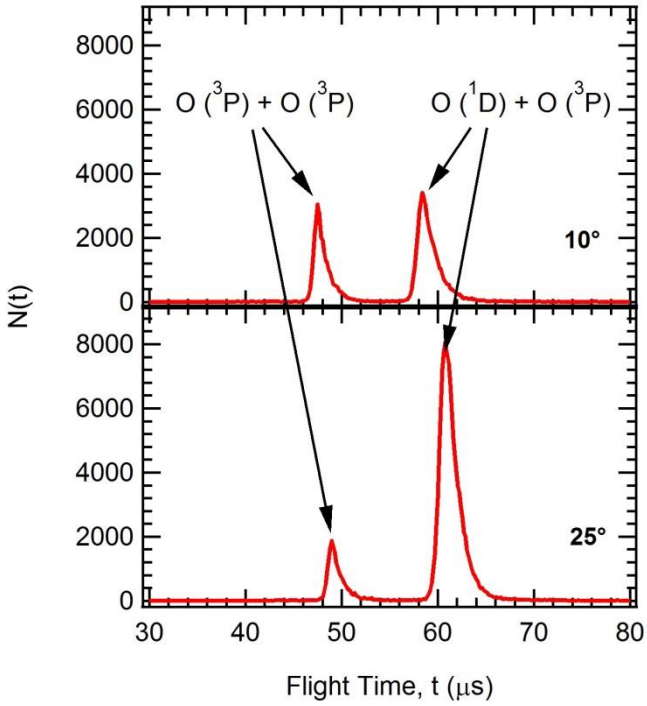

Figure 2.6: Time-of-flight spectra for O($^3P_2$) atoms produced by O_2 photodissociation at 130.2 nm monitored by ORTOF. Laboratory angles are indicated.

We have not recorded VUV tuning curves in the 130 nm range similar to those shown in Fig. 2.5 near 125 nm. However, we have scanned ν_3 at various combinations of ν_1 and ν_2 in order to map out optimum phase matching curves and efficiencies. The behavior observed in these studies was very similar to that observed near 125 nm. Most notably, we found that the highest VUV intensities were always observed on the red side of the $^3P_1$ resonance, and VUV intensities did not change significantly within 200 cm^{-1} of the $^3P_1$ resonance.

Prospects for increased VUV Pulse Energies

As shown in Fig. 2.5, the greatest VUV intensities (0.10 mJ/pulse) were obtained using three tunable dye lasers with ν_1 tuned to the low energy side of the 6^3P_1 resonance. An input pulse energy of 2.7 mJ at 255 nm corresponds to 3.46×10^{15} photons/pulse. Using our measured VUV intensity of 6×10^{13} photons/pulse at 125 nm corresponds to a 1.7% conversion efficiency from the UV to VUV. This is a factor of about 3 smaller than the 5% conversion efficiency reported by Muller and coworkers using three pulse amplified ring dye lasers, which produced 1.1 mJ VUV pulses at 130 nm.[21] Note that our final pulse energies (0.1 mJ) are about a factor of ten smaller.

Laser power dependence measurements in our laboratory revealed that the VUV intensities increase approximately linearly with 255 nm pulse energies up to 2.7 mJ, with no evidence for the onset of saturation in the conversion efficiency with increasing ν_1 pulse energies. On the other hand, using 2.7 mJ pulses at 255 nm, further increases in pulse energies at 404 nm and 625 nm produce increases in VUV intensities that are much less than linear, suggesting the onset of saturation in conversion efficiencies for ν_2 and ν_3 under our experimental configuration. In the work of Muller, 255 nm pulse energies were 10 mJ, with pulse durations of 2.2 ns.[21] Since our

pulse intensities were a factor of 3 smaller, and pulse duration (~7 ns) a factor of three greater, it is tempting to attribute the order of magnitude smaller VUV intensities produced in our work to the order of magnitude smaller 255 nm laser powers we employed.

On the basis of our measurements, the most obvious way to further increase our VUV pulse energies is by increasing the 255 nm pulse energy. In our experiments to date, the 255 nm pulse energies were limited to 2.7 mJ by the available Nd:YAG pump energy and relatively low efficiency for third harmonic generation starting with a 765 nm dye laser. We attempted to obtain higher 255 nm pulse energies by frequency doubling the 510 nm radiation from a 355 nm pumped dye laser, or by mixing the 532 nm from the Nd:YAG laser with 480 nm produced by a 355 nm pumped dye laser. However, in both cases the maximum pulse energies were still ~ 3 mJ. However, by employing a second Nd:Yag laser for pumping the three dye lasers, and/or by employing a different nonlinear mixing scheme for production of 255 nm light (e.g., doubling of 666 nm light to 333 nm followed by mixing with 1064 nm), achieving 255 nm pulse energies of ~10 mJ should be feasible. We note that by employing a second Nd:YAG pump laser, higher pulse energies at 404 nm and 625 nm (or 777 nm) can also be obtained. Thus, on the basis of our power dependence measurements, by employing 255 nm pulse energies in the 10 mJ range, at least a threefold increase in VUV pulse energies, i.e.,~0.3 mJ/pulse should be readily achievable.

Detailed modeling of the four-wave mixing process to generate 130.2 nm radiation has been carried out, with the primary aim being to maximize conversion efficiencies.[33,34] A number of considerations were presented in these papers that, if implemented, may lead to substantial improvements to the efficiencies reported here. To date, however, we have not employed these concepts to improve conversion efficiencies. We have also not yet attempted to improve the laser beam spatial profiles by spatial filtering of the dye laser beams prior to amplification. Also,

the beam diameters of the three laser beams were set to be nominally equal by employing the same telescope configurations in each laser prior to final amplification. We have not attempted to quantitatively match (using a laser beam profiler) the spatial beam diameters of the three input beams prior to mixing. We have not devoted any effort to optimizing conversion efficiencies by simultaneously varying the diameters of the three input laser beams. Also, in the original work of Muller and coworkers, considerable effort was devoted to ensuring that the heatpipe temperature was uniform throughout using a secondary enclosure. As noted in our experimental section, other than wrapping the heatpipe with copper foil, we have not taken great care to ensure homogeneous temperature. Clearly, many experimental parameters are subject to substantial further optimization, leading to further increases in VUV pulse energies. From these considerations, we believe that with some care, pulse energies in the 1 mJ range near 125 nm or 130 nm are within reach using commercial nanosecond dye lasers.

Generation of VUV at 120 nm < λ < 125nm

The calculations by Smith and Alford cover VUV energies up to 83,100 cm^{-1}, *i.e.,* down to $\lambda \approx 120$ nm.[20] Behavior similar to that shown in Figures 2.3 and 2.4 was observed. The VUV conversion efficiencies are expected to decrease at shorter wavelengths due to the smaller χ_{VUV}. While this range includes Lyman-α at 82,259 cm^{-1}, χ_{VUV} is very small for Hg at this specific wavelength, so conversion efficiencies will be substantially smaller than those reported in this paper. Consequently, resonance enhanced difference frequency mixing in Kr/Ar mixtures ($\nu_{VUV} = 2\nu_1 - \nu_2$) is likely to remain the best approach for VUV generation at Lyman-α.[3] We note, however, that using $\lambda_1 = \lambda_2 = 312.85$ nm and $\lambda_3 = 581$ nm, producing VUV at 123 nm near the 10 P resonance, gives similar intensities to VUV production at ~125 nm.

Generation of VUV at λ < 120 nm

Because of the reduced transmission of the MgF_2 output window at shorter wavelengths, we have not carried out extensive studies at λ< 120 nm using collimated input laser beams in Hg. However, during the course of this work, we found that substantial VUV intensities are generated near 11.0 eV ($\lambda \approx$ 112.7 nm) using only two lasers with λ_1 = 255 nm, λ_2 = 404 nm and λ_3 = 404 nm, corresponding to VUV energies well above the Hg^+ limit at 84184 cm^{-1}. Relatively strong photoionization signals were observed, despite the fact that the transmission through our MgF_2 lens must be very small (<10%). Since an excited state of Hg lies at 88759 cm^{-1}, it is perhaps not surprising that VUV generation is efficient near 11.0 eV. Using an off-axis MgF_2 lens configuration, the 112.7 nm light is spatially dispersed from the 125 or 130.2 nm beams, and would normally not contribute. It is important to keep in mind, however, that with λ_1 = 255 nm and λ_2 = 404 nm (*e.g.*, for producing light at 130.2 or 125 nm), in the absence of a dispersing element, significant VUV light at 112.7 nm is likely to be present, especially if a LiF optic is used as the VUV exit window.

It is well-known that Hg facilitates efficient production of radiation at wavelengths well below the LiF cutoff at 104 nm.[35,36] The most challenging aspects of generation of light in the extreme ultraviolet (XUV) is designing a cell facilitating windowless operation, and developing a method for spatially isolating the XUV without energy losses inherent to dispersive elements such as gratings. We have recently been working on the generation of light at energies up to 13 eV, and have made considerable progress in both of these areas.[37]

Conclusions

Generation of intense pulsed VUV radiation (6 x 10^{13} photons/pulse) has been demonstrated using resonance-enhanced four-wave mixing of unfocussed pulsed commercial dye lasers in Hg vapor. The tuning curves for a number of different resonant two-photon combinations have been measured and agree well with the predictions of Smith and Alford.[20] While the highest conversion efficiencies (1.7% from UV to VUV) and peak intensities are achieved using three independently tunable dye lasers, two somewhat simpler schemes employing two dye lasers are characterized. Our studies indicate that under our experimental conditions, VUV pulse energies are limited by the available input pulse energies at 255 nm and that further increases in VUV pulse energies to the mJ range should be readily achievable.

REFERENCES

1. D. N. Nikogosyan, *Nonlinear Optical Crystals: A Complete Survey* (Springer Science Inc., New York, 2005).

2. R. Hilbig and R. Wallenstein, Appl. Opt., **21**, 913 (1982).

3. J.P. Marangos, N. Shen, H. Ma, M.H.R. Hutchinson and J.P. Connerade, J. Opt. Soc. Am. B, **7**, 1254 (1990).

4. E. Cromwell, T. Trickl, Y.T. Lee and A.H. Kung, Rev. Sci. Instrum., **60,** 2888 (1989).

5. S.J. Hanna, P. Campuzano-Jost, E.A. Simpson, D.B. Robb, I. Burak, M.W. Blades, J.W. Hepburn and A.K. Bertram, Int. J. Mass. Spec., **279**, 134 (2009).

6. S. Souma, T. Sato, T. Takahashi and P. Baltzer, Rev. Sci. Instrum. **78**, 123104 (2007).

7. F. Mühlberger, J. Wieser, A. Morozov, A. Ulrich and R. Zimmermann, Anal. Chem. **77,** 2218 (2005).

8. R. Flesch, M.C. Schürmann, M. Hunnekuhl, H. Meiss, J. Plenge, and E. Rühl, Rev. Sci. Instrum. **71,** 1319 (2000).

9. X. Yang, J. Lin, Y.T. Lee, D.A. Blank, A.G. Suits and A.M. Wodtke, Rev. Sci. Instrum. **68**, 3317 (1997).

10. S-H. Lee, C-H. Chin, W-K. Chen, W-J. Huang and C-C. Hsieh, Phys. Chem. Chem. Phys. **13**, 8515 (2011).

11. G.C. Bjorklund, IEEE J. Quantum Electron. **QE-11**, 287 (1975).

12. R.Mahon, T.J. McIlrath, V.P. Myerscough and D.W. Koopman, IEEE J. Quant. Electron. **QE-15**, 444 (1979).

13. H. Langer, H. Puell and H. Röhr, Opt. Comm. **34**, 137 (1980).

14. R. Hilbig and R. Wallenstein, IEEE J. Quant. Electron. **QE-17**, 1566 (1981).

15. G. Hilber, A. Lago, and R. Wallenstein J. Opt. Soc. Am. B **4**, 1753 (1987).

16. B.R. Strazisar, C. Lin and H.F. Davis, Science **290**, 958 (2000).

17. L. Hanley and R. Zimmermann, Anal. Chem. **81**, 4174 (2009).

18. R. Mahon and F.S. Tomkins, IEEE J. Quant. Electron. **QE-18**, 913 (1982)

19. R. Hilbig and R. Wallenstein, IEEE J. Quant. Electron. **QE-19**, 1759 (1983).

20. A.V. Smith and W.J. Alford, J. Opt. Soc. Am. B **4**, 1765 (1987).

21. C.H. Muller, D.D. Lowenthal, M.A. DeFaccio and A.V. Smith, Opt. Lett. **13**, 651 (1988).

22. R.G. Caro, A. Costela and C.E. Webb, Opt. Lett. **6**, 464 (1981).

23. K. S. E. Eikema, J. Walz and T.W. Hänsch, Phys. Rev. Lett. **83**, 3828 (1999).

24. D. Kolbe, M. Scheid and J. Walz, Phys. Rev. Lett. **109**, 063901 (2012).

25. D.R. Albert and H.F. Davis, J. Phys. Chem. Lett. **1**, 1107 (2010).

26. C. Lin, M.F. Witinski and H.F. Davis, J. Chem. Phys. **119**, 251 (2003).

27. P.A. Willis, H.U. Stauffer, R.Z. Hinrichs and H.F. Davis, Rev. Sci. Instrum. **70**, 2606 (1999)

28. D. Proch and T. Trickl, Rev. Sci. Instrum. **60**, 713 (1989).

29. D.L. Proctor, D.R. Albert, and H. F. Davis, Rev. Sci. Instrum. **81**, 023106 (2010).

30. M. Xie, Z. Zhou, Z. Wang, D. Chen and F. Qi, Int. J. Mass. Spec. **303**, 137 (2011).

31. M.F. Witinski, M. Ortiz- Suárez and H.F. Davis, J. Chem. Phys. **122**, 174303 (2005).

32. M.F. Witinski, M. Ortiz-Suárez, and H.F. Davis, J. Chem. Phys. **124**, 094307 (2006).

33. A.V. Smith, W.J. Alford, and G.R. Hadley, J. Opt. Soc. Am. B **5**, 1503 (1988).

34. A.V. Smith, G.R. Hadley, P. Esherick and W.J. Alford, Opt. Lett. **12**, 708 (1987).

35. C.H. Kwon, H.L. Kim, and M.S. Kim, Rev. Sci. Instrum. **74**, 2939 (2003).

36. P.R. Herman and B.P. Stoicheff, Opt. Lett. **10**, 502 (1985).

37. M.A. Todd, D.A. Albert and H. F. Davis, unpublished.

CHAPTER 3: Experimental Methods

Crossed Molecular Beam Scattering

The experiments were carried out using a rotatable source, fixed detector crossed molecular beams apparatus (Figure 3.1).[1] The phenyl beam was produced via photolysis of chlorobenzene at 193 nm.[2] A beam of chlorobenzene (Aldrich) (~10 Torr) seeded in ~1800 Torr of H_2 was produced via a pulsed piezoeletrically actuated supersonic expansion.[3] A pulsed excimer laser (GAM EX-10) operating at 193 nm then photolyzed the precursor forming primarily phenyl radicals and chlorine atoms.[52] The laser was mounted to the source assembly and rotated with it maintaining good alignment for all source positions. The output of the excimer laser, which provided ~10 ns pulses (10 mJ) was gently focused to a 6 mm x 2 mm spot directly in front of the orifice of the pulsed valve. For reactive scattering experiments, the phenyl beam (<v> = 2200 m/s, speed ratio = 11) passed through a 2 mm diameter skimmer (Precision Instruments) into the main chamber region, maintained at or below 5 x 10^{-6} Torr. In nonreactive scattering experiments an additional stage of differential pumping was employed with the beam skimmed by a 2 mm diameter skimmer and then further collimated with a square (3 mm x 3 mm) knife-edge defining aperture fabricated using four razor blades**.** In all experiments, the molecular beam was collimated by a 2 mm diameter skimmer (Precision Instrument) before entering the main chamber and crossing the phenyl beam at a 90˚ collision angle. Beam parameters (gas mixture, <v>, and speed ratio) for the molecular beams (O_2, N_2, C_3H_6 and C_4H_8) along with the corresponding center of mass angle and collision energy for collisions with the phenyl radical beam are given in Table 3.1. The molecular beam was characterized in a separate series of experiments by monitoring its time-of-flight (TOF) distributions on-axis using a slotted chopper wheel with a mass spectrometer detector employing

electron impact ionization detection. Scattered species traveled 24.1 cm through a series of three apertures and were ionized by a single VUV photon at 9.9 eV in a detector region maintained below 1 x 10^{-9} Torr. The resulting positive ions were mass selected using a quadrupole mass filter (Extrel Merlin with 0.75″ rods) and detected using a conversion dynode/electron multiplier operating in pulse counting mode.

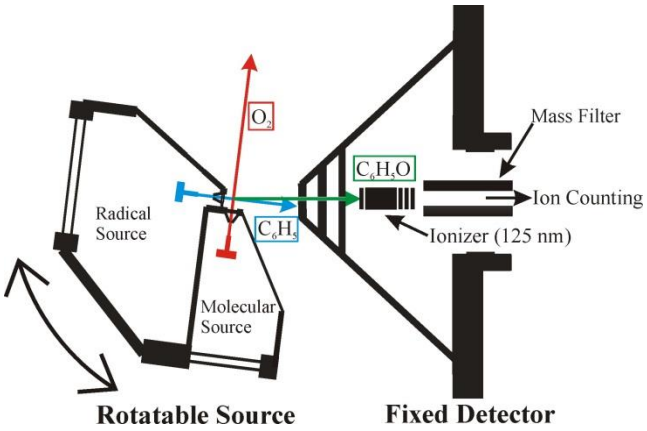

Figure 3.1: Schematic of the Cornell fixed detector, rotatable crossed molecular machine.

Table 3.1: Beam parameters for crossed molecular beam experiments with phenyl radicals

Gas Mixture	Beam Velocity (m/s)	Speed Ratio (v/Δv)	Collision Energy (kJ/mol)	CM Angle (degrees)
40% O_2 in He	950	12	64	10
40% N_2 in He	970	14	59	9
3% O_2 in H_2	1870	10	97	20
25% C_3H_6 in He	1050	12	84	14
9% C_3H_6 in H_2	1700	10	108	22
25% C_4H_8 in He	960	12	97	17

TOF spectra were generated at a given laboratory angle by scanning the delay of the 9.9 eV light source relative to that of the 193 nm excimer laser that produced phenyl radicals. The laboratory angular distribution was generated by integrating the TOF spectra at each given angle. The TOF spectra were fit using the forward convolution technique, taking as inputs instrumental parameters as well as center-of-mass (CM) distribution functions, namely P(E), the CM translational energy release, and T(Θ), the CM angular distribution, and outputting calculated laboratory TOF and angular distributions.[4] The two CM functions were iteratively adjusted until the calculated TOF and angular distributions matched their experimental counterparts.

Radical Beam Production and Characterization

Production of molecular free radicals can be achieved via a variety of techniques: photolysis[5], pyrolysis[6], electrical discharge[7], chemical reaction[8], etc.. In most of these cases a relatively weak bond of a stable precursor is cleaved to generate the corresponding radical. The weak bond also often fragments upon ionization using traditional (~80 eV) electron impact. Because of the tendency of the precursor to fragment to the same mass as the radical of interest, detection of production of the radical species is often difficult. In special cases (OH[9], CN[10,11,12], CH_3[13], etc.) the spectroscopy of the radical species is known and can be detected using LIF or REMPI, but for larger molecular free radicals this is generally not the case.

By employing "soft" ionization, fragmentation of the parent species can be reduced or eliminated, allowing for clean detection of the radical species even when looking directly on-axis. This allows for convenient optimization for the production of molecular radicals. As can be seen in Figure 3.2 the production of phenyl radicals on-axis from the photodissociation of chlorobenzene is undetectable using traditional electron impact. The chlorobenzene parent

fragments substantially to the parent mass of phenyl radicals (m/e = 77). When using "soft" single photon ionization, fragmentation of chlorobenzene to m/e = 77 is negligible and the enhancement of m/e = 77 when phenyl radicals are produced is apparent (Figure 3.2). The easy detection of production of phenyl radicals allows for straightforward optimization of the phenyl radical beam. For instance, we found that modest photolysis laser powers (~10 mJ per pulse) produced the most intense phenyl radical beams, since at higher laser powers secondary photochemistry depletes the phenyl radicals that are initially formed. "Soft" ionization also allows for the straight-forward determination of beam impurities which can potentially interfere with detection of the desired product species in molecular beam scattering experiments.

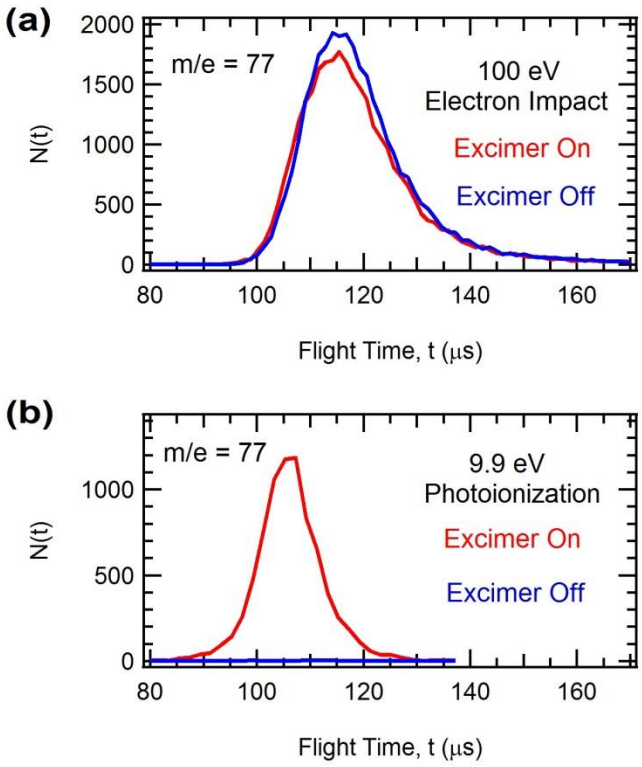

Figure 3.2: Looking directly (0˚) into the phenyl radical/chlorobenzene beam at m/e = 77. When the excimer laser is off (blue curve) the beam contains only of chlorobenzene molecules. When the excimer laser is on (red curve) the beam contains phenyl radicals and chlorobenzene molecules. (a) Product detection using 100 eV electron impact ionizer. (b) Product detection using 9.9 eV photoionization light source.

Comparison of 9.9 eV Light Source with Previous Techniques

We have examined the reaction $Zr + CH_4 \rightarrow ZrCH_2 + H_2$ to compare product detection using our new 9.9 eV light source with a 7.9 eV light source (F_2 excimer laser) and electron impact ionization (Figure 3.3). The best signal level when comparing these different approaches was the 7.9 eV light source, its signal level was approximately a factor of five greater than that for the 9.9 eV light source which in turn was about another factor of five greater in absolute signal level than using 100 eV electron impact. The signal to noise ratio was even better than the factor of five increase in signal level as can be seen with the different TOFs in Figure 3.3. For studying $Zr + CH_4 \rightarrow ZrCH_2 + H_2$, the 9.9 eV light source is significantly better than the electron impact ionization scheme. The 9.9 eV light source opens up a variety of systems that are unobtainable using the 7.9 eV light source, such as more catalytically relevant transition metal reactions (Pt, Pd, etc.) as well as many reactions of hydrocarbon free radicals.

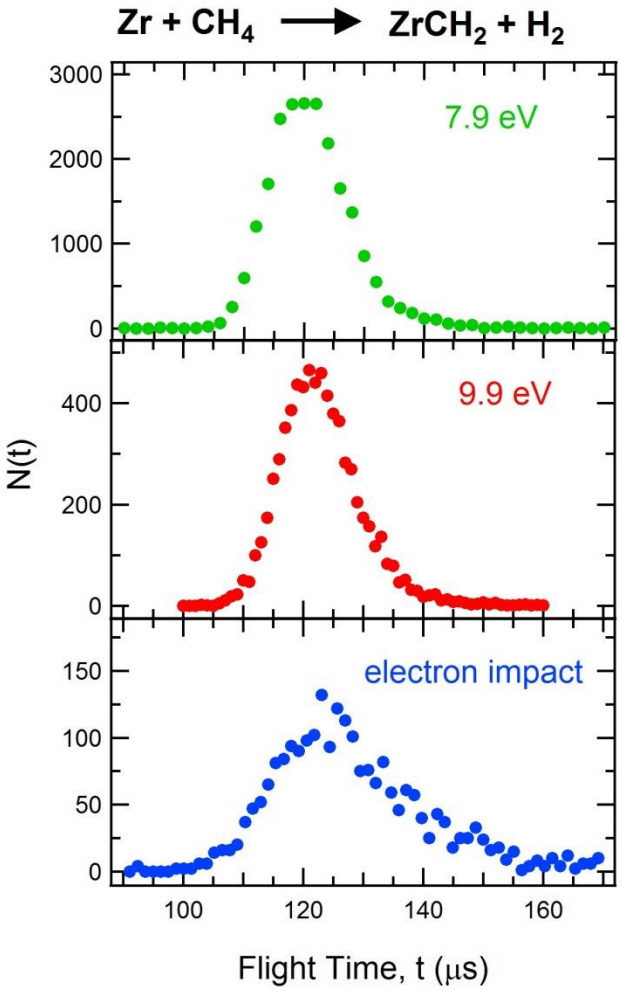

Figure 3.3: Time-of-flight distributions at the center-of-mass angle monitored at m/e = 105 ($ZrCH_2^+$) for Zr + CH_4 → $ZrCH_2$ + H_2. The top panel (green) is monitored using an F_2 excimer laser at 7.9 eV for single photon ionization. The middle panel (red) is monitored using the 9.9 eV photoionization light source. The bottom panel (blue) is monitored using electron impact ionization. All of the distributions have the same total counting time.

REFERENCES

1. P.A. Willis, H.U. Stauffer, R.Z. Hinrichs and H.F. Davis, Rev. Sci. Instrum. **70**, 2606 (1999).

2. N.E. Sveum, S.J. Goncher and D.M. Neumark, *Phys. Chem. Chem. Phys.*, **8**, 592 (2006).

3. D.L. Proctor, D.R. Albert and H.F. Davis, *Rev. Sci. Instrum.,* **81**, 023106 (2010).

4. P.A. Willis, H.U. Stauffer, R.Z. Hinrichs and H.F. Davis, *J. Phys. Chem. A,* **103**, 3706 (1999).

5. H.F. Davis, J. Shu, D.S. Peterka and M. Ahmed, *J. Chem. Phys.*, **121**, 6254 (2004).

6. D.W. Kohn, H. Clauberg, and P. Chen, *Rev. Sci. Instrum.*, **63**, 4003 (1992).

7. E.N. Sharp, M.A. Roberts and D.J. Nesbitt, *Phys. Chem. Chem. Phys.*, **10**, 6592 (2008).

8. V. Aristov, D. Conroy and H. Reisler, *Chem. Phys. Lett.,* **318**, 393 (2000).

9. J.M. Beames, F. Liu, M.I. Lester and C. Murray, *J. Chem. Phys.*, **134,** 241102 (2011).

10. R. Engleman, *J. Mol. Spectrosc.*, **49**, 106 (1974).

11. F. Leonori, K.M. Hickson, S.D. Le Picard, X. Wang, R. Petrucci, P. Foggi, N. Balucani and P. Casavecchia, *Mol. Phys.*, **108,** 1097 (2010).

12. P. Maksyutenko, D.S.N Parker, F. Zhang and R.I. Kaiser, *Rev. Sci. Instrum.*, **82**, 083107 (2011).

13. K. Liu, *Phys. Chem. Chem. Phys.*, **9**, 17 (2007).

CHAPTER 4: Collision Complex Lifetimes in the Reaction $C_6H_5 + O_2 \rightarrow C_6H_5O + O$

Introduction

The phenyl radical (C_6H_5) is ubiquitous in combustion, and is a key intermediate in the production of polycyclic aromatic hydrocarbons (PAHs), which serve as precursors to soot formation.[1] Prototypical reactions of the phenyl radical in combustion include those with molecular oxygen (O_2) and with various hydrocarbons. Understanding the mechanisms for these reactions and quantifying the branching ratios for competing channels is crucial to modeling soot production in real and complex combustion environments.[2] The mechanisms for formation of PAHs involve the formation of phenyl radicals and their subsequent reactions with unsaturated hydrocarbons. The most prominent pathway is the hydrogen-abstraction acetylene-addition (HACA) mechanism, in which large PAHs are generated by stepwise addition of smaller hydrocarbons.[3] During the formation of PAHs, the generation and subsequent reaction of phenyl radicals is a key first step. The reaction of phenyl radicals with molecular oxygen can serve to interrupt HACA-like mechanisms and, depending on the reaction products, suppress or enhance PAH growth.[2] Much work has been done, both theoretically[4,5,6,7] and experimentally,[8,9,10,11,12] to understand the mechanism of phenyl oxidation.

Crossed molecular beam studies in conjunction with theoretical calculations have been instrumental in addressing mechanistic questions for small systems containing 4 atoms or less. For such systems, direct dynamics simulations employing accurate potential energy surfaces may be compared to detailed experimental measurements of product angular and velocity distributions.[13,14,15,16] More recently, there has been considerable effort aimed at using ideas gained from small systems to better understand reactions involving larger polyatomics.[17,18]

Unfortunately, when the number of atoms becomes large, direct dynamics calculations and the calculation of accurate potential energy surfaces becomes too complex. A much simpler approach for reactions involving initial formation of intermediates followed by several decomposition channels is to calculate the geometries and energies of key intermediates and transition states. One may then use statistical theories, such as Rice-Ramsperger-Kassel-Marcus (RRKM) theory, to predict rate constants and product branching ratios.[17] The RRKM theory, if applicable to the system of interest, is appealing in its simplicity.[19] Microcanonical reaction rate constants (and therefore branching ratios) for each competing pathway from a common intermediate may be calculated directly from calculated parameters, including the energetics, geometries, and vibrational frequencies for intermediates and key transition states along the reaction coordinate.

Parameters for key intermediates and transition state geometries for the reaction of phenyl radicals with molecular oxygen have been calculated by Tokmakov *et al.*[6] The reaction is characterized by addition, forming phenylperoxy (C_6H_5OO) intermediates lying ~195 kJ/mol below the reactants. These intermediates can subsequently decompose via simple O-O bond fission to form phenoxy radicals (C_6H_5O) plus ground state oxygen atoms, $O(^3P)$, with an exoergicity relative to reactants of ~36 kJ/mol. Alternatively, the reaction can proceed by isomerization of C_6H_5OO to 2-oxepinyloxy radicals, followed by unimolecular rearrangements producing other products, including $C_6H_4O_2$ + H, C_5H_5 + CO_2 and C_5H_5O + CO. A simplified potential energy diagram for the C_6H_5O + O channel and energetics for the other reaction channels predicted by Takmakov *et al.* are shown in Figure 4.1.[6] To date, crossed molecular beam experiments at a variety of collision energies have only detected the C_6H_5O + O channel from simple O-O bond fission of the initially-formed C_6H_5OO.[20,21,22] Using the theoretical

calculations, the branching ratios between reaction products can be calculated with RRKM theory and compared to experimental results. In comparing calculated branching ratios with experimentally derived values, one must assume that RRKM theory is valid and that the potential energy surface is sufficiently accurate. If the calculations differ from the experimental results, one or both of these assumptions must be incorrect.

Previous experimental studies bring into question the applicability of RRKM theory for the $C_6H_5 + O_2$ reaction. In 2007, Gu and coworkers carried out the first crossed beams study, employing a phenyl radical beam produced by pyrolysis of nitrosobenzene (C_6H_5NO).[20] At a mean collision energy of 107 kJ/mol, the reaction dynamics were determined to be "rather direct via an extremely short lived phenylperoxy radical holding lifetimes of less than 0.01 ps."[20] The occurrence of a direct reaction with lifetimes an order of magnitude shorter than the O-O vibrational period of the C_6H_5OO complex (~ 0.10 ps, i.e., ~100 fs) is surprising, given the deep potential well for the C_6H_5OO intermediates, modest exoergicity for the $C_6H_5O + O$ products, and the 33 vibrational degrees of freedom available for a 13 atom system.

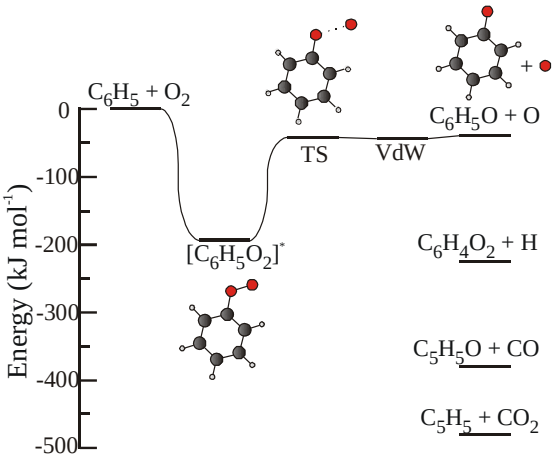

Figure 4.1: Simplified potential energy diagram for $C_6H_5 + O_2 \rightarrow C_6H_5O + O$ reaction, where TS is transition state for O-O bond fission and VdW is Van der Waals complex between the phenoxy radical and oxygen atom. Overall energetics for other major reaction channels predicted by Tokmakov et al. are shown. Adapted from ref. 6.

Recently, Parker and coworkers have reexamined the $C_6H_5 + O_2$ reaction system at a much lower collision energy (38 kJ/mol), using a photolytic phenyl radical source.[22] They found that at their lower collision energy, the C_6H_5OO intermediates are long-long lived relative to their rotational period, consistent with RRKM theory. In addition, they have apparently reinterpreted their original high collision energy data (107 kJ/mol) by invoking an "osculating" complex model, rather than the direct stripping mechanism assumed earlier. In the "osculating" complex model, the lifetimes of intermediates are comparable to their rotational periods. Under such conditions, the intensity of products scattered "forward" relative to "backward" in the center-of-mass (CM) reference frame, $I(0^o)/I(180^o)$, is very strongly dependent upon the lifetimes of intermediates, with this quantity increasing sharply with decreasing lifetimes relative to rotational periods. This reinterpretation of their original high collision energy data, with no new data or justification, has led the authors to suggest a CM angular distribution with the intensity of the forward peak relative to the backward peak, $I(0^o)/I(180^o)$ of 9 ± 4.[22] This mean value leads to lifetimes for the C_6H_5OO in the 300 fs range (rather than <10 fs as originally concluded). We have conducted crossed molecular beam studies of phenyl radicals with molecular oxygen at collision energies of 64 kJ/mol and 97 kJ/mol using a photolytic phenyl radical source in order to understand the role of collision energy on the lifetimes of phenylperoxy intermediates.

Phenyl Radical Sources

Phenyl radicals were generated either by photolysis or by pyrolysis of commercially available precursors. In the photolytic source, phenyl radicals were generated by photodissociation of chlorobenzene (Aldrich) at 193 nm directly in front of the 1 mm orifice of a home-built piezoelectric pulsed valve.[23] A dilute mixture of chlorobenzene (~10 Torr) was seeded in hydrogen or helium carrier gas (~1800 Torr) by bubbling the carrier gas through a

liquid sample held at room temperature. The ~8 mJ/pulse output of a 193 nm excimer laser (GAM EX10 or Lambda Physik Compex) was loosely focused to a 2 mm x 6 mm spot directly in front of the pulsed valve nozzle, producing primarily phenyl radicals and chlorine atoms.[24]

The pyrolytic phenyl radical source employed supersonic expansion of nitrosobenzene (Aldrich) seeded in helium (1000 Torr). The nitrosobenzene beam was generated by passing the helium carrier gas over solid nitrosobenzene held in a variable temperature bath. The concentration of nitrosobenzene in the beam was varied by changing the bath temperature (4 ^{o}C – 21 ^{o}C). The pyrolytic source consisted of a silicon-carbide tube (2 mm OD and 1 mm ID) attached to the output of a piezoelectric pulsed valve (1 mm orifice) via a water-cooled support block. The 0.5 cm long heated region of the silicon-carbide tube was resistively heated to temperatures between 1200 °C and 1500 °C, as measured using an optical pyrometer. The nitrosobenzene, when heated, primarily dissociates to form phenyl and NO radicals.

In order to compare the different phenyl radical sources, experiments were carried out using a two-chamber fixed beam apparatus. The pulsed phenyl radical beam was generated in a source chamber, passed through a 1 mm diameter conical skimmer, and then entered a second chamber housing a Wiley-McLaren time-of-flight mass spectrometer.[25] A fraction of the beam was ionized by the 9.9 eV radiation generated via 4-wave mixing in mercury vapor with a focused geometry.[26] Ions were accelerated to a constant kinetic energy, allowed to drift ~1 m, and detected with a dual microchannel plate in the chevron configuration. The output was amplified by a fast pre-amp (ORTEC) and sent to a multi-channel scalar (Stanford Research Instruments) to generate arrival time distributions which were then transformed to mass spectra.

Nonreactive Scattering of C_6H_5 from O_2 and N_2

Crossed-molecular-beams experiments were performed with a rotatable sources machine[27] where the phenyl radical beam intersected a pulsed beam of O_2 or N_2 at a right angle, leading to mean collision energies of ~64 kJ/mol. Products traveled 24.1cm before being ionized by 9.9eV photons, mass filtered, and detected as a function of arrival time. Time-of-Flight (TOF) spectra were recorded at various laboratory angles monitoring $C_6H_5^+$, m/e = 77, from nonreactive scattering of phenyl radicals from O_2 or N_2.

When a phenyl radical encounters an O_2 molecule, phenylperoxy (C_6H_5OO) intermediates (located ~200 kJ/mol below the reactants) can be formed. These intermediates can decompose to a variety of new reaction products or back to reactants.[6] However, elastic and inelastic nonreactive collisions also occur, without formation of C_6H_5OO. By studying the nonreactive scattering of phenyl radicals with molecular oxygen, we can gain insight into such nonreactive collisions. The C_6H_5 TOF spectra for nonreactive scattering were obtained by subtracting TOF spectra with the O_2/N_2 beam off from TOF spectra with the O_2/N_2 beam on at various angles. The nonreactive TOFs for phenyl radicals scattering from O_2 and N_2 are shown in Figure 4.2. Nonreactive scattering of C_6H_5 from both O_2 and N_2 can be fit with identical P(E) and T(θ) distributions (Figure 4.3). The similarity between the nonreactive scattering from both O_2 and N_2 and the lack of intensity in the backward direction, which would correspond to long-lived C_6H_5OO complexes decaying back to $C_6H_5 + O_2$, implies that most C_6H_5OO intermediates decay to new reaction products and not back to reactants.[6] The absence of background from fragmentation of chlorobenzene producing $C_6H_5^+$ at m/e = 77 facilitates the study of nonreactive scattering even at angles very close to the phenyl radical beam.

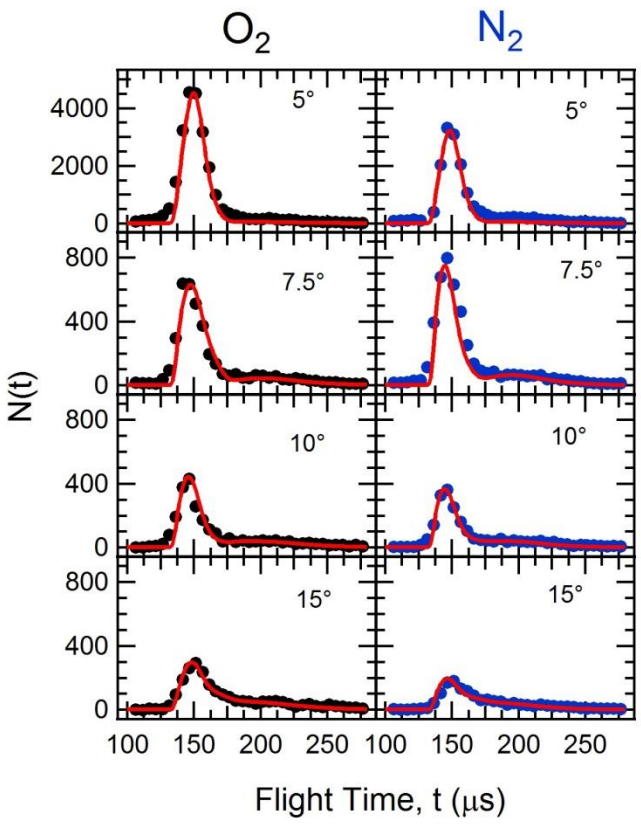

Figure 4.2: Time-of-flight distributions (m/e =77) at the indicated laboratory angle for non-reactive of scattering of phenyl radicals from O_2 (left panel, black) and N_2 (right panel,blue). All time-of-flight distributions are normalized to the same number of laser shots per point.

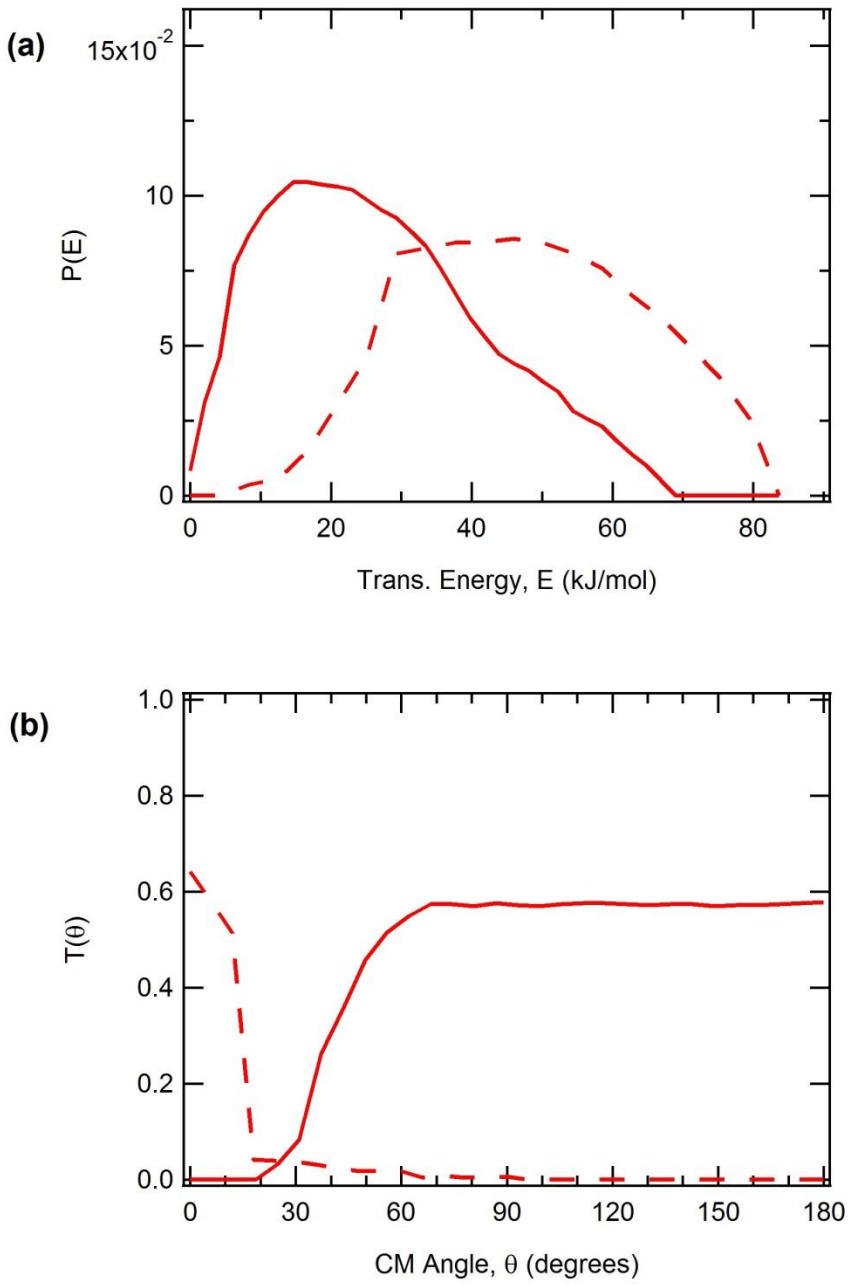

Figure 4.3: Center–of-mass distributions (m/e = 77) used to fit the non-reactive scattering of phenyl radicals from O_2 and N_2 (same distributions used for both O_2 and N_2). Both a forward scattered component (dotted line) and a sideways/backward scattered component (solid line) were used to fit the data. The scaling factor of forward component to the sideways/backward component was 4:1.

Calculations indicate that O-O bond fission in C_6H_5OO producing $C_6H_5O + O$ (^3P) has no potential energy barrier above the reaction endoergicity, $D_o(C_6H_5O\text{-}O) = 156$ kJ/mol.[6] The low barrier for production of $C_6H_5O + O$ is consistent with our finding that most of the C_6H_5OO intermediates decay to new reaction products. The other energetically accessible channels require multiple isomerization steps.[6] Consequently, the lifetimes of the C_6H_5OO intermediates, which are largely determined by the rate of O-O bond fission in C_6H_5OO, play a critical role in determining branching ratios in this reaction.

$C_6H_5 + O_2 \rightarrow C_6H_5O + O$, E_{coll} = 64 kJ/mol

Time-of-flight (TOF) spectra were recorded at various laboratory angles for m/e = 93, $C_6H_5O^+$. Each TOF spectrum, shown in Figure 4.4, consists of ~30,000 laser shots, corresponding to ~20 min of data collection time. At angles close to the phenyl beam, a small amount of time-dependent background signal was present. By carrying out parallel studies in which a N_2/He mixture was used instead of an O_2/He mixture, this signal was found to result from non-reactive scattering of minor impurities in the phenyl beam. This signal was therefore subtracted out from each TOF spectrum.

The laboratory angular distribution was constructed by integrating each TOF spectra, as shown in Figure 4.5. The solid line fits to the laboratory angular distribution and TOF spectra were simulations of the experimental data calculated using the forward convolution technique described previously.[28] The optimized P(E) and T(Θ) for the $C_6H_5O + O$ channel are shown as solid lines in Figure 4.6.

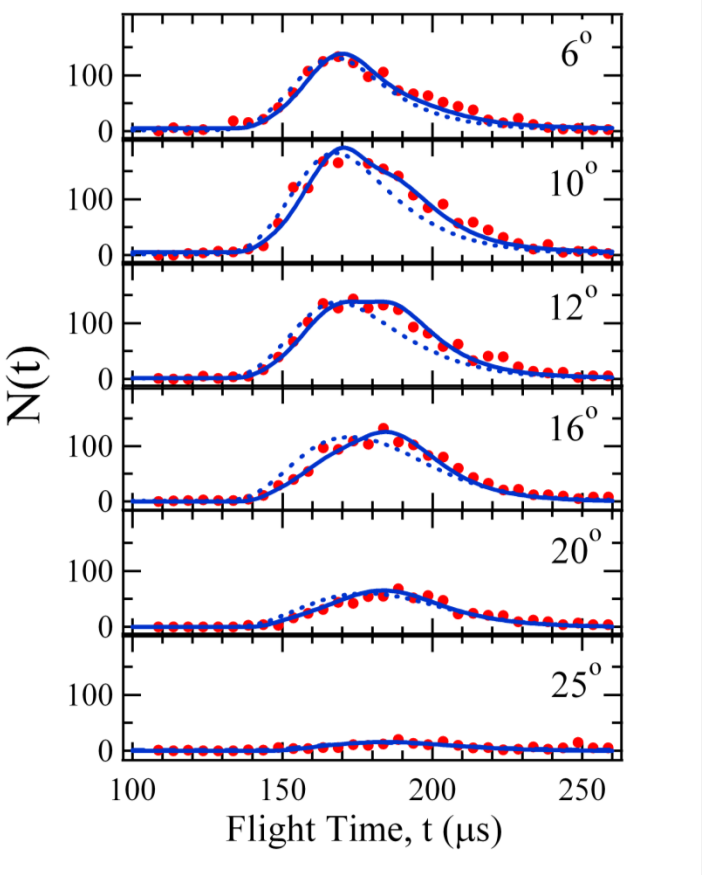

Figure 4.4: Measured TOF spectra obtained at various laboratory angles for $C_6H_5O^+$ (m/e = 93) products. Circles are experimental data; solid lines are calculated using optimized center-of-mass translational energy and angular distributions (Figure 4.6); dotted lines show fits using osculating complex angular distribution.

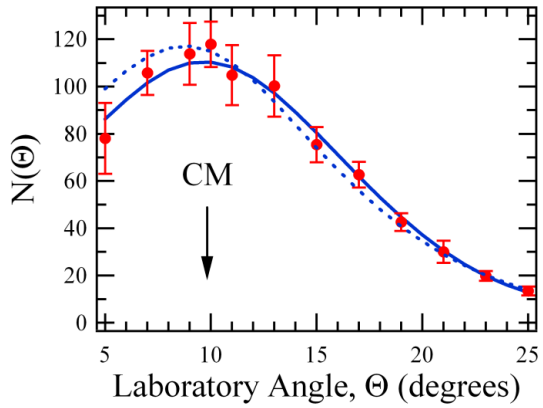

Figure 4.5: Laboratory angular distribution for C_6H_5O products. Circles are experimental data with 1σ error bars; solid line is calculated using optimized center-of-mass distributions; dotted line shows fit using osculating complex T(Θ) shown in Figure 4.6. Fits were scaled by minimizing χ^2. CM denotes the center-of-mass angle.

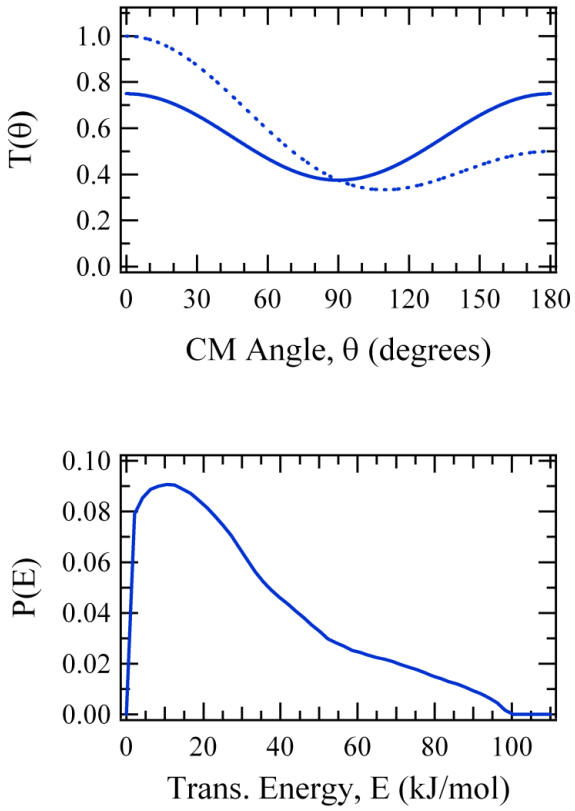

Figure 4.6: Solid Lines: Optimized C_6H_5O center-of-mass angular distribution, T(Θ), and translational energy distribution, P(E). Dotted Line: Osculating complex T(Θ)

We find that the P(E) peaks at low translational energy release, ~12 kJ/mol. This is characteristic of a reaction in which no significant potential energy barrier exists for O-O bond fission in C_6H_5OO above its endoergicity, *i.e.*, the maximum in the potential energy along the reaction pathway is primarily due to the centrifugal barrier, corresponding to decay via a "loose" transition state. This is consistent with calculations that predict no significant exit barrier for C_6H_5OO decomposition to $C_6H_5O + O$.[6]

The best fit center-of-mass angular distribution is forward-backward symmetric (Figure 4.6). A forward-backward symmetric angular distribution is characteristic of a reaction involving C_6H_5OO collision complexes with lifetimes of at least several rotational periods. Information about the lifetimes of intermediates can be inferred by analyzing the product center-of-mass angular distribution, $T(\theta)$.[31] If the $T(\theta)$ is strongly forward peaked, with zero intensity in the backward direction, the reaction is direct with the lifetimes of any intermediates much shorter than any rotational period *i.e.* traditional stripping dynamics.[29] A $T(\theta)$ that shows equal intensity in the forward and backward direction usually implies the existence of long-lived collision complexes, *i.e.* intermediates whose lifetimes are longer than a few rotational periods. Finally, a $T(\theta)$ with contributions in both the forward and backward direction but with asymmetry in favor of the forward direction is usually interpreted as either evidence for osculating complexes, *i.e.* intermediates whose lifetimes are *comparable* to a rotational period or as evidence for multiple reaction mechanisms, *i.e.* a forward scattered distribution superimposed with a symmetric distribution.[30] Crossed molecular beam scattering can only measure absolute lifetimes for intermediates whose lifetimes are comparable to a rotational period, for intermediates whose lifetimes are greater than ~ 4 rotational periods all that can be ascertained from the crossed molecular beam scattering data is an absolute minimum lifetime. The intermediates of long-

lived collision complexes could have lifetimes anywhere from four to thousands of rotational periods.

The shortest rotational times available to phenylperoxy intermediates, while still conserving the orbital angular momentum of the collision, are 0.5, 1.7 and 2.2 ps. We have tried to fit our data with an osculating complex CM angular distribution, as indicated by the dotted line in Fig. 4.6.[31,32] In Figures 4.4 and 4.5, we include the calculated laboratory angular and TOF distributions as dotted lines assuming decomposition of an osculating complex with a CM angular distribution shown as a dotted line in Figure 4.6. These calculated distributions do not simulate the experimental data as well as when a fully symmetric distribution was employed, indicating that the C_6H_5OO lifetimes are not likely to be as short as one rotational period.

Our conclusion that the reaction is dominated by formation of long lived collision complexes followed by simple O-O bond fission at a mean collision energy of 64 kJ/mol is significantly different from that of Gu et al.[20,21] They concluded that the reaction proceeded via a direct mechanism at a collision energy of 107 kJ/mol, near the spectator stripping limit, imposing a maximum C_6H_5OO lifetime of ~0.01 ps. This timescale is at least two orders of magnitude shorter than the lower limit inferred from our work. To better appreciate the large difference between our results, we have calculated the laboratory angular and TOF distributions using the center-of-mass translational energy P(E) and angular T(Θ) distributions similar to those presented in Ref 20.

Comparison of Experimental Results with Previous Findings

Laboratory angular and TOF distributions (Figure 4.7) were calculated using T(θ) and P(E) similar to that of Gu and coworkers, as well as with the optimized P(E) from this work along

with the T(θ) found by Gu (Figure 4.8). All of the spectra were calculated using the same beam and instrumental parameters as the optimized fit in our work. The P(E) similar to that of Gu *et al.* was scaled so that their largest translational energy release matched our largest translational energy release. In their experiment the collision energy was ~43 kJ/mol higher than in ours causing their P(E) to extend out to higher energies (~145 kJ/mol).

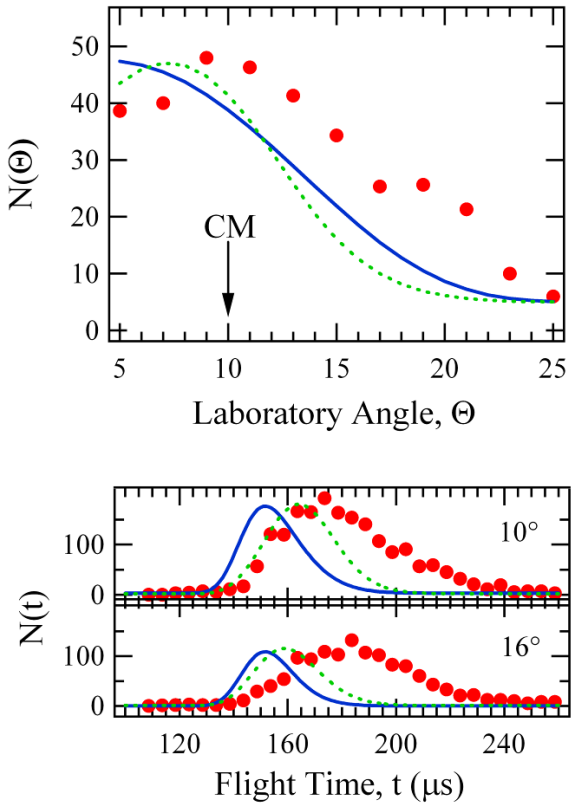

Figure 4.7: Laboratory angular distribution and TOF spectra, circles are experimental data; solid lines are calculated using center-of-mass distributions similar to that of Gu *et al.* (solid lines in Figure 4.8); dotted lines are calculated same T(θ) and optimized P(E) from this work (dotted line in Figure 4.8)

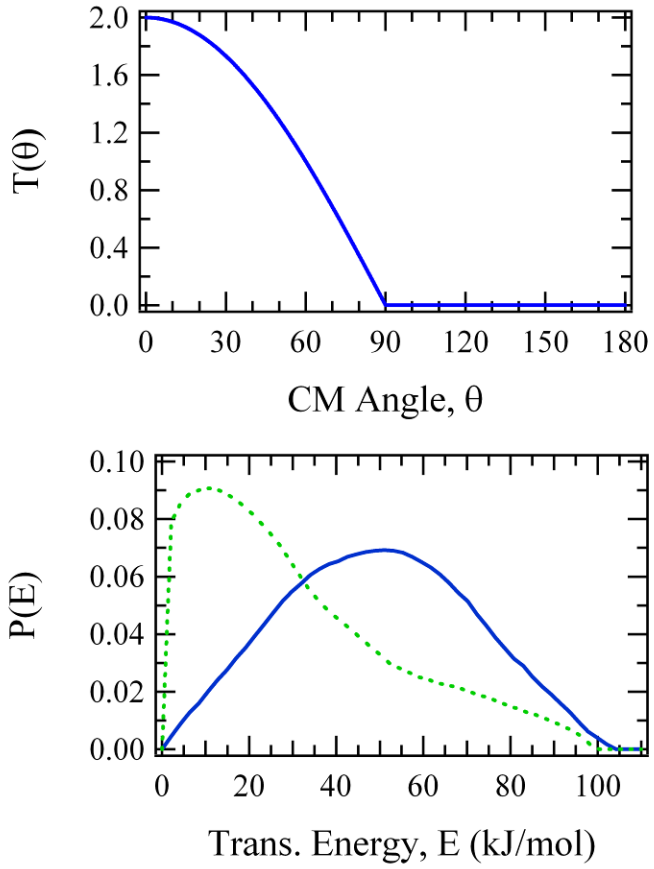

Figure 4.8: Solid Lines: T(Θ) and P(E) similar to that in Gu, X.; Zhang, F.; Kaiser, R.I. Crossed beam reaction of the phenyl radical, (C_6H_5, X(2)A ') with molecular oxygen (O_2, ($X^3\Sigma g$)): Observation of the phenoxy radical, (C_6H_5O, X_2A'). *Chem. Phys. Lett.* **2007,** 448, 7-10. Dotted Line: Optimized P(E) from this work

While both studies were carried out using the method of crossed beams employing pulsed sources for each beam, there are considerable experimental differences. Most notably, the C_6H_5 reactants were produced in our study by photodissociation of C_6H_5Cl in a room temperature nozzle, whereas in their work the C_6H_5 was produced by flash pyrolysis of C_6H_5NO at 1350 K.[20,33] In addition, our experiment was carried out at a lower mean collision energy.

Could the sharply differing dynamics reported in the only two existing crossed beam studies of $C_6H_5 + O_2$ be attributable to the different experimental conditions? Beams of polyatomic free

radicals have been produced in a variety of different ways including chemical reaction[34], electrical discharge[35], pyrolysis[36], and photolysis.[37] To date, there has been relatively little attention paid to how preparation of radicals can affect their reaction dynamics. Rice-Ramsperger-Kassel-Marcus (RRKM) calculations,[19] performed with a standard program,[38] can provide some insight into how the different experimental conditions might affect the measurements.

In pyrolysis sources, precursors are passed through a hot (up to 2000K) SiC tube causing decomposition into the corresponding radicals and byproducts. Using a short residence time (typically less than 10 μs), secondary reactions may be minimized.[36] While this approach can produce rather intense radical beams, the level of vibrational excitation can be large since vibrational energy is not as effectively cooled as rotations upon supersonic expansion.[39] Here we assume the vibrational temperature of the phenyl radicals employed in Ref. 20 is equal to the nozzle temperature, reported to be T = 1350 K.[33] Assuming a statistical vibrational distribution and approximating the vibrational modes as independent harmonic oscillators with the vibrational frequencies of C_6H_5[40], we calculate the average energy in each vibrational mode utilizing the vibrational partition function. The average total vibrational energy at 1350 K is the sum of the individual average energies, yielding 148 kJ/mol for C_6H_5 produced by pyrolysis of C_6H_5NO.

In our photolytic source, a laser is used to photodissociate C_6H_5Cl and the internal energy distributions of the radicals are governed by the photodissociation dynamics. Chlorobenzene photodissociation at 193nm has been well characterized by Sveum et al. using VUV photoionization detection of the products employing a synchrotron light source.[24] It is known that three distinct channels exist. By integrating the areas of the published P(E) distributions, the

branching ratio for the three channels was 55:42:3. Using the mean translational energy release for each channel, the average excess energy for the C_6H_5 + Cl products is ≈130 kJ/mol. Since the spin orbit splitting in Cl atoms is only 10.6 kJ/mol, most of the excess available energy is C_6H_5 vibrational energy. Assuming no vibrational cooling during the expansion and ignoring the energy deposited into spin-orbit excited Cl, the C_6H_5 radicals produced by photolysis in our experiment have, on average, about 88% as much vibrational energy as those produced by pyrolysis in the work of Gu et al.[20,21]

The mean collision energy employed in our study (64 kJ/mol) is smaller than that in the previous study (107 kJ/mol). This factor will also produce a greater level of excitation in any C_6H_5OO complexes formed in the reaction in the work of Gu, leading to shorter lifetimes in their experiment. Using the mean C_6H_5 vibrational energies, mean collision energies, and $D_o(C_6H_5\text{-}O_2)$ = 194 kJ/mol, the mean total vibrational energy, E of the C_6H_5OO complexes is 388 kJ/mol in our experiment and 449 kJ/mol in the work of Gu et al. The minimum energy for reaction, E_o is calculated to be $D_o(C_6H_5O\text{-}O)$ = 152 kJ/mol.[6]

Assuming RRKM theory is applicable to this reaction involving the polyatomic intermediate C_6H_5OO having 13 atoms and 33 vibrational degrees of freedom, our calculations should provide at least an order of magnitude estimate of decay rates. Using the vibrational frequencies and moments of inertia from Ref. 6, together with the values of E and E_o given above, we calculated RRKM rate constants, k_{uni}, for unimolecular decomposition of C_6H_5OO to C_6H_5O + O. The mean lifetimes τ (= $1/k_{uni}$) were calculated to be $\tau \approx 260$ ps for E = 388 kJ/mol, and $\tau \approx 70$ ps for E = 449 kJ/mol. These RRKM lifetimes correspond to many C_6H_5OO rotational periods, consistent with a forward-backward symmetric angular distribution.

97 kJ/mol C_6H_5 + O_2

A photolytic phenyl radical beam intersected the ~3% O_2 in H_2 beam at a 90° crossing angle leading to a collision energy of 97 ± 8 kJ/mol. The TOF distributions for the phenoxy (C_6H_5O) radical + ground-state atomic oxygen (O) channel, detected by monitoring signal at m/e = 93 ($C_6H_5O^+$) are shown in Figure 4.9. At 5 degrees, a small amount of background signal from impurities in the beam existed at early times and was subtracted from the displayed spectrum by recording the TOF spectra without the O_2 beam. The laboratory angular distribution shown as the solid dots in Figure 4.10 was generated by integrating the TOF spectrum at each laboratory angle, shown in Figure 4.9. The solid lines in Figures 4.9 and 4.10 are the optimized calculated fits to the experimental data using the P(E) and T(θ) shown as the solid lines in Figure 4.11. The dotted lines in Fig. 4.10 are the calculated fits using the angular distribution shown as a dotted line in Fig. 4.11, corresponding to osculating complexes with $I(0^o)/I(180^o) = 2$.

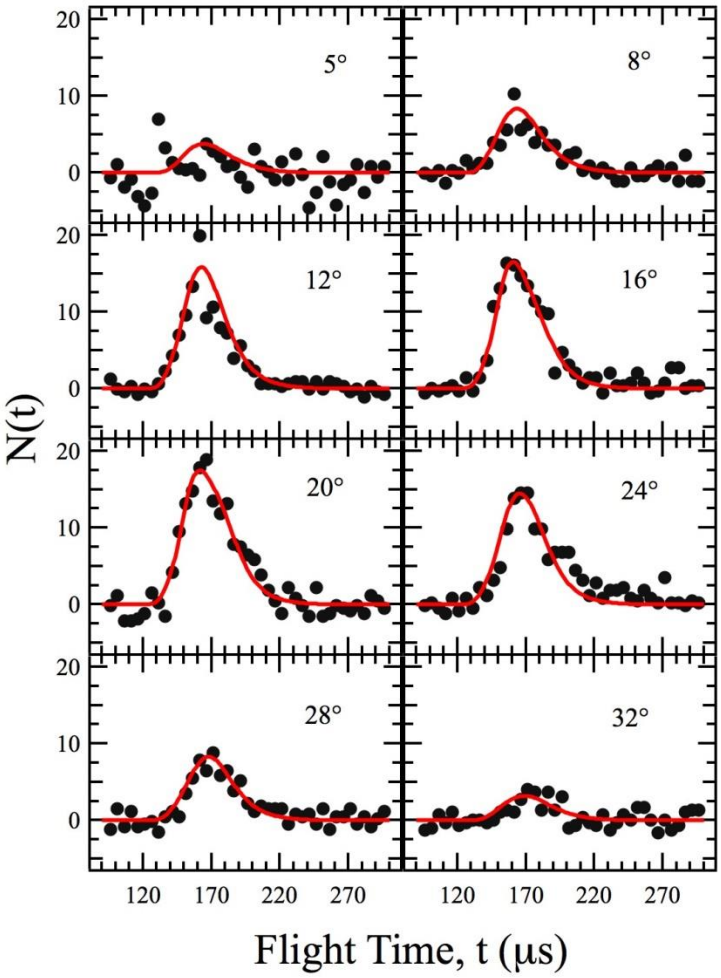

Figure 4.9: Measured TOF spectra for various laboratory angles for $C_6H_5O^+$ (m/e = 93) products. Solid dots represent experimental data points; solid lines are calculated using the optimal center-of-mass distributions shown in Figure 4.11.

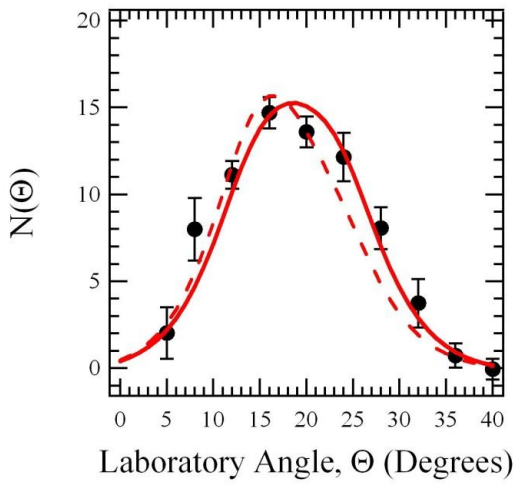

Figure 4.10: Laboratory angular distribution for $C_6H_5O^+$ (m/e = 93) products. Solid dots correspond to experimental data points with 1σ error bars. Solid line is calculated using the optimal center-of-mass distributions shown in Figure 4.11. Dotted line is calculated assuming an osculating complex distribution as shown in Figure 4.11.

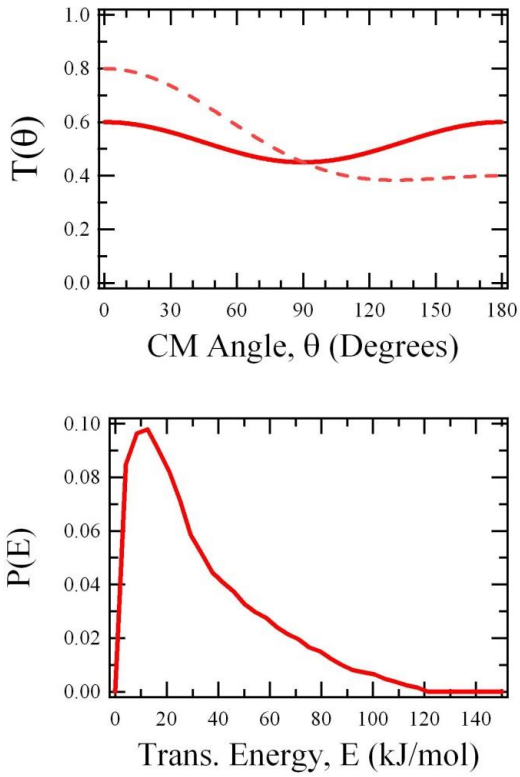

Figure 4.11: Solid lines are the optimized center-of-mass distributions. Dotted line is the osculating complex fit that represents the error limits of the center-of-mass angular distribution.

The P(E) peaks near zero kinetic energy release (~10 kJ/mol), implying a rather loose exit transition state to form C_6H_5O + O, consistent with simple O-O bond fission. The optimized center-of-mass angular distribution corresponds to a forward-backward symmetric T(θ). The osculating complex CM angular distribution (dotted line in figure 4.10 and 4.12) does not simulate the experimental data as well as when a forward-backward symmetric distribution is used.

The optimized fit to the data is forward-backward symmetric, with I(0°)/I(180°) = 1, corresponding to the existence of collision complexes with lifetimes much longer than their picosecond rotational periods. The absolute limit to the range of fits to our data, shown as dotted lines in Figures 4.10 and 4.11, leads to a maximum asymmetry in the angular distribution, corresponding to I(0°)/I(180°) = 2. This upper limit to the asymmetry corresponds to an absolute minimum lifetime for the C_6H_5OO intermediates of approximately one rotational period (~1 ps). The range of T(θ) fits we infer at a collision energy of 97 kJ/mol is the same as the range of fits previously inferred at a collision energy of 64 kJ/mol.[21] This consistency between the two collision energies suggests that even though the lifetimes of the intermediates are likely decreasing, as would be predicted by RRKM theory, the mean lifetimes of intermediates are not likely becoming as short as a few rotational periods. If our 64 kJ/mol result had been an osculating complex, i.e. lifetimes comparable to a rotational period, then we would expect a detectable increase of forward scattering to exist, from the expected decrease in C_6H_5OO lifetimes, when increasing the collision energy from 64 kJ/mol to 97 kJ/mol. Our range of acceptable fits, implying lifetimes much longer than a rotational period at 97 kJ/mol is consistent with RRKM calculations and sharply contrast the original results and subsequent reinterpretation reported by the Kaiser group at a collision energy of 107 kJ/mol.

In the 107 kJ/mol data originally reported by the Kaiser group in 2007, the derived center-of-mass angular distribution was sharply forward peaked, i.e. $I(0°)/I(180°) = \infty$, implying a direct reaction to form $C_6H_5O + O$, with the stated lifetime, $\tau \leq 10$ fs.[20] A subsequent reinterpretation of the same data, has apparently led to $I(0°)/I(180°) = 9 \pm 4$. This revised mean value corresponds to reaction intermediates whose maximum lifetimes are about one third of a rotational period, i.e., $\tau \sim 0.3$ ps. The revised lower limit to $I(0°)/I(180°) = 5$ would correspond to an absolute upper limit of $\tau \leq 0.5$ ps.

Earlier, we calculated RRKM lifetimes for differing amounts of total energy available to C_6H_5OO intermediates.[21] The mean RRKM lifetimes, assuming the only reaction channel is the formation of C_6H_5O and O, for C_6H_5OO intermediates at 107 kJ/mol collision energy is 70 ps. This is still more than two orders of magnitude longer than the absolute upper limit of 0.5 ps inferred in the most recent reinterpretation by Kaiser's group.[22]

The primary experimental differences between our results and the original data published by the Kaiser group are the detection scheme and the phenyl radical source. The Kaiser group uses an 80 eV electron impact ionizer for both the 38 and 107 kJ/mol experiments; whereas we use 9.9 eV "soft" single photon ionization in both of our experiments. Fragmentation of parent C_6H_5O is expected to occur to a much larger extent when using an 80 eV electron impact ionizer than with 9.9 eV single-photon ionization detection. One could imagine that C_6H_5O radicals with a large amount of internal energy could be more likely to fragment when using the electron impact ionizer, consequently the low translational energy release (high internal energy) component of the P(E) would be underrepresented in the electron impact experiments. C_6H_5O radicals that have long lifetimes are more likely to have substantial energy randomization leading to a higher degree of internal excitation. It should be noted that in the 38 kJ/mol experiment the

Kaiser group finds the P(E) peaking at low translational energy release, *i.e.* high internal excitation, so the transition to large amounts of fragmentation must be taking place when the total energy available to products goes from ~210 kJ/mol, in the 38 kJ/mol photolysis experiment, to ~300 kJ/mol in the 107 kJ/mol pyrolysis experiment (using the internal energy estimates for phenyl radicals from Ref. 21). The amount of fragmentation would have to substantially increase over this range in order to account for the different experimental observations.

With regards to the phenyl radical source, our results and the recent low energy (~38 kJ/mol) results of Parker *et al.*[22] were obtained with a photolytic phenyl radical source, whereas those from ref. 20 are generated with a pyrolytic source of phenyl radicals. We have already shown that the total internal energy of phenyl radicals beams produced by pyrolysis and photolysis are comparable assuming similar amounts of vibrational cooling in the different phenyl radical sources.[21] We now turn to a careful analysis of the phenyl radical beams produced by photolysis and pyrolysis.

Phenyl Radical Beam Characterization

A thorough characterization of the radical beams, with careful attention to the possible existence of any impurities, is crucial. The ideal radical source produces exclusively the radical of interest with no interfering species.

The mass spectra of the phenyl radical beams, recorded using the two-chamber fixed source apparatus, produced either by photodissociation of chlorobenzene or by pyrolysis of nitrosobenzene are shown in Figure 4.12a and 4.12b, respectively. The snapshots of the beams shown are those which produce the largest signal at the parent mass of the phenyl radical ion,

m/e = 77. However, the composition did not change significantly for conditions where signal levels were not optimized. Under optimized conditions, the phenyl radical peak intensity produced in the photolysis source is about a factor of five higher than that produced with the pyrolysis source.

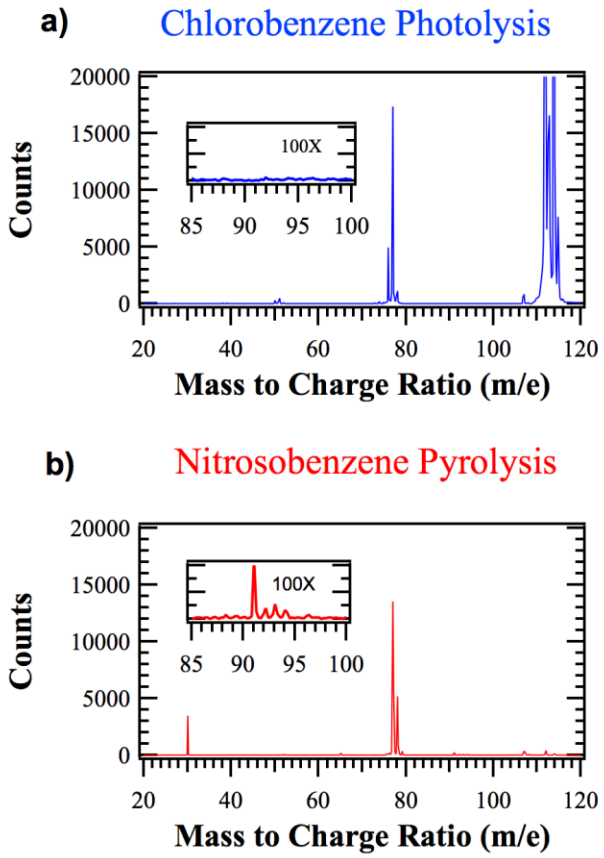

Figure 4.12: **a)** Mass spectrum of phenyl radical source using photolysis of chlorobenzene. Inset shows a 100x zoomed in portion of the mass spectrum around $C_6H_5O^+$, m/e = 93. **b)** Mass spectrum of phenyl radical source using pyrolysis of nitrosobenzene. Inset shows a 100x zoomed in portion of the mass spectrum around $C_6H_5O^+$, m/e = 93.

For both beams, phenyl radical, m/e = 77, is the major product. In the pyrolysis source, most of the C_6H_5NO precursor is consumed, so the parent m/e = 107 peak is very weak. In the photolysis source, a substantial fraction of undissociated C_6H_5Cl remains, as evidenced by the signal observed at m/e = 112 and m/e = 114. Note that the NO is readily ionized at 9.9 eV whereas Cl is not.

A crucial difference in the two radical sources is the nature of the impurities. In the photolytic beam (Fig. 4.12a), the major impurities result from secondary photodissociation of phenyl radicals, producing C_4H_3 (m/e = 51) + C_2H_2 and C_6H_4 (m/e = 76) + H. Our observations are consistent with the study by Negru and coworkers, who observed these channels in the photodissociation of phenyl radicals at 193 nm.[41] We found that the most intense phenyl radical beams are generated at modest laser fluences, thereby minimizing secondary photodissociation of the phenyl radical.

In the pyrolysis source (Fig. 4.12b), the main source of impurities comes from chemical reactions that take place inside the hot pyrolysis tube. The elevated temperatures (1200 - 1500 K) and chemically long residence times (~10 μs) in the tube have been described as a 'high-temperature 'chemical reactor'".[42] Very importantly, pyrolysis of nitrosobenzene leads to a significant yield of m/e = 93, corresponding to phenoxy radical (C_6H_5O) impurity in the beam. Not surprisingly, the C_6H_5O impurity level is very small for the photolytic source, since no oxygen is present in seeded chlorobenzene beams. The level of C_6H_5O impurity produced in the pyrolysis source depends on the pyrolysis source temperature and the concentration of nitrosobenzene in the beam. Impurity levels were found to decrease relative to phenyl radicals with increasing pyrolysis source temperature (varied from 1200-1500 K). Impurity levels were also found to increase with increasing nitrosobenzene concentration when the nitrosobenzene

bath temperature was increased from 4 °C to 21 °C. Over the range of experimental parameters studied, the phenoxy radical impurity (relative to phenyl radical) ranged from 0.4 % to 1.2 %. For the photolytic source of phenyl radicals, the signal at m/e = 93, corresponding to C_6H_5O impurity, is within the baseline. From the signal levels measured in the TOF mass spectra, an absolute upper limit to this ratio is 0.1 %. We also monitored the signals at m/e = 93 and m/e = 77 at small laboratory angles using the photoionization detector of our rotatable source crossed molecular beam apparatus, which has a much higher detection sensitivity than the TOF mass spectrometer. Using the photolytic phenyl radical source, we the measured ratio of m/e = 93 to m/e = 77 in the beam was found to be ~0.03 %. This is at least an order of magnitude smaller than the m/e = 93 impurity level found using the pyrolytic phenyl radical source.

Additional impurities are observed in both the photolytic and pyrolytic beams. However, the impurities are quite different for each case, because of the different precursors and beam conditions. The difference is best illustrated by examining the trio of peaks at m/e = 76, 77 and 78, corresponding to $C_6H_4^+$, $C_6H_5^+$ and $C_6H_6^+$. In the photolysis source we saw mainly $C_6H_5^+$ with a significant amount of $C_6H_4^+$ coming from the secondary photochemistry and only a small amount of $C_6H_6^+$. Conversely, in the pryolysis source the main peak still corresponds to $C_6H_5^+$, but a significant amount of signal exists for $C_6H_6^+$ resulting from phenyl radicals abstracting hydrogen atoms from other hydrocarbons, most likely from the nitrosobenzene precursor, with only a small amount of signal at m/e = 76.

One must carefully consider the implications of impurities to the interpretation of experimental data. We have looked for products from reaction of benzyne (C_6H_4), efficiently produced by 193 nm photolysis of fluorobenzene[43], with O_2. We have found no evidence for any reactions under our experimental conditions. In all studies on the reaction of phenyl radicals

with molecular oxygen, the C_6H_5O + O channel has been investigated by detecting the phenoxy radical ion, $C_6H_5O^+$. Therefore, the amount of impurity at this mass, m/e = 93, is of critical importance.

The smaller yield of phenyl radicals and substantial C_6H_5O impurity in the pyrolysis source is very important to the outcome of crossed beams studies of reactions where C_6H_5O is detected. Specifically, the C_6H_5O impurity in the phenyl beam will undergo elastic and inelastic collisions with the O_2 molecules and with its He carrier gas. This contribution must be considered explicitly if beams containing significant levels of C_6H_5O impurity are employed. The signals from non-reactive elastic and inelastic scattering typically increase sharply as the beam centerline axis is approached. In the 107 kJ/mol study by the Kaiser group, no subtraction of background signal was carried out, and the result contained a "lack of TOF data beyond the center-of-mass angle in Gu et al.'s study closer to the primary beam."[22] While we cannot be certain of the level of C_6H_5O impurity in the pyrolysis source used by the Kaiser group; the lack of background subtraction in the pyrolytic phenyl radical source experiment coupled with an increased level of C_6H_5O impurity could account for the discrepancy between the different experimental results. We see no large increase in the forward-scattering contribution at higher collision energies, whereas the Kaiser group results imply a sharp increase in the forward-scattering contribution as the collision energy is increased.[20,21,22]

Search for Channels Other than C_6H_5O + O

As a consequence of the long lifetimes of the C_6H_5OO intermediates other reaction channels may be competitive. The previous calculations indicate that isomerization of the C_6H_5OO

radical to the 2-oxepinyloxy radical, may lead to three different channels, i.e., $C_6H_4O_2$ + H, C_5H_5 + CO_2 and C_5H_5O + CO.

The ionization energy for $C_6H_4O_2$ (from the H atom elimination channel) is ~10 eV. Given that our light source produces 9.9 eV photons, we were unable to detect this reaction pathway in the present experiments. While detection of C_5H_5 should be possible using 9.9 eV photons (IP = 8.4 eV), C_6H_5O is known to fragment upon photoionization producing $C_5H_5^+$.[44] Consequently, substantial background signals were observed at m/e = 65, and so we were not able to see any evidence for this channel in our experiment.

Because $C_5H_5O^+$ is aromatic, and hence very stable, the ionization energy of the pyranyl radical (C_5H_5O) is expected to be very low, *i.e.*, likely below 7.9 eV.[45] Therefore, we attempted to observe this channel using a 157 nm F_2 excimer laser (7.9 eV) as an ionization source and, in separate experiments, using 9.9 eV photons, in experiments at a mean collision energy of 71 kJ/mol. However, no reaction products were detected using either 7.9 or 9.9 eV photons. On the basis of these experiments, we believe that the C_5H_5O + CO is at most a minor channel (< 10%) under our experimental conditions. Unfortunately, we are not able to draw any conclusions about the possible existence of the other channels based on our measurements.

Conclusions

In the reaction of phenyl radicals with molecular oxygen, the lifetimes of C_6H_5OO intermediates are at least 1 ps, and probably much longer, even at a collision energy of 97 kJ/mol. The range of acceptable CM angular distributions for the 97 kJ/mol and 64 kJ/mol results are identical[21], *i.e.* no sharp increase in forward scattering is detected as the collision energy is increased to 97 kJ/mol. Our result is quite different from the original ($\tau \leq 10$ fs) and

revised ($\tau \leq 0.5$ ps) lifetimes derived by Kaiser *et al.*.[20,22] A possible source of this discrepancy could be C_6H_5O impurities in pyrolytic phenyl radical beams employing nitrosobenzene. Even for collision energies up to 97 kJ/mol RRKM lifetimes for C_6H_5OO intermediates are consistent with the experimental results.

REFERENCES

1. H. Richter and J.B. Howard, *Progress in Energy and Combustion Science*, **26**, 565 (2000).

2. J.A. Miller, M.J. Pilling, and J. Troe, *Proceeding of the Combustion Institute*, **30**, 43 (2005).

3. J. Appel, H. Bockhorn and M. Frenklach, *Combustion and Flame*, **121**, 122 (2000).

4. B. Carpenter, *J. Am. Chem. Soc.*, **115**, 9806 (1993).

5. C. Barckholtz, M.J. Fadden and C.M. Hadad, *J. Phys. Chem. A*, **103**, 8108 (1999).

6. I.V. Tokmakov, G.S. Kim, V.V. Kislov, A.M. Mebel and M.C. Lin, *J. Phys. Chem. A*, **109**, 6114 (2005).

7. G. da Silva and J.W. Bozzelli, *J. Phys. Chem. A*, **112**, 3566 (2008).

8. P.M. Sommeling, P. Mulder, R. Louw, D.V. Avila, J. Lusztyk and K.U. Ingold, *J. Phys. Chem.*, **97**, 8361 (1993).

9. P. Frank, J. Herzler, T.H. Just and C. Wahl,*Twenty-Fifth Symposium on Combustion.*, 833 (1994).

10. T. Yu and M.C. Lin, *J. Am. Chem. Soc.*, **116**, 9571 (1994).

11. J. Schaugg, R.S. Tranter, and H.H. Grotheer, in *Transport Phenomena in Combustion, Vol. 1*. S.H. Chan, ed. Taylor and Francis: Washington D.C. 1996. Pg. 130-141.

12. K. Tonokura, Y. Norikane, M. Koshi, Y. Nakano, S. Nakamichi, M. Goto, S. Hashimoto, M. Kawasaki, M.P. Sulbaek Anderson, M.D. Hurley and T.J. Wallington, *J. Phys. Chem. A*, **106**, 5908 (2002).

13. K. Liu, *J. Chem Phys.*, **125**, 132307 (2006).

14. P. Casavecchia, N. Balucani and G.G. Volpi, *Ann. Rev. Phys. Chem.*, **50**, 347 (1999).

15. B.R. Strazisar, C. Lin and H.F. Davis, *Science*, **290**, 958 (2000).

16. J.D. Sierra, L. Bonnet and M. Gonzalez, *J. Phys. Chem. A*, **115**, 7413 (2011).

17. P. Casavecchia, F. Leonori, N. Balucani, R. Petrucci, G. Capozza and E. Segoloni, *Phys. Chem. Chem. Phys.*, **11**, 46 (2009).

18. N. Balucani, G. Capozza, F. Leonori, E. Segoloni and P. Casavecchia, *Int. Rev. Phys. Chem.*, **25**, 109 (2006).

19. T. Baer and W.L. Hase, *Unimolecular Reaction Dynamics*; Oxford University Press: New York, 1996.

20. **X.** Gu, F. Zhang and R.I. Kaiser, *Chem. Phys. Lett.*, **448**, 7 (2007).

21. D.R. Albert and H.F. Davis, *J. Phys. Chem. Lett.*, **1**, 1107 (2010).

22. D.S.N. Parker, F. Zhang and R.I. Kaiser, *J. Phys. Chem. A*, **115**, 11515 (2011).

23. D.L. Proctor, D.R. Albert and H.F. Davis, *Rev. Sci. Instrum.*, **81**, 023106 (2010).

24. N.E. Sveum, S.J. Goncher and D.M. Neumark, *Phys Chem. Chem. Phys.*, **8**, 592 (2006).

25. W.C. Wiley and I.H. McLaren, *Rev. Sci. Instrum.*, **26**, 1150 (1955).

26. R. Hilbig and R. Wallenstein, *IEEE J. Quant. Electron.*, **QE-19**, 1759 (1983).

27. P.A. Willis, H.U. Stauffer, R.Z. Hinrichs and H.F. Davis, *Rev. Sci. Instrum.*, **70**, 2606 (1999).

28. P.A. Willis, H.U. Stauffer, R.Z. Hinrichs and H.F. Davis, *J. Phys. Chem. A.*, ***103***, 3706 (1999).

29. R.D. Levine, *Molecular Reaction Dynamics*; Cambridge University Press: Cambridge, UK, 2005.

30. A.D. Estillore, L.M. Visger and A.G. Suits, *J. Chem. Phys.*, **133**, 074306 (2010).

31. G.A. Fisk, J.D. McDonald and D.R. Herschbach, *Faraday Discuss. Chem. Soc.*, **44**, 228 (1967).

32. M. Alagia, N. Balucani, P. Casavecchia, D. Stranges and G.G. Volpi, *J. Chem. Phys.*, **98**, 8341 (1993).

33. X. Gu and R.I. Kaiser, *Acc. Chem. Res.*, **42**, 290 (2009).

34. R.I. Kaiser, J.W. Ting, L.S. Huang, N. Balucani, O. Asvany, Y.T. Lee, H. Chan, D. Stranges and D. Gee, *Rev. Sci. Instrum.*, **70**, 4185 (1999).

35. F. Dong, M. Roberts and D.J. Nesbitt, *J. Chem. Phys.*, *128*, 044305 (2008).

36. D.W. Kohn, H. Clauberg and P. Chen, *Rev. Sci. Instrum.*, **63**, 4003 (1992).

37. H.F. Davis, J. Shu, D.S. Peterka and M. Ahmed, *J. Chem. Phys.*, **121**, 6254 (2004).

38. L. Zhu and W.L. Hase, Program 644, Quantum Chemistry Program Exchange, Indiana University

39. D.R. Miller, in *Atomic and Molecular Beam Methods*, Vol. 1, G. Scoles, ed. Oxford University Press, New York, 1988. Pg 35.

40. A.V. Friderichsen, J.G. Radziszewski, M.R. Nimlos, P.R. Winter, D.C. Dayton, D.E. David and G.B. Ellison, *J. Am. Chem. Soc.***, 123**, 1977 (2001).

41. B. Negru, S.J. Goncher, A.L. Brunsvold, G.M.P. Just, D. Park and D.M. Neumark, *J. Chem. Phys.*, 133, 074302 (2010).

42. F.T. Zhang, R.I. Kaiser, V.V. Kislov, A.M. Mebel, A. Golan and M. Ahmed, *J. Phys. Chem. Lett.*, **2**, 1731 (2011).

43. S.H. Lee, C.Y. Wu, S.K. Yang and Y.P. Lee, *J. Chem. Phys.*, **125**, 144301 (2006).

44. C.M. Tseng, Y.T. Lee, M.F. Lin, C.K. Ni, S.Y. Liu, Y.P. Lee, Z.F. Xu and M.C. Lin, *J. Phys. Chem. A.*, **111**, 9463 (2007).

45. B. Carpenter, personal communication.

CHAPTER 5: Crossed Molecular Beam Studies of Phenyl Radical Reactions with Propene and 2-Butene

Introduction

The reactions of phenyl radicals (C_6H_5) in combustion environments has long been established as a benchmark for understanding the role of cyclic aromatic species, particularly in the formation of soot.[1,2] Soot formation is initiated by the formation of polycyclic aromatic hydrocarbons (PAH), which can then aggregate to form the nano/micro sized particles that cause a wide variety of environmental and health issues.[3,4] The reaction of phenyl radicals with unsaturated hydrocarbons is thought to be one of the key initiation processes in the synthesis of PAH. The electron deficient phenyl radical site can add to the π-electronic system of an unsaturated hydrocarbon, forming a branched aromatic species which can then continue to grow via the HACA (hydrogen-atom abstraction, acetylene addition) mechanism or other hydrocarbon addition mechanisms.[5,6] Considerable work has been carried out by Lin and coworkers aimed at understanding the potential energy surfaces for this class of reactions.[7,8,9] In order to accurately test the prediction of product branching ratios using calculated potential energy surfaces, the identification and quantification of primary product channels as a function of available energy is necessary. Crossed molecular beam (CMB) scattering experiments serve as a valuable technique for elucidating product branching ratios and reaction mechanisms under single collision conditions.[10,11,12]

In the reaction of C_2 hydrocarbons with phenyl radicals, the only predicted primary products involve H-atom abstraction from the C_2 hydrocarbon, $C_6H_5 + C_2H_x \rightarrow C_6H_6 + C_2H_{x-1}$, or addition to an unsaturated hydrocarbon followed by H-atom elimination, $C_6H_5 + C_2H_x \rightarrow C_6H_5C_2H_{x-1} + H$.[7,8] When phenyl radicals react with larger unsaturated hydrocarbons, the same

H-atom abstraction and elimination pathways exist in addition to other elimination products (CH_3, C_2H_5, etc.) that form larger aromatic species.[9]

The reaction of phenyl radicals with propene was studied as early as 1972, when Hefter and coworkers examined the addition products by electron spin resonance at 183 K in liquid propene. They found evidence of three pathways: addition to the 1-carbon, addition to the 2-carbon, and an H-atom abstraction channel forming benzene plus allyl radicals.[13]

Park et al. studied the consumption of phenyl radicals in the presence of propene using cavity ring-down spectroscopy, finding the rate constant at low temperatures (296K - 496K) to be ~10^{12} cm^3 mol^{-1} s^{-1}.[9] In addition they calculated stationary points along the reaction coordinates for many of the key reaction pathways. On the basis of calculated potential energy barriers, Park et al. predicted that addition to the 1-carbon atom, forming the 1-phenyl reaction intermediate, to be the dominant addition channel over their temperature range. Addition to the 2-carbon atom, forming the 2-phenyl reaction intermediate, was predicted to involve a barrier 5 - 10 kJ mol^{-1} higher than addition to the 1-carbon atom.[9]

The first crossed molecular beam experiments were conducted at collision energies between 130 and 194 kJ mol^{-1}.[14,15] Under these conditions, only the H-atom elimination channel was observed, with an upper limit of 10% placed on the possible methyl elimination channel producing styrene (C_8H_8). From experiments employing deuterium-substituted propene, it was concluded that ~85% of the H-atoms were emitted from the vinyl moiety with the other ~15% coming from the methyl group.[14] This result was consistent with expectations that vinylic H atoms are more weakly-bound than those in the methyl group.

In a reinvestigation of the reaction of phenyl radicals with propene at a much lower collision energy (45 kJ/mol), methyl-elimination forming C_8H_8 was observed along with the previously-identified H-atom elimination pathways.[16] The product branching ratio between the methyl and H-atom elimination was found to be ~2:1, in apparent agreement with RRKM calculations that accompanied the experimental work.[16] The RRKM calculations predicted that methyl radical elimination forming styrene (C_8H_8) should be dominant at low collision energies, with H-atom elimination forming C_9H_{10} becoming dominant at collision energies above 100 kJ/mol. However, in contrast to the earlier theoretical calculations where 1-phenyl propene was predicted to be dominant, 3-phenyl propene was predicted to be the dominant C_9H_{10} isomer.[16] While this apparent disagreement with the earlier theoretical study was not addressed, according to the calculations, preferential fission of the more strongly-bound H atoms from the methyl group was attributable to the potential energy barrier being about 1 kJ/mol smaller than for vinylic C-H fission.[14,16]

In more recent work carried out at Berkeley's Advanced Light Source, the reactions of phenyl radicals with propene was studied using a pyrolysis molecular beam reactor.[17] Nitrosobenzene, which undergoes pyrolysis to form phenyl radicals and nitrogen monoxide, was coexpanded with propene carrier gas in a high temperature pyrolysis nozzle source where the phenyl radicals can subsequently react with propene. Products were probed using "soft" VUV single photon ionization using a synchrotron. The authors were able to identify the methyl elimination channel forming C_8H_8, as well as H-atom elimination forming, C_9H_{10}. At the estimated temperature of the pyrolysis tube (1200-1500 K), formation of C_8H_8 was found to be dominant with a branching ratio of 6:1 for C_8H_8:C_9H_{10}. The contribution from C_8H_8 + CH_3

relative to C_9H_{10} + H inferred from the photoionization study is much larger than inferred from the crossed beam study[16] or the RRKM calculations.[18]

Product photoionization efficiency curves can, under favorable conditions, be used to distinguish between chemical isomers.[19,20] In the reaction of phenyl + propene, the C_8H_8 product was identified as the lowest-energy styrene isomer. Studies of the photoionization efficiencies for the C_9H_{10} product led to the conclusion that the dominant H atom elimination channel produces primarily the 3-phenyl propene isomer, with a very small yield of the cis- and trans- 1-phenyl propene and no evidence for production of the cyclic indane isomer. While these conclusions were in apparent agreement with the newer calculations predicting dominant formation of 3-phenyl propene from H atom elimination, they appear to be inconsistent with the earlier crossed beam conclusion that 1-phenyl propene was dominant.

In the present work, we report studies of reactions of phenyl radicals with propene at collision energies of 84 and 108 kJ/mol. To gain further insight into the C_6H_5 + C_3H_6 reaction, we also have performed CMB studies of the reaction of phenyl radical with trans-2-butene (C_4H_8).

C_6H_5 + C_3H_6 Experiments

The TOF distributions for C_6H_5 + C_3H_6 at E_{coll} = 84 kJ/mol, monitoring the formation of C_9H_{10} + H and C_8H_8 + CH_3, are shown in figures 5.1 and 5.2 respectively. The H-atom elimination products were monitored at m/e = 118 ($C_9H_{10}^+$) and methyl elimination products were monitored at m/e = 104 ($C_8H_8^+$). The corresponding laboratory angular distributions are shown in figure 5.3. The best fit CM functions for both channels are shown in figure 5.4. The best fit T(Θ) is forward-backward symmetric for both product channels, showing evidence for

participation of collision complexes with lifetimes greater than their picosecond rotational timescales. The best fit P(E) for the methyl elimination product channel peaks at ~35 kJ/mol, implying an exit barrier for the formation of C_8H_8 + CH_3. The best fit P(E) for the H-atom elimination products also peaks near zero. However, due to the kinematics of detecting a heavy species recoiling from an H-atom, the uncertainty in the P(E) is much larger than that for the methyl elimination channel.

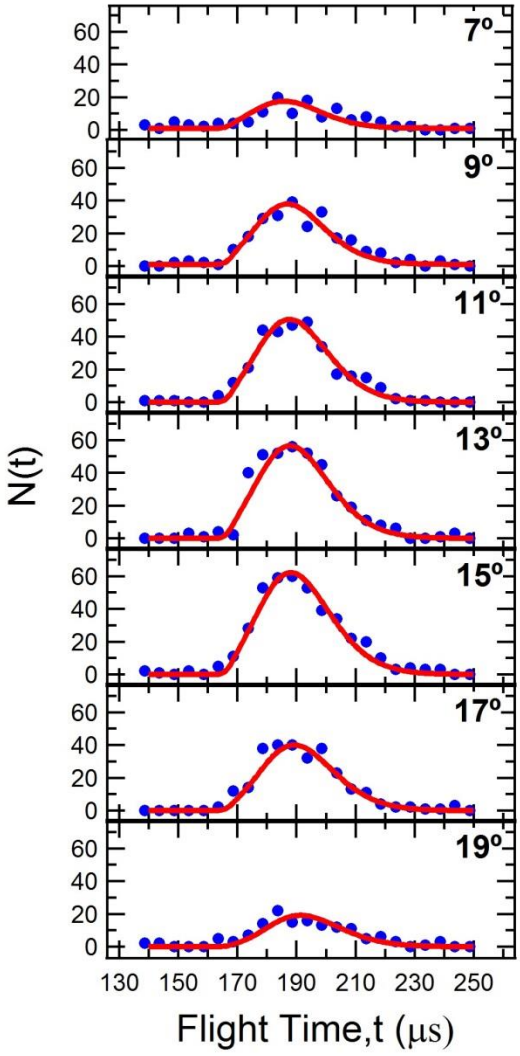

Figure 5.1: TOF spectra monitoring $C_9H_{10}^+$ (m/e =118) in the C_6H_5 + C_3H_6 → C_9H_{10} + H reaction, E_{coll} = 84 kJ/mol. Solid dots represent experimental data points; solid lines are calculated using the optimized CM distribution functions shown in Figure 5.4.

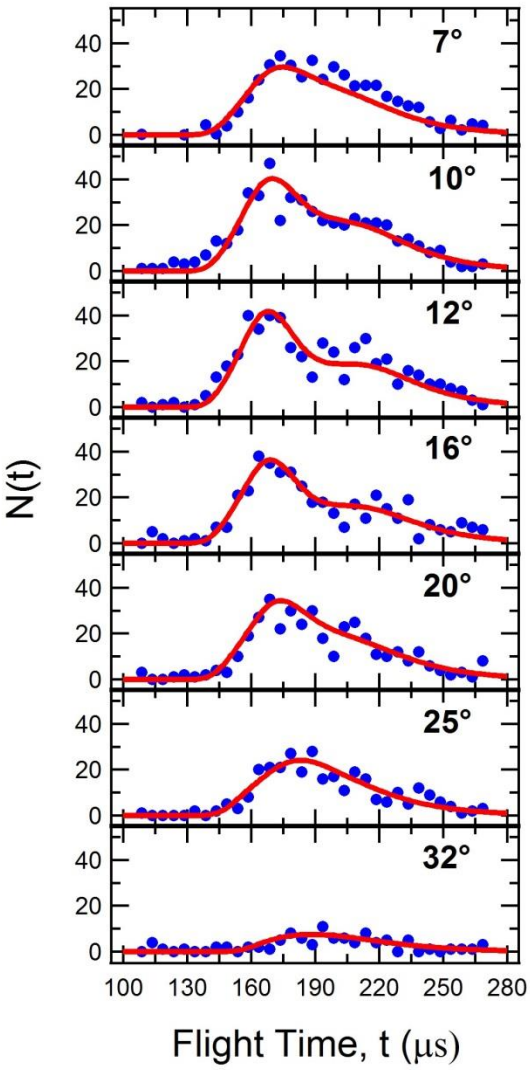

Figure 5.2: TOF spectra monitoring $C_8H_8^+$ (m/e =104) in the $C_6H_5 + C_3H_6 \rightarrow C_8H_8 + CH_3$ reaction, E_{coll} = 84 kJ/mol. Solid dots represent experimental data points; solid lines are calculated using the optimized CM distribution functions shown in Figure 5.4.

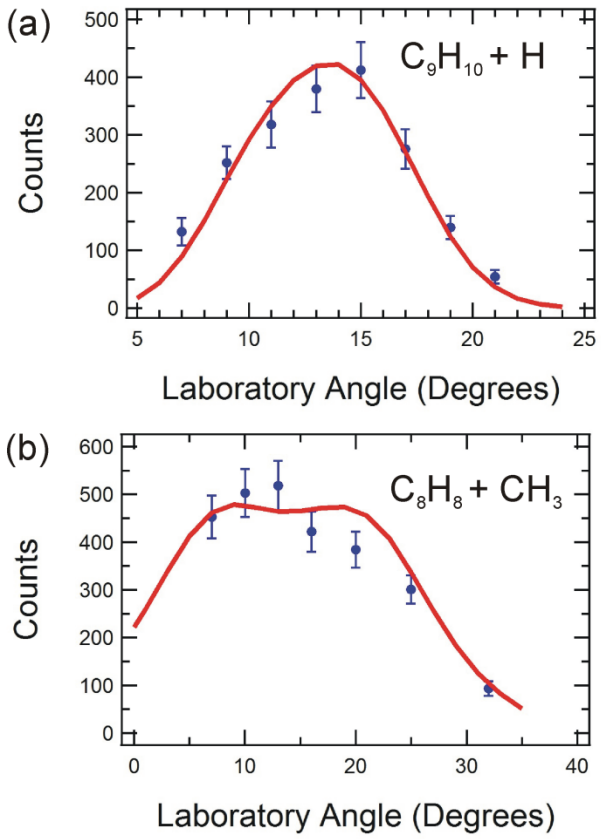

Figure 5.3: Laboratory angular distributions for the C_6H_5 + C_3H_6 reaction, E_{coll} = 84 kJ/mol. Solid dots represent experimental data points with 1σ error bars. Solid lines are calculated using the optimized CM distribution functions shown in Figure 5.4. (a) $C_9H_{10}^+$ (m/e = 118) from the C_6H_5 + C_3H_6 → C_9H_{10} + H reaction. (b) $C_8H_8^+$ (m/e = 104) from the C_6H_5 + C_3H_6 → C_8H_8 + CH_3 reaction.

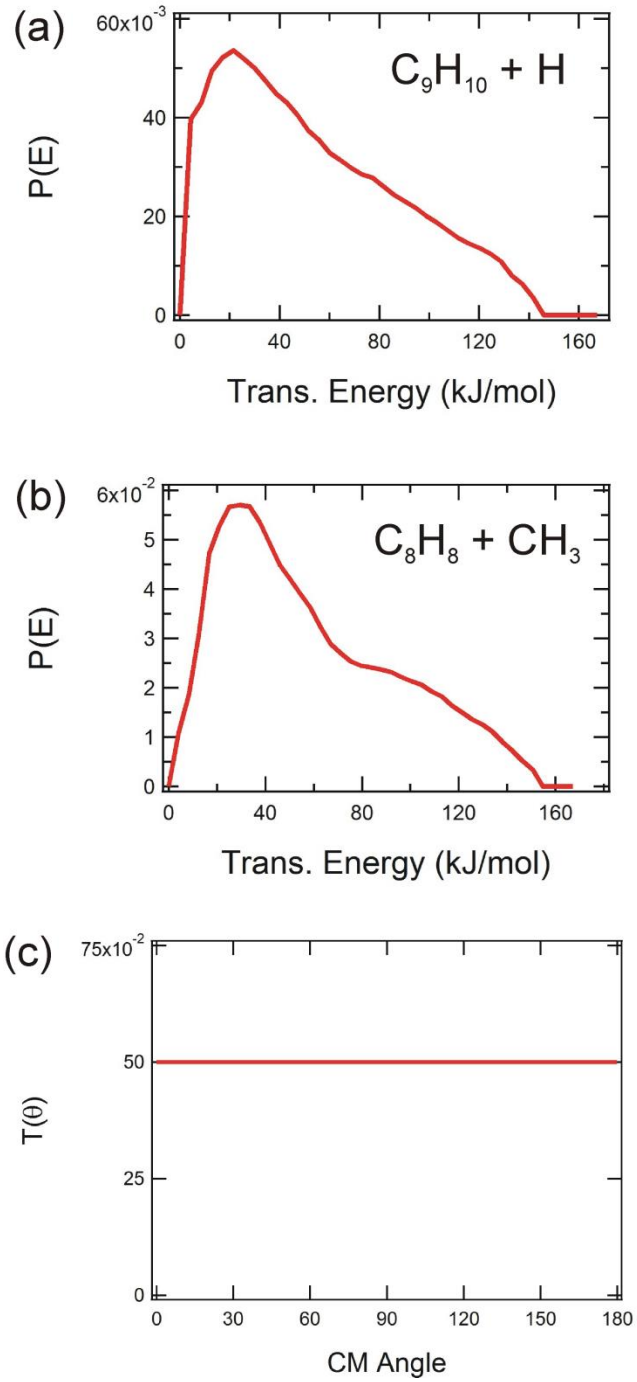

Figure 5.4: Optimized CM distributions for the C_6H_5 + C_3H_6 reaction, E_{coll} = 84 kJ/mol. (a) P(E) for the C_9H_{10} products; (b) P(E) for the C_8H_8 products; (c) T(Θ) used for both C_9H_{10} and C_8H_8 products.

The Newton diagrams for each product channel (Figure 5.5) illustrate the difference in the kinematics of the two product channels. The small Newton circle for H-atom elimination constrains the C_9H_{10} products to angles and velocities near that of the center of mass velocity vector. Consequently, the widths of the TOF and lab angular distributions are largely determined by the width of the center of mass velocity vector, especially in the case when the P(E) peaks near zero translational energy release. At a given angle, a larger fraction of the total H-atom elimination products are observed relative to those for methyl-elimination products (Figure 5.5). The product branching ratio at E_{coll} = 84 kJ/mol was found to be 10:1 for C_8H_8:C_9H_{10}.

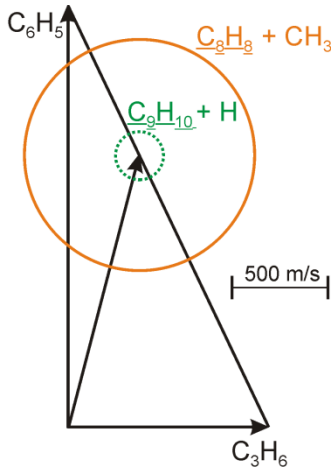

Figure 5.5: Newton diagram for the C_6H_5 + C_3H_6 reaction, E_{coll} = 84 kJ/mol. Dotted green circle corresponds to the maximum Newton circle for monitoring C_9H_{10} from C_6H_5 + C_3H_6 → C_9H_{10} + H. Solid orange circle corresponds to the maximum Newton circle for monitoring C_8H_8 from C_6H_5 + C_3H_6 → C_8H_8 + CH_3.

The determination of product branching ratios must take into account the relative detection sensitivities for both products. In order to quantify the detection sensitivity for C_8H_8 and C_9H_{10},we have monitored non-reactive scattering of molecular beams of styrene (Aldrich, C_8H_8) and alpha-methyl styrene (Aldrich, C_9H_{10}) using both a 100 eV electron impact ionization and 9.9 eV photoionization. By comparing the signal levels using both detection schemes, we found that the 9.9 eV photoionization cross section for both species are equal to within our experimental uncertainty. This is not surprising as similar molecules belonging to a particular class (alkane, alkene, monoaromatic species, etc.) often have comparable photoionization cross sections at comparable energies above their ionization thresholds.[21,22] We anticipate that the other possible C_9H_{10} isomers, all of which have ionization energies within 0.2 eV, have 9.9 eV photoionization cross sections similar to alpha-methyl styrene.[17,23]

The dependence of internal energy on photoionization cross section is relevant to the determination of product branching ratios.[24,25,26] The total available product energy is the a sum of the collision energy, internal energy of reactants and reaction exoergicity. This energy is distributed among internal degrees of freedom (vibration, rotation, etc.) of the product species and relative translational energy. In the data fitting procedure the translational energy distribution, P(E), is inferred; the total product internal energy distribution is found by subtracting the P(E) from the total energy available. In the $C_6H_5 + C_3H_6$ reaction studied here, the total internal energy distribution is not much different for the C_8H_8 and C_9H_{10} reaction channels, ranging from 0 to 300 kJ/mol. The C_8H_8 product has a P(E) that peaks further from zero than the C_9H_{10} product and will thus have a slightly lower internal energy contribution. The largest effect of internal energy on photoionization cross section is seen near the photoionization threshold.[24,25,26] One obvious case of internal energy affecting the photoionization cross section

occurs with the ionization of product molecules below their 0 K ionization potential.[24,25] In this case vibrationally excited neutrals now have sufficient energy to reach the ground state of the ion, where their vibrationless counterparts do not. Also, when just above threshold, Franck-Condon factors can significantly affect the ionization efficiency if the ion has different equilibrium bond lengths than the neutral.[26] Recent studies probing this behavior have found that when molecules are ionized using single photon ionization that is well above the ionization threshold (> 1 eV), the ionization efficiency has been shown to be relatively independent of internal energy.[26,27,28] In detecting C_8H_8 and C_9H_{10} using 9.9 eV radiation we are ~1.5 eV above the ionization threshold and do not expect the photoionization efficiency to be significantly altered by the internal energy of the products.[17,23]

Both H-atom elimination and methyl elimination products are detected in the C_6H_5 + C_3H_6 reaction at E_{coll} = 108 kJ/mol. Time-of-flight arrival distribution for C_9H_{10} + H and C_8H_8 + CH_3 are shown in figures 5.6 and 5.7 respectively. Lab angular distributions for both product channels are shown in figure 5.8. The best fit center-of-mass functions are similar to the lower collision energy with forward-backward symmetric T(Θ)'s and P(E)'s that peak slightly away from zero translational energy release (Figure 5.9). The product branching ratio at E_{coll} = 108 kJ/mol is 3:1 for C_8H_8:C_9H_{10}. We measure a larger contribution for the C_8H_8 channel than was predicted by RRKM calculations and measured in a previous crossed molecular beam scattering experiment by Kaiser et al.[16] In the previous crossed molecular beam result, conducted at a lower collision energy (E_{coll} = 45 kJ/mol), one complication in detecting the C_8H_8 product channel was caused by background from fragmentation of C_9H_{10} products to the parent mass of $C_8H_8^+$.[16] We are able to eliminate the fragmentation problem by using "soft" photoionization at 9.9 eV, whereas in the Kaiser et al. study products were detected by the use of 80 eV electron impact

ionization. Since the ionization energies of C_8H_8 and C_9H_{10} are both near 8.5 eV,[17,23] the use of photon energy close to the to the ionization threshold of the detected species minimizes dissociative ionization, allowing products to be detected exclusively at their parent mass.

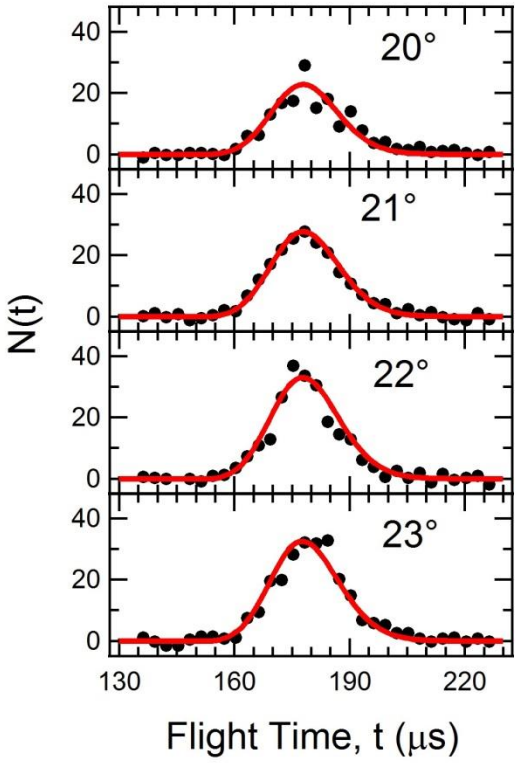

Figure 5.6: TOF spectra monitoring $C_9H_{10}^+$ (m/e =118) in the $C_6H_5 + C_3H_6 \rightarrow C_9H_{10} + H$ reaction, E_{coll} = 108 kJ/mol. Solid dots represent experimental data points; solid lines are calculated using the optimized CM distribution functions shown in Figure 5.9.

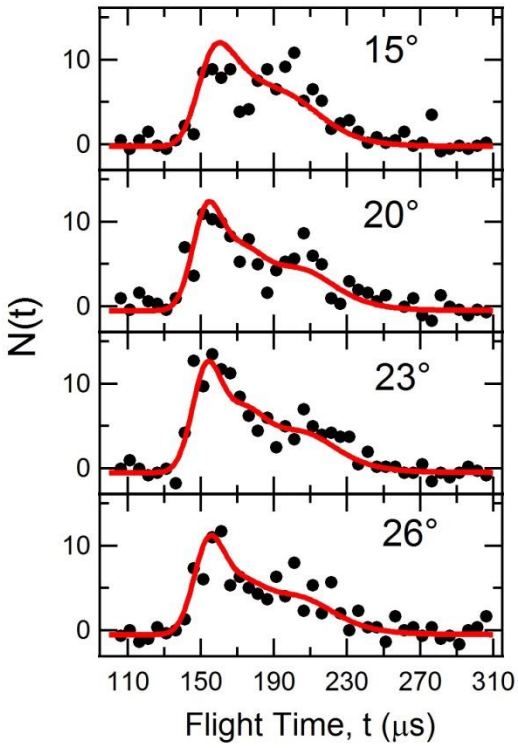

Figure 5.7: TOF spectra monitoring $C_8H_8^+$ (m/e =104) in the $C_6H_5 + C_3H_6 \rightarrow C_9H_{10} + H$ reaction, E_{coll} = 108 kJ/mol. Solid dots represent experimental data points; solid lines are calculated using the optimized CM distribution functions shown in Figure 5.9.

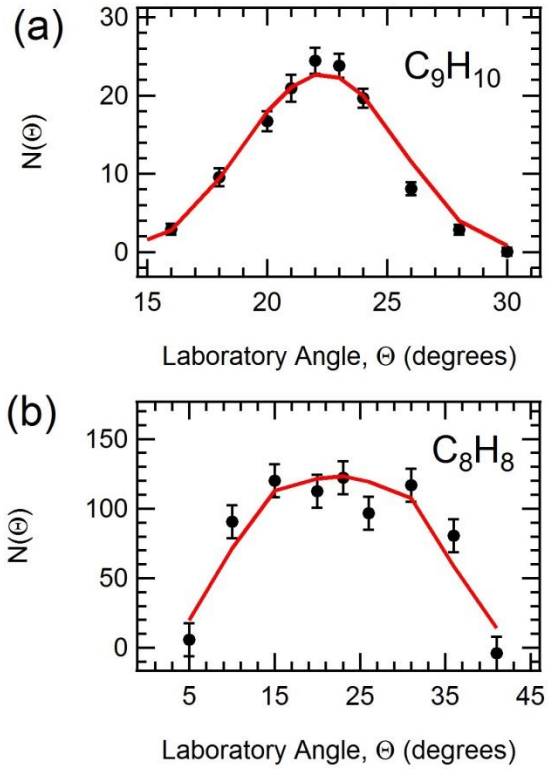

Figure 5.8: Laboratory angular distributions for the C_6H_5 + C_3H_6 reaction, E_{coll} = 108 kJ/mol. Solid dots represent experimental data points with 1σ error bars. Solid lines are calculated using the optimized CM distribution functions shown in Figure 5.9. (a) $C_9H_{10}^+$ (m/e = 118) from the C_6H_5 + C_3H_6 → C_9H_{10} + H reaction. (b) $C_8H_8^+$ (m/e = 104) from the C_6H_5 + C_3H_6 → C_8H_8 + CH_3 reaction.

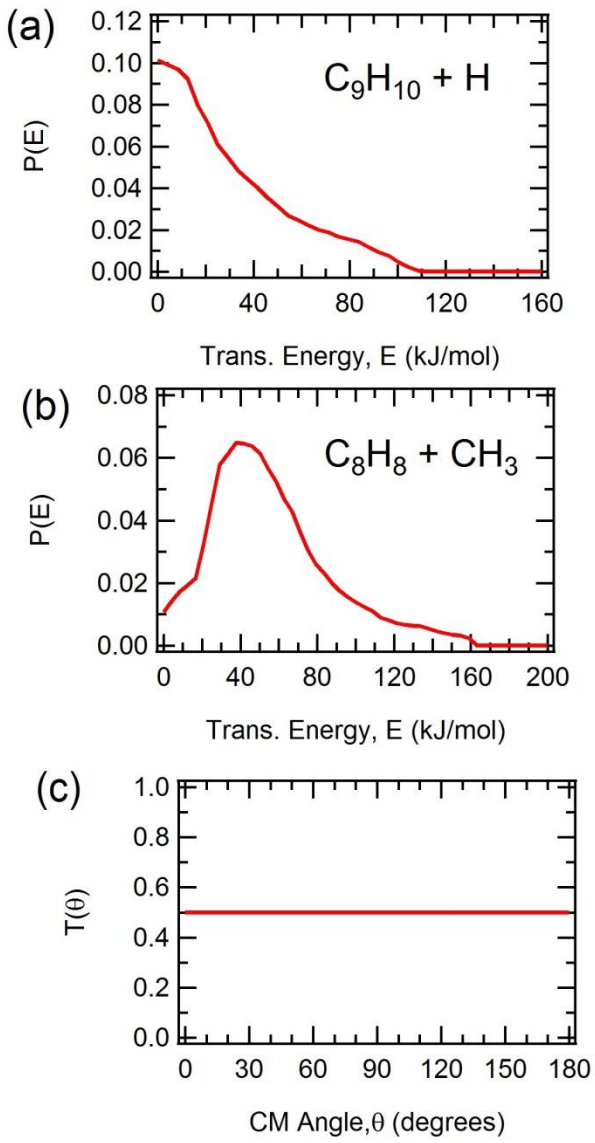

Figure 5.9: Optimized CM distributions for the C_6H_5 + C_3H_6 reaction, E_{coll} = 108 kJ/mol. (a) P(E) for the C_9H_{10} products; (b) P(E) for the C_8H_8 products; (c) T(Θ) used for both C_9H_{10} and C_8H_8 products.

In the C_6H_5 + C_3H_6 reaction, the phenyl radical can add to either the 1-or 2- carbon forming the 1-phenyl reaction intermediate (Figure 5.10a) and the 2-phenyl reaction intermediate (Figure 5.10b), respectively. On the basis of the calculated potential energy surfaces of Park et al[9] and Kaiser et al[16] the addition to the 1-carbon proceeds over a slightly smaller barrier than addition to the 2-carbon (~5 kJ/mol for addition to the 1-carbon and ~10 kJ/mol for 2-addition). In all of the crossed molecular beams experiments to date, the collision energies are very far above both of these addition barriers. Therefore, the relative importance of addition to the 1-carbon vs. 2-carbon will not depend strongly on barrier heights. However, a low energy isomerization pathway allows rapid conversion between the 1-carbon vs. 2-carbon intermediates.[9,16] This was confirmed in a recent RRKM study which found that the rate constant for isomerization is substantially faster than decomposition.[16] Under these conditions, the relative importance of addition to the 1-carbon or 2-carbon will not play an important role in determining the branching ratios between products.[16] This conclusion is supported by comparisons of RRKM branching ratios assuming exclusive addition to the 1-carbon or 2-carbon atoms, which found that the branching ratios are nearly identical in both cases. At very high collision energies (e.g., 200 kJ/mol) the product branching ratio for CH_3 elimination to H-atom elimination changes from 1:3.5 for exclusive addition to the 1-carbon to 1:2 for exclusive addition to the 2-carbon.[16] On the basis of these results, under our experimental conditions the initial phenyl radical addition site (1-carbon or 2-carbon) should have minimal influence on the product branching ratios.

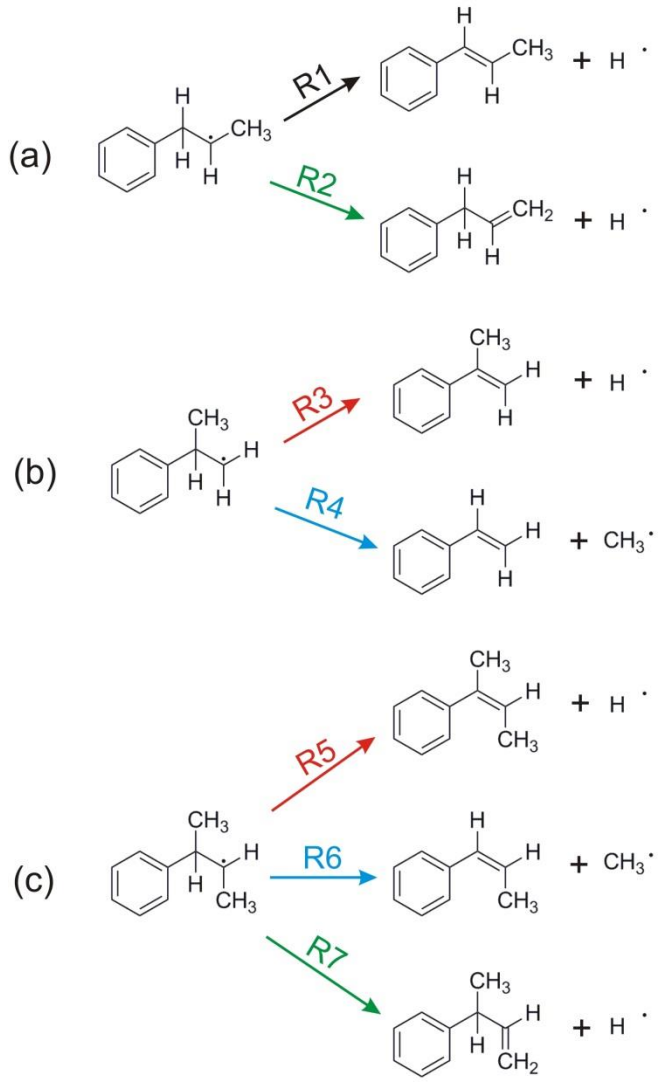

Figure 5.10: Schematic representation of reaction products from different addition intermediates. (a) 1-phenyl reaction intermediate in the $C_6H_5 + C_3H_6$ reaction. (b) 2-phenyl reaction intermediate in the $C_6H_5 + C_3H_6$. (c) Addition intermediate in the $C_6H_5 + C_4H_8$.

As shown in Figure 5.10a, the most likely products from the 1-phenyl reaction intermediate involves formation of C_9H_{10} isomers (1-phenyl propene (R1) or 3-phenyl propene (R2)) by H atom loss. From the 2-phenyl reaction intermediate, (Figure 5.10b) the likely decomposition product is $C_8H_8 + CH_3$ (R4), with H atom loss producing 2-phenyl propene (R3)

also possible. While we find the C_8H_8:C_9H_{10} branching ratio to be larger than in the previous crossed beams study and the accompanying RRKM calculations, we observed a decrease in this branching ratio with increasing collision energy, in agreement with the RRKM calculations.[16] The C_8H_8 to C_9H_{10} branching ratio decreased from 10:1 at E_{coll} = 84 kJ/mol to 3:1 at E_{coll} = 108 kJ/mol. The factor of three decrease with a ~24 kJ/mol increase in the collision energy, is larger than the RRKM predictions.[16]

C_6H_5 + C_4H_8 Experiments

In an effort to gain additional insight into the propene reaction, we have also studied the phenyl radical reaction with trans-2-butene (C_4H_8). In the reaction with C_4H_8, the 2- and 3-carbon atoms are chemically equivalent and addition at both sites produce a common reaction intermediate, as illustrated in Figure 5.10c. This intermediate (Figure 5.10c) resembles that of the 2-phenyl reaction intermediate in the C_6H_5 + C_3H_6 reaction, (Figure 5.10b), due to the presence of H atom and CH_3 at the carbon atom addition site.

The C_9H_{10} TOF arrival time distributions at E_{coll} = 97 kJ/mol for the reaction C_6H_5 + $C_4H_8 \rightarrow C_9H_{10} + CH_3$, are shown in Figure 5.11. The resulting laboratory angular and CM distributions are shown in figures 5.12 and 5.13, respectively. The P(E) peaks away from zero near 50 kJ/mol, implying that an exit barrier exists for the methyl elimination pathway. This is consistent with the behavior observed for the methyl-elimination channel in the C_6H_5 + C_3H_6 reaction. The T(Θ) is isotropic, suggesting the participation of collision complexes with lifetimes exceeding their rotational periods, as was observed in the propene reaction.

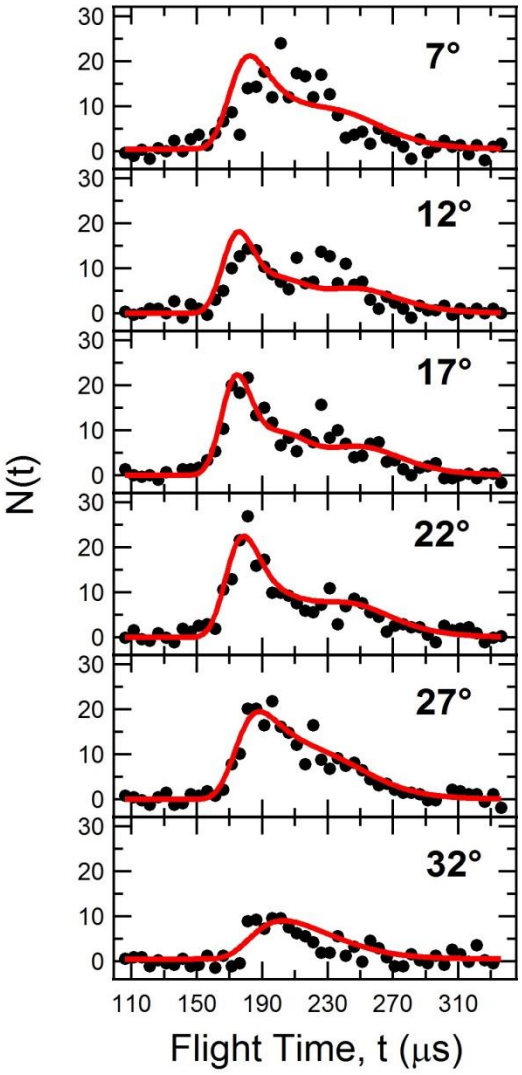

Figure 5.11: TOF spectra monitoring $C_9H_{10}^+$ (m/e =118) in the $C_6H_5 + C_4H_8 \rightarrow C_9H_{10} + CH_3$ reaction, E_{coll} = 97 kJ/mol. Solid dots represent experimental data points; solid lines are calculated using the optimized CM distribution functions shown in Figure 5.13.

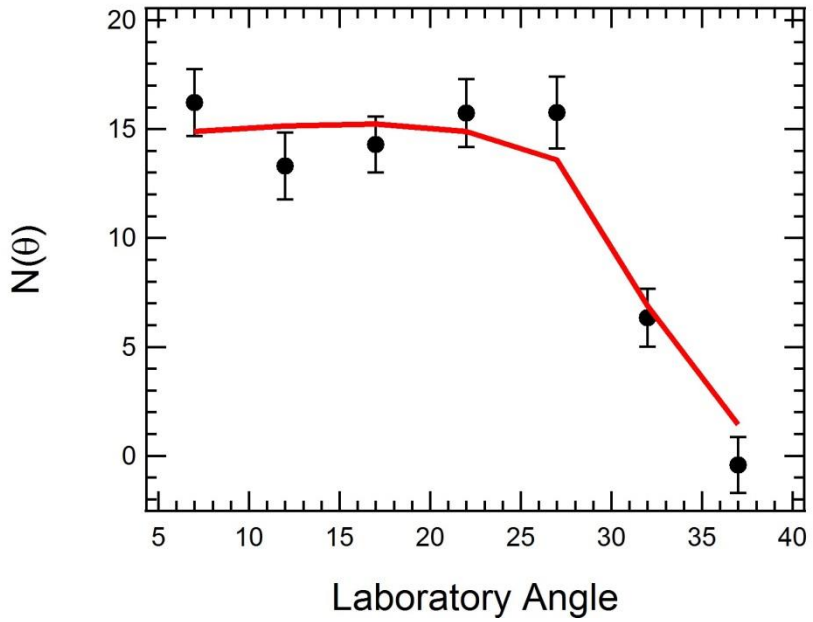

Figure 5.12: Laboratory angular distributions monitoring $C_9H_{10}^+$ from the $C_6H_5 + C_4H_8 \rightarrow C_9H_{10} + CH_3$ reaction, E_{coll} = 97 kJ/mol. Solid dots represent experimental data points with 1σ error bars. Solid lines are calculated using the optimized CM distribution functions shown in Figure 5.13.

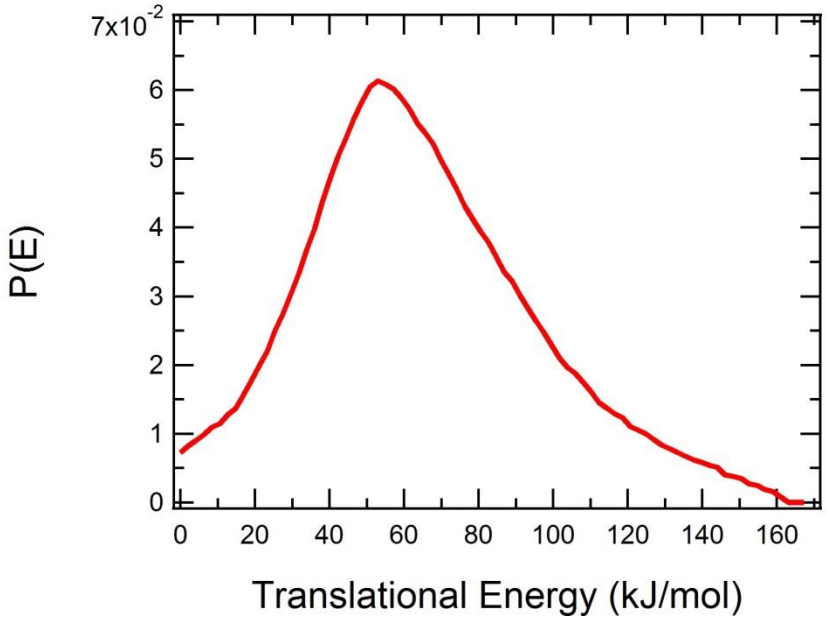

Figure 5.13: Optimized CM distributions, (a) P(E), (b) T(Θ) for the $C_6H_5 + C_4H_8 \rightarrow C_9H_{10} + CH_3$ reaction, E_{coll} = 108 kJ/mol.

We searched for the reaction $C_6H_5 + C_4H_8 \rightarrow C_{10}H_{12} + H$, but found no evidence for its existence. Due to the kinematics of the reactions, our detection sensitivity for the H-atom elimination channel should be more than an order of magnitude larger than for methyl elimination. The photoionization cross sections for phenyl products are similar, so no significant difference in detection sensitivity from differing photoionization cross sections should exist.[21,22] From these considerations, we conclude that the H atom elimination channel from $C_6H_5 + C_4H_8$ cannot account for more than 3% of the total reaction cross section.

Propene Reaction Mechanism

The absence of the H atom elimination channel in the 2-butene reaction is useful in understanding the propene reaction. The channels originating from the 2-phenyl reaction intermediates in the $C_6H_5 + C_3H_6$ reaction (Figure 5.10b) have analogues in the $C_6H_5 + C_4H_8$ reaction (Figure 5.10c): R3 is analogous to R5 because both involve H atom elimination from the carbon atom adjacent to the phenyl group. Similarly, R4 is analogous to R6 because both involve CH_3 elimination from the carbon atom adjacent to the phenyl group. The $C_6H_5 + C_4H_8$ reaction intermediate can also lose a hydrogen atom from the methyl group (R7 in Figure 5.10) in a manner analogous to the $C_6H_5 + C_3H_6$ reaction (R2 in Figure 5.10) forming 3-phenyl propene. Reaction R1 in the propene system, involving H atom elimination from a CH_2 moiety adjacent to the phenyl group, has no analogue in the butene system.

In the comparison of the butene and propene reactions, analogies must be used with some caution: the cis steric repulsions in the alkene products differ in the propene and butene systems, with the most unfavorable situations involving methyl-methyl and methyl-phenyl interactions more important for butene reactions. From these considerations, the H atom elimination

channels in the butene reactions are in general slightly less thermodynamically favorable than are the analogous products in the propene system.

As noted above, the absence of H atom products from the 2-butene reaction shows that reactions R5 and R7 cannot compete with R6. Because of the above-noted similarity between intermediates in Figure 5.10b and 5.10c, H-atom elimination from the 2-phenyl reaction intermediate (R3) is not likely to be competitive with CH_3 elimination (R4). Despite the slightly different (at most a few kcal/mol) energetics between the propene and butene reactions due to the cis-cis interactions, the butene results provide strong evidence that H atom elimination in the propene reaction primarily results from decomposition of the 1-addition intermediate illustrated in Figure 5.10a (R1 and R2).

Our finding that R7 is not competitive with R6 in the butene system is also of value in deriving insight into the propene reaction. The H-atom elimination pathway R7 for butene is analogous to R2 in the propene reaction, which is believed to be the sole source of 3-phenyl propene. In drawing conclusions from these analogies, it is important to remember that in the butene system, all products are formed from chemically indistinguishable reaction intermediates (Figure 5.10c) and are in direct competition with one another. In contrast, H atom elimination in the propene system via R2 is only in direct competition with R1 and any competition between R2 the other available channels (R3 and R4) requires isomerization between the 1- and 2- addition products. As noted above, the low barrier for isomerization and the RRKM calculations provide strong evidence that isomerization is much faster than product formation by bond fission under our experimental conditions.[16] Under such limiting conditions, all four decomposition pathways (R1-R4) can be considered to be in mutual competition, in a manner analogous to the competition (R5-R7) in the butene reaction. From the analogies between R7 and R2 and R5 and

R3 described above, one might be tempted to suggest that in the propene system, the H atom channels, R2 and R3, are not likely to be competitive with CH_3 elimination, R4. This would lead to the conclusion that in the propene system, the dominant source of H involves R1 and that the dominant C_9H_{10} isomers are cis-and trans- 1-phenylpropene. This conclusion is consistent with the earlier electronic structure calculations of Park et al.[9], as well as the earliest crossed beam studies using deuterated propenes which reported an 85:15 branching ratio for 1-phenylpropene: 3-phenylpropene.[15] However, this conclusion seems to be at odds with the more recent calculations[16,18], where the potential energy barrier for formation of 3-phenylpropene was calculated to be ~1 kJ/mol lower than that for cis-1-phenylpropene. The potential energy barrier for formation of trans-1-phenylpropene was not explicitly reported in that work, but apparently this channel was not deemed to be important.[16,18] The conclusion of the recent calculations that 3-phenylpropene (the highest energy isomer) is dominant is intriguing because it requires that decomposition of long-lived complexes proceeds by preferential fission of the strongest C-H bond in the reaction intermediate.[16,18]

In photoionization efficiency studies, it has sometimes been possible to identity the dominant isomers produced in a chemical reaction.[19,20] This method requires that the different isomers have significantly different ionization energies or exhibit distinctive structure in plots of photoionization cross section vs. photon energy.[19,20] For example, in the case of ethenol (IP = 9.3 eV) vs. acetaldehyde (IP = 10.2 eV), the much lower ionization energy of the enol isomer made it possible to unambiguously conclude that the enol form was produced in hydrocarbon oxidation.[19] Unfortunately, in the case of the C_9H_{10} isomers, the ionization energies are not significantly different; the ionization energies are 8.2, 8.3 and 8.4 eV for 1-, 2- and 3-phenylpropene, respectively.[17] While the ALS study reported that the observed photoionization

efficiency curves could be simulated by assuming 96% 3-phenylpropene, 3% 1-phenylpropene, *etc.*,[17] owing to the similarity in ionization energies in the present case, we have found that many other possibilities are also consistent with the experimental measurements, including dominant formation of 1-phenylpropene.

In previous crossed molecular beam studies, 3,3,3- trideuteropropene and 1,1,2-trideuteropropene were employed in an attempt to unambiguously determine the relative importance of channels R1-R3 in Figure 5.10.[15] In principle, by monitoring the relative yields of $C_9H_7D_3$ and $C_9H_8D_2$ production at m/e = 121 and 120, respectively, one can determine the branching ratio between atomic elimination from the 3- (i.e, the methyl group) vs. the 1- and 2-sites in the reaction intermediate. As already noted, the earlier study concluded that 1-phenylpropene was the dominant C_9H_{10} isomer.[15] However, fragmentation inherent in electron impact ionization makes such studies difficult. We believe that the use of "soft" photoionization detection should facilitate clearer identification of the dominant isomers, and we hope to carry out such studies in the near future. Therefore, while our conclusions appear to be in better agreement with the earlier work in which 1-phenyl propene was identified as the primary isomer[15], final conclusions about the isomeric form of the C_9H_{10} products remain tentative, and await upcoming definitive studies using deuterium-labeled propene reactants.

According to the previous calculations, phenyl radicals can abstract hydrogen atoms from propene forming C_6H_6 (benzene) + C_3H_5, with several different isomeric forms of C_3H_5 radical possible.[9,16,18] Abstraction of one of the three methyl H atoms forming resonantly-stabilized allyl radicals is most favorable energetically, with abstraction at the sp^2 hybridized carbon atoms leading to formation of 1- and 2- propenyl radicals.[9,18] In principle, these channels can be most easily monitored by detecting C_6H_6 at its parent mass, m/e = 78. Unfortunately, due to the

natural abundance of ^{13}C, background signals due to elastic and inelastic scattering of C_6H_5 is present, with intensities ~6% of that at m/e = 77. Unfortunately, this makes it impossible to detect nascent benzene from the abstraction channel. However, using deuterated propene, abstraction of a D atom produces C_6H_5D, which we can detect with high sensitivity at m/e = 79. Furthermore, by comparing the signals at this m/e = 79 from reactions of 3,3,3-trideuteropropene to that from 1,1,2- trideuteropropene, it will also be possible to assess the relative importance of abstraction at the methyl vs. sp^2 hybridized carbon atoms in propene. These studies are planned for the near future.

Conclusions

In the reaction of phenyl radicals with propene, both H-atom and CH_3 elimination products were observed at collision energies of 84 and 108 kJ/mol. At both collision energies, methyl radical elimination, forming C_8H_8 was found to be dominant, with branching ratios for C_8H_8:C_9H_{10} of 10:1 and 3:1 at 84 and 108 kJ/mol, respectively. The decrease in product branching ratio with increasing collision energy is consistent with recent RRKM predictions.[16] However we find the methyl radical elimination channel to be larger by roughly a factor of 5 as compared to the RRKM predictions. Further insight into the reaction mechanism was gained by studying the reaction of phenyl radicals with trans-2-butene, where addition leads to a single reaction intermediate analogous to the 2-phenyl reaction intermediate in the propene reaction. In the reaction with 2-butene, elimination of CH_3 forming C_9H_{10} was observed with the upper limit of 3% for the H-atom elimination products. From analogies between the open reaction channels in the propene and 2-butene reactions, we suggest that in the reaction with propene that the minor H-atom elimination channel results exclusively from decomposition of the 1-addition intermediate. While we tentatively suggest the reaction involves fission of the weakest C-H

bond, producing cis- or trans- 1-phenyl propene, definitive conclusions regarding the isomeric form of the C_9H_{10} product, and the mechanisms for the abstraction reactions forming benzene, awaits deuterium isotope labeling studies.

REFERENCES

1. H. Richter and J.B. Howard, *Progress in Energy and Combustion Science*, **26**, 565 (2000).

2. J.A. Miller, M.J. Pilling and J. Troe, *Proceedings of the Combustion Institute*, **30**, 43 (2005).

3. E.J. Highwood and R.P. Kinnersley, *Environment International*, **32**, 560 (2006).

4. M. Shiraiwa, K. Selzle and U. Pöschl, *Free Radical Research*, **46**, 927 (2012).

5. M. Frenklach, *Phys. Chem. Chem. Phys.* **4**, 2028 (2002).

6. B. Shukla and M. Koshi, *Combustion and Flame*, **158**, 369 (2011).

7. I.V. Tokmakov and M.C. Lin, *J. Am. Chem. Soc.* **125**, 11397 (2003).

8. I.V. Tokmakov and M.C. Lin, *J. Phys. Chem. A,* **108**, 9697 (2004).

9. J. Park, G.J. Nam, I.V. Tokmakov and M.C. Lin, M.C. *J. Phys. Chem. A*, **110**, 8729 (2006).

10. P. Casavecchia, F. Leonori, N. Balucani, R. Petrucci, G. Capozza and E. Segoloni, *Phys. Chem. Chem. Phys.*, **11**, 46 (2009).

11. N. Balucani, F. Leonori and P. Casavecchia, *Energy*, **43**, 47 (2012).

12. D.R. Albert and H.F. Davis," Experimental Studies of Bimolecular Reaction Dynamics Using Pulsed Tabletop Vacuum Ultraviolet Photoionization Detection" *Phys. Chem. Chem. Phys.* Submitted (2013)

13. H.J. Hefter, T.A. Hecht and G.S. Hammond, *J. Am. Chem. Soc.*, **94**, 2793 (1972).

14. X. Gu and R.I. Kaiser, R.I. *Acc. Chem. Res.* **42**, 290 (2009).

15. F. Zhang, X. Gu, Y. Guo and R.I. Kaiser, *J. Phys. Chem. A,* **112**, 3284 (2008).

16. R.I, Kaiser, D.S.N. Parker, M. Goswami, F. Zhang, V.V. Kislov, A.M. Mebel, J. Aguilera-Iparraguirre and W.H. Green, *Phys. Chem. Chem. Phys.* **14**, 720 (2012).

17. F. Zhang, R.I. Kaiser, A. Golan, M. Ahmed and N. Hansen,*J. Phys. Chem. A,* **116**, 3541 (2012).

18. V.V. Kislov, A.M. Mebel, J. Aguilera-Iparraguirre and W.H. Green, *J. Phys. Chem. A,***116**, 4176 (2012).

19. C.A. Taatjes, N. Hansen, A. McIlroy, J.A. Miller, J.P. Senosiain, S.J. Klippenstein, F. Qi, L. Sheng, Y. Zhang, T.A. Cool, J. Wang, P.R. Westmoreland, M.E. Law, T. Kasper and K. Kohse-Höinghaus, *Science*, **308**, 1887 (2005)

20. O. Welz, J.D. Savee, D.L. Osborn, S.S. Vasu, C.J. Percival, D.E. Shallcross, C.A. Taatjes,

Science, **335**, 204 (2012).

21. Z. Zhou, M. Xie, Z. Wang and F. Qi, F. *Rapid Commun. Mass Spectrom.* **23**, 3994 (2009).

22. T. Adam and R. Zimmermann, *Anal. Bioanal. Chem.* **389**, 1941 (2007).

23. P.J. Linstrom and W.G. Mallard, *NIST Chemistry WebBook*; NIST: Gaithersburg, MD, 2005.

24. J.C. Robinson, N.E. Sveum and D.M. Neumark, *J. Chem. Phys.,* **119**, 5311 (2003).

25. M.L. Morton, L.J. Butler, T.A. Stephenson and F. Qi, F. *J. Chem. Phys.*, **116**, 2763 (2002).

26. F. Aguirre, S.T. Pratt, *J. Chem. Phys.,* **122**, 234303 (2005).

27. H. Fan and S.T. Pratt, *J. Chem. Phys.,* **124**, 114312 (2006).

28. R.L. Gross, X. Liu and A.G. Suits, *Chem. Phys. Lett.*, **362**, 229 (2002).

CHAPTER 6: Conclusions and Future Directions

Phenyl radical reactions have been studied via the crossed molecular beam technique using high-intensity pulsed tabletop vacuum ultraviolet (VUV) single photon ionization at 9.9 eV. The "soft" nature of VUV single photon ionization has allowed for the study of reactions involving competing reaction pathways without interference from ion fragmentation. Crossed molecular beams experiments employing "soft" single photon ionization were previously limited either to products amenable to ionization at 7.9 eV from an excimer laser[1,2,3,4,5] or to experiments at dedicated synchrotron facilities.[6,7,8,9,10,11] The development of high-intensity VUV light sources using commercial tabletop lasers should increase the range of chemical systems that can be studied by researchers outside of synchrotron facilities. The pulsed nature of the VUV light source described here serves as a novel tool that facilitates the study of some chemical systems that are difficult to study using continuous detection schemes.

For product detection using synchrotron photoionization or electron impact ionization, the continuous nature of the detector is best exploited using *continuous* molecular beams.[12] By modulating the products using a slotted chopper wheel, product velocity distributions are measured by time of flight. Since elementary reactions between stable closed-shell molecules are rare,[13] *in-situ* production of free radicals is a fundamental requirement for such experiments, necessitating the use of *continuous* discharge[14,15] or pyrolysis[16] methods. As already noted, Casavecchia's group has pioneered both methods for studies of a wide range of important chemical systems using "soft" electron impact ionization, as summarized in comprehensive review articles.[14,17]

At Berkeley's Advanced Light Source, the first crossed beams apparatus employing synchrotron photoionization detection was available to the dynamics community between 1994

and 2004.[6] This apparatus was used extensively for studies of molecular photodissociation, most notably by the groups of Butler[18,19] and Neumark.[20,21,22] During this period, however, only three reactive scattering studies were published: $Cl + C_3H_8$ (propane) $\rightarrow C_3H_7 + HCl$[7], $Cl + C_5H_{12} \rightarrow C_5H_{11} + HCl$[8] and $^1CH_2 + C_2H_2 \rightarrow C_3H_3 + H$.[9] In the Cl atom studies, a continuous pyrolysis source was well-matched to the continuous nature of the detector.[7,8] Since a large fraction of Cl_2 can be dissociated at a moderate temperature, and because secondary reactions of the radicals within the nozzle are not significant, the product signal to noise ratios were quite high.

In the studies of reactions of electronically excited $^1CH_2$ at the ALS, photolysis of ketene using a 308 nm pulsed excimer laser (100 Hz) was employed.[9] For production of certain radical species, particularly molecular free radicals, photodissociation of a stable precursor is an extremely attractive approach. To achieve radical number densities sufficient for reactive scattering studies, photodissociation typically requires precursor molecules with sufficient cross-sections ($>5 \times 10^{-19}$ cm^2/molecule) for photodissociation producing the radical of interest. Lasers must be sufficiently powerful to photolyze a significant fraction of precursor molecules. This usually necessitates UV light from pulsed excimer (e.g., 193 nm or 248 nm) or Nd:YAG lasers (e.g., 355 or 266 nm). In such cases the pulse repetition rates are typically 10-200 Hz range.[23] Pulsed molecular beams offer advantages over continuous beams by facilitating the production of higher peak beam intensities with narrower velocity and internal energy distributions through the ability to use higher backing pressures.[23]

In many cases, the internal state distributions of photolytic free radical beams can be much colder than is possible using pyrolysis. For example, photodissociation of HNO_3 produces OH primarily in v = 0, and the OH rotational distribution is cooled upon supersonic expansion.[24] Since D_0 (HO-NO_2) is only 199 kJ/mol,[25] flash pyrolysis would seem to be an attractive approach

for producing intense beams of OH radicals.[16] However, since high nozzle temperatures are required, and since vibrational energy is in general not cooled efficiently upon supersonic expansion[26], substantial vibrational excitation is anticipated for such radical beams. For example, assuming a temperature of 1800 K, the fraction of OH in v = 1 (corresponding to 3700 cm^{-1} of internal energy) is calculated to be >5%. Our experimental measurements of an OH beam generated in this manner are consistent with these calculations. For reactive scattering studies where narrow distributions of reactant internal energies are highly desirable, such levels of vibrational excitation renders pyrolysis much less desirable than photolysis in the case of OH production.

The fundamental mismatch in duty cycle between *pulsed* photolytic beams and *continuous* detection methods such as electron impact ionization or synchrotron photoionization represents a significant experimental limitation. Using a 100 Hz photolytic source in an apparatus of this type, product TOF distributions typically arrives within a time window of 150 μs or less. Therefore, the duty cycle of the detector is typically no more than 1.5% (150 μs/pulse x 100 pulses/s = 0.015 s/s = 1.5%). Thus, although a third-generation synchrotron produces ~10^{16} photons/s, at most 1.5 x 10^{14} photons/s are actually usable when one or more components of the experiment are pulsed. Also, until the "top off mode" was introduced in 2003 at Berkeley's advanced light source, VUV intensities decayed over a several hour period, making normalization difficult.[27] The limitations on maximum pulse rates for high power UV lasers represented a significant inherent limitation to the use of the Berkeley apparatus in crossed beams experiments. While photodissociation experiments are also inherently pulsed (due to the need for a UV photolysis laser), the much larger signal levels inherent to photodissociation experiments (a factor of 10 or more) easily compensated for the duty cycle issue. The unique

ability provided by the synchrotron, to tune the photon energy just above threshold for photoionization made this apparatus extremely valuable in a range of studies.[20,27,28,29]

In 2002, a new crossed beam apparatus was commissioned at the Taiwan Synchrotron Light Source.[10] Although in many ways similar in design to the Berkeley machine, three notable improvements were made. First, the distance between the beam crossing region and photoionization region of the detector was reduced from 15 cm to 10 cm, leading to a factor of 2.25 increase in signal levels. Also, a quadrupole mass filter with larger pole diameter (1.25" instead of 0.75") was employed, increasing the ion transmission by a factor of ~2.[10] Finally, a new generation of pulsed valves with very short opening time has made it possible to significantly increase peak beam densities.[30] Collectively, these improvements have a major impact, opening up a wide range of studies not feasible using the Berkeley machine. Currently, this apparatus represents the state of the art in the field.

In our comparison of the use of pulsed photoionization to continuous electron impact ionization detection in transition metal-hydrocarbon chemistry, considerably higher signal to noise ratios were obtained using photoionization.[3] However, a significant experimental constraint in experiments using pulsed VUV photoionization with a fixed mass spectrometric detector is that only a single velocity and product scattering angle is probed at a given laser delay. To map out the product velocity distribution at a given laboratory angle, the delay of the photoionization laser relative to time zero for the reaction must be scanned. Typically such scans cover about 20-30 channels at 5 μs/channel. Due to VUV pulse intensity fluctuations, this produces statistical "noise" in the TOF distributions. While it is possible to normalize for long-term drifts in the VUV pulse energies, normalizing for shot to shot intensity fluctuations is difficult. Furthermore, obtaining product angular distributions requires that the angle of the two beams relative to the fixed

detector must be rotated. In typical cases, 6-15 different detector angles must be measured in a given experiment.

Ion imaging methods are widely-touted as being superior to "conventional" crossed beam experiments because they provide the opportunity to record the entire product angular and velocity distribution in each laser shot, corresponding to a large (factor of > 200) multiplexing advantage.[31] Therefore, one might anticipate that ion imaging using pulsed 9.9 eV photoionization could outperform the use of a conventional rotatable source-fixed detector apparatus. As already noted, Suits has studied a number of systems using this method utilizing a 7.9 eV excimer laser.[1,2] Honma and coworkers have recently employed imaging in reactions of transition metal atoms with oxidants such as O_2.[32] Such reactions have large cross sections and are amenable to ionization schemes employing near-UV lasers.[32] For such cases, the molecular species of interest can be ionized selectively with high efficiency and the probability for ionization of reactant molecules or other products is very small. On the other hand, for many studies, the use of *nonresonant* VUV ionization coupled with ion imaging detection is likely to be complicated by photodissociation of molecules in the interaction region[1] or from bimolecular reactions of ions produced by the VUV.[33] In several ion imaging studies by Suits and coworkers, products scattered into certain areas of the Newton circle could not be included in the analysis, leading to fundamental limitations in the range of angles that can be analyzed.[1] In Rydberg tagging experiments carried out in our laboratory, similar issues have frequently arisen. For example, in reactions involving hydrocarbon molecules, the H atom product is probed by Rydberg TOF spectroscopy. In this case, pulsed VUV at Lyman α at 121 nm is used to pump the $1s \rightarrow 2p$ transition, and then a second laser promotes the H atoms to $n \sim 40$. Since hydrocarbons absorb strongly at 121 nm producing H atoms, this represents an unwanted source of background signal that may be difficult to avoid.

Yang has proposed Rydberg tagging studies utilizing a rotatable source machine where the UV and VUV lasers are not located directly at the crossing region as a potential solution to this issue.[34] In this case, careful consideration of the density to flux transformation will be essential to ensure that product kinetic energy release distributions are accurate. We are currently exploring the use of near-transform limited UV lasers for generation of VUV for detection of H or O atoms in Rydberg tagging experiments. In this case, the use of very narrowband radiation may increase the contrast ratio between atomic excitation (with narrow lines) and photolysis (broad lines).

Our approach using "soft" single photon pulsed ionization allows the product molecules to drift to a triply differentially pumped detector (10^{-10} Torr) before ionization, spreading out according to their velocities. In contrast to ion imaging or Rydberg tagging experiments where VUV is introduced into the high-pressure molecular beam crossing region, no interference from photodissociation or ion-molecule reactions is observed. As illustrated above, the very high ionization efficiency and very low background count rates lead to quite high signal to noise ratios in our experiment. However, the need to scan the laser delay to measure product TOF distributions represents the key remaining limitation in our current implementation of soft photoionization in crossed beams reactions. To overcome this, we are currently developing the use of *coaxial* VUV photoionization detection. As illustrated in Figure 6.1, the use of a fixed detector geometry makes it relatively straightforward to introduce the ionization laser along the detector axis in a counterpropagating geometry. The neutral products from bimolecular reactions drift from the interaction region with their nascent velocity distributions, with a small fraction passing through a series of apertures. Rather than ionizing a 2-3 mm length of the neutral distribution using the crossed-beam configuration employed to date, the packet of neutral

molecules is allowed to spread out according to their neutral velocities. At a suitable VUV laser delay, the entire column of neutrals is photoionized by the VUV pulse within a 33 cm long ion guide. Since a light electron is ejected, photoionization does not lead to an appreciable velocity perturbation, and the positive ion is then mass filtered and detected as usual. Photodissociation, if it occurs, leads to ejection of photofragments from the detector axis and will not produce significant background signals. The great advantage of this approach is that the *entire* packet of neutrals is ionized in each laser pulse, rather than a 2-3 mm long segment. The anticipated increase in signal to noise ratio is very large, and will depend upon the specific kinematics of the system under study. The calculated lower limit to the improvement is based on the fact that it will no longer be necessary to scan the VUV laser delay over ~30 channels. The upper limit corresponds to the fact that ionization will occur over a 33 cm pathlength, rather than in a 3 mm pathlength as in the orthogonal (crossed beam) configuration. We thus anticipate increases in signal to noise ratios of a factor of 30-100.

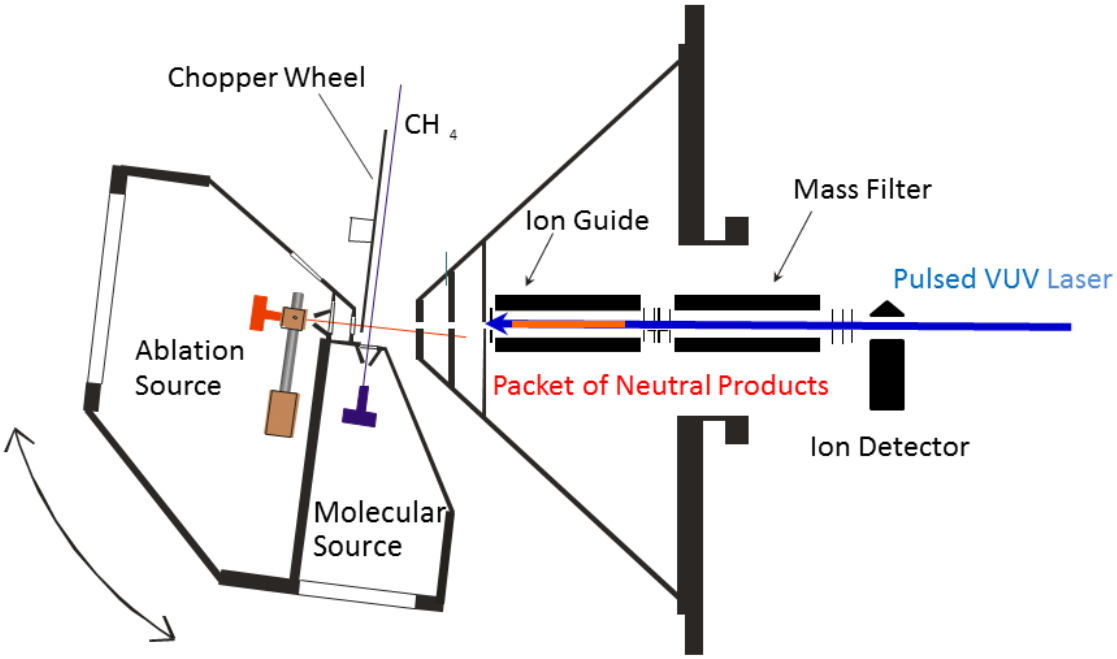

Figure 6.1: Crossed Beams Apparatus with Coaxial Photoionization Detection. Neutral products drift from crossing region through several apertures into ion guide region where they are photoionized by a counterpropagating VUV laser beam. Ions are then mass filtered and detected. The entire velocity distribution is recorded for each laser shot.

The primary challenge in implementing the coaxial ionization method is of a technical nature. One needs to ensure that the entire packet of neutrals is detected with constant (or at least known) sensitivity. We are presently characterizing this approach using a fixed beam apparatus and hope to be able to introduce this method to crossed beam studies in the near future. The most notable improvement will result from the much larger signal levels and the elimination for the need to scan the delay of the detection laser. Since the number of photons is much greater

than the number of absorbing molecules, the VUV intensity is constant along the beam axis so no correction for absorption is required.

Our present approach for VUV generation using unfocussed laser beams is most efficient at wavelengths near 125 nm, corresponding to photon energies of ~9.9 eV. While this method can be extended to somewhat higher photon energies, a fundamental constraint is that the transmission of light through MgF_2 and LiF optics decreases sharply at shorter wavelengths, falling to zero at $\lambda < 104$ nm for LiF. To overcome this limitation, we are currently developing techniques to extend the wavelength range into the XUV ($\lambda < 110$ nm) by using resonance enhanced four-wave mixing of focused laser beams in Hg vapor produced by laser vaporization at room temperature.[35] In this way, a windowless configuration can be employed. Furthermore, by using noncollinear phasematching[36], the need for dispersive elements to separate the XUV from the residual UV beams is eliminated. By combining this approach with the use of coaxial photoionization, we expect that we will be able to use pulsed photoionization for detecting many chemically interesting species with ionization energies up to 12 eV.

REFERENCES

1. C. Huang, W. Li, A.D. Estillore and A.G. Suits, *J. Chem. Phys.*, **129,** 074301 (2008).

2. A.D. Estillore, L.M. Visger-Kiefer and A.G. Suits, *Faraday Discuss.*, **157**, 181 (2012).

3. P.A. Willis, H.U. Stauffer, R.Z. Hinrichs and H.F. Davis, *Rev. Sci. Instrum.,* **70**, 2606 (1999).

4. J.J. Schroden and H.F. Davis, *J. Phys. Chem. A,* **116**, 3508 (2012).

5. M. Oana, Y. Nakatsuka, D.R. Albert and H.F. Davis, *J. Phys. Chem. A,* **116**, 5039 (2012).

6. X. Yang, J. Lin, Y.T. Lee, D.A. Blank, A.G. Suits and A. Wodtke, *Rev. Sci. Instrum.*, **68**, 3317 (1997).

7. D.A. Blank, N. Hemmi, A.G. Suits and Y.T. Lee, *Chem. Phys.*, **231**, 261 (1998).

8. N. Hemmi and A.G. Suits, *J. Chem. Phys.*, **109**, 5338 (1998).

9. H.F. Davis, J. Shu, D.S. Peterka and M. Ahmed, *J. Chem. Phys.*, **121**, 6254 (2004).

10. C.C. Wang, Y.T. Lee, J.J. Lin, J. Shu, Y-Y. Lee and X. Yang, *J. Chem. Phys.*, **117**, 153 (2002).

11. C-H. Chin, W-K. Chen, W-J. Huang, Y-C. Lin and S-H. Lee, *J. Phys. Chem A*, **116**, 7615 (2012).

12. W.R. Gentry in *Atomic and Molecular Beam Methods*, edited by G. Scoles (Oxford University Press, New York, 1988), Vol. 1, pp. 54-82.

13. J.J. Lin, *Phys. Chem. Chem. Phys.*, **13**, 19206 (2011).

14. P. Casavecchia, F. Leonori, N. Balucani, R. Petrucci, G. Capozza and E. Segoloni, *Phys. Chem. Chem. Phys.*, **11**, 46 (2009).

15. P.C. Engelking, *Rev. Sci. Instrum.*, **57**, 2275 (1986).

16. D.W. Kohn, H. Clauberg and P. Chen, *Rev. Sci. Instrum.,* **63**, 4003 (1992).

17. N. Balucani, G. Capozza, F. Leonori, E. Segoloni and P. Casavecchia, *Ann. Rev. Phys. Chem.,* **25**, 109 (2006).

18. J.A. Mueller, B.F. Parsons, L.J. Butler, F. Qi, O. Sorkhabi and A.G. Suits, *J. Chem. Phys.*, **114**, 4505 (2001).

19. M.L. Morton, L.J. Butler, T.A. Stephenson and F. Qi, *J. Chem. Phys.,* **116**, 2763 (2002).

20. W. Sun, K. Yokoyama, J.C. Robinson, A.G. Suits and D.M. Neumark, *J. Chem. Phys.*, **110**, 4363 (1999).

21. N.E. Sveum, S.J. Goncher and D.M. Neumark, *Phys. Chem. Chem. Phys.,* **8**, 592 (2006).

22. J.C. Robinson, N.E. Sveum and D.M. Neumark, *J. Chem. Phys.,* **119**, 5311 (2003).

23. W.R. Gentry in *Atomic and Molecular Beam Methods,* edited by G. Scoles (Oxford University Press, New York, 1988), Vol. 1, pp. 54-82.

24. B.R. Strazisar, C. Lin and H.F. Davis, *Science,* **290**, 958 (2000).

25. J. Chase, W. Malcolm (Eds.), NIST-JANAF Thermochemical Tables, American Chemical Society, Washington, DC,1998.

26. S. Stolte in *Atomic and Molecular Beam Methods,* edited by G. Scoles (Oxford University Press, New York, 1988), Vol. 1, pp. 631-652.

27. S.R. Leone, M. Ahmed and K.R. Wilson, *Phys. Chem. Chem. Phys.,* **12**, 6564 (2010).

28. O. Welz, J.D. Savee, D.L. Osborn, S.S. Vasu, C.J. Percival, D.E. Shallcross and C.A. Taatjes, *Science,* **335**, 204 (2012).

29. C.A. Taatjes, N. Hansen, D.L. Osborn, K. Kohse-Höinghaus, T.A. Cool and P.R. Westmoreland, *Phys. Chem. Chem. Phys.*, **10**, 20 (2008).

30. U. Even, J. Jortner, D. Noy, N. Lavie and C. Cossart-Magos, *J. Chem. Phys.*, **112**, 8068 (2000).

31. S.J. Greaves, R.A. Rose and A.J. Orr-Ewing, *Phys. Chem. Chem. Phys.*, **12**, 9129 (2010).

32. K. Honma and Y. Matsumoto, *Phys. Chem. Chem. Phys.*, **13**, 8236 (2011).

33. J.C. Weisshaar, *Acc. Chem. Res.*, **26**, 213 (1993).

34. X. Yang, *Phys. Chem. Chem. Phys.*, **13**, 8112 (2011).

35. M.A. Todt, D.R. Albert and H.F. Davis, "High Intensity VUV and XUV Generation by Noncollinear Phasematching in Laser Vaporized Media" *To Be Submitted.*

36. S. Hannemann, U. Hollenstein, E.-J. van Duijn and W. Ubachs, *Opt. Lett.*, **30**, 1494 (2005).